DYNAMIC CONTRAST-ENHANCED MRI IN RAT GLIOBLASTOMA MODELS: VASCULAR PARAMETERS AND CORRECTIONS FOR SYSTEMATIC ERRORS

by

PRABHU CHANDRA ACHARYA

A dissertation submitted in partial fulfillment of the
requirements for the degree of

DOCTOR OF PHILOSOPHY IN BIOMEDICAL SCIENCES:

MEDICAL PHYSICS

2025

Oakland University
Rochester, Michigan

Doctoral Advisory Committee:

Yang Xia, Ph.D., Chair
James R Ewing, Ph.D., Co-Chair
Stephen L Brown, Ph.D.
Tavarekere N Nagaraja, Ph.D.
Hassan Bagher-Ebadian, Ph.D.

This work is dedicated to my late mother Mina Kumari Acharya and late grandmother Kamala Devi Acharya

ACKNOWLEDGEMENTS

First and foremost, I would like to express my sincere gratitude to my advisor, Dr. James R Ewing, Department of Neurology, Henry Ford Health (HFH), for allowing me to pursue my research work under his supervision and providing me a great opportunity to be a part of his team. I am deeply indebted to his scholarly guidance, valuable time for teaching, encouragement, and endless help and support from the day I joined his laboratory to the completion of this work. I would like to extend my sincere gratitude to Dr. Yang Xia, for his invaluable help and support with academic matters at Oakland University (OU). My genuine thanks and appreciation to Dr. Stephen L Brown for his great mentorship, wise counseling, and serving as a source of profound wisdom. My sincere thanks to Dr. Bradley J Roth for providing me an opportunity to enroll as a medical physics graduate student at OU and his invaluable support during the initial semesters of my study. My sincere thanks and appreciation to Dr. Tavarekere N Nagaraja, and Dr. Hassan Bagher-Ebadian for their mentorship, encouragement, and help in publications. I would like to extend my gratitude to the faculty and staff members of the Physics Department, OU and the Neurology Department, HFH for their guidance and assistance throughout the years. Thanks to all dissertation committee members for their invaluable time and participation for evaluating this research work. I am also thankful for the grant support from the National Institute of Health.

Finally, my family, wife Binita, and lovely sons Aaradhya and Ashvik have been a great source of motivation for me ever.

ABSTRACT

DYNAMIC CONTRAST-ENHANCED MRI IN RAT GLIOBLASTOMA MODELS: VASCULAR PARAMETERS AND CORRECTIONS FOR SYSTEMATIC ERRORS

by

PRABHU CHANDRA ACHARYA

Advisors: Yang Xia, Ph.D., James R Ewing, Ph.D.

Dynamic contrast-enhanced MRI (DCE-MRI) is widely used in pharmacokinetic modeling to assess biomarkers of treatment response and predictors of tumor progression. Plasma volume fraction (v_p), blood-to-tissue forward volumetric transfer constant (K^{trans}), and interstitial volume fraction (v_e) are the most common biomarkers that explain tumor physiology in embedded cerebral gliomas. DCE-MRI demand stability of receiver sensitivity across the time of study but may suffer from high duty-cycle imaging instability that can bias parameter estimates. In this dissertation, an analysis of DCE-MRI data affected by unstable receiver sensitivity acquired at 7T in a rat model of 9L glioblastoma (GBM) is presented. Phantom studies verified that an unexpected variation in K^{trans} in 9L rat model of gliosarcoma was the result of reduction in receiver signal amplitude, indicating a baseline signal drift. Cooling the coil and repeating the experiment pointed to heating of the coil as the root of the problem, a finding confirmed by the vendor. A correction to the amplitude drift based on a heuristic logarithmic function is presented.

Two patient-derived orthotopic xenograft (PDOX) models of GBM (HF3016 and HF3177) were characterized using multiparametric MRI. Vascular and tumor microenvironmental (TME) parameters (v_p, K^{trans}, v_e, VD, tumor exudate flux) were estimated with DCE-MRI along with multiparametric MRI. DCE data were analyzed voxel-wise using Patlak, extended Patlak, and Logan methods, with a data-driven model selection approach for defining the tumor and the normal tissue regions. While vascular and diffusion parameters showed no significant differences between the two models ($p>0.05$), Flux strongly correlated with V_D at the tumor rim. These data report physiological properties of untreated GBM that are representative of human disease both geno- and pheno-typically.

Tumor interstitial fluid pressure (TIFP) was measured using the invasive technique in treatment naïve and in irradiated 9L gliosarcoma cerebral tumors in rats. The signatures of acute treatment response were investigated using DCE-MRI. Parameters K^{trans}, v_e ,V_D and Flux, were assessed in these cohorts in paired experiments 24 hours apart, with intervening radiotherapy (RT) in the treatment animals. TIFP and tumor blood flow were significantly reduced ($p<0.05$) post RT. DCE-MRI biomarkers showed a decrease post RT; notably Flux and V_D significantly decreased post RT ($p<0.05$) and were strongly correlated indicating a clear signature of radiation response. The regression fits of Flux versus V_D also differed ($p<0.05$) between the two cohorts.

TABLE OF CONTENTS

TABLE OF CONTENTS—Continued

TABLE OF CONTENTS—Continued

TABLE OF CONTENTS—Continued

LIST OF FIGURES

LIST OF TABLES

LIST OF ABBREVIATIONS

aCSF	Artificial cerebrospinal fluid
IACUC	Institutional Animal Care and Use Committee
ADC	Apparent diffusion coefficient
DCE	Dynamic contrast enhanced
CNS	Central nervous system
$C_p(t)$	Contrast agent concentration in blood plasma at time t
$C_t(t)$	Contrast agent concentration in tissue at time t
PS	Permeability-surface area
H & E	Hematoxylin and eosin
MHC	Major immunohistopathology complex
ROI	Region of interest
RT	Radiotherapy
TBF	Tumor blood flow
TMZ	Temozolomide
AIF	Arterial input function
ASL	Arterial spin labelling
CA	contrast agent
EES	Extracellular extravascular space
HFH	Henry Ford Health
RF	Radiofrequency
TR	Time of repetition

TE	Time of echo
TME	Tumor microenvironment
FA	Flip angle
SM	Standard model
GBM	Glioblastoma
GS	Gliosarcoma
GD-DTPA	Gadolinium-diethylene-triaminepentaacetic acid
LL	Look-Locker
SF	Scale factor
BBB	Blood-brain barrier
MTT	Mean transit time
VEGF	Vascular endothelial growth factor
PDX	Patient derived xenograft
PDOX	Patient derived orthotopic xenograft
PET	Positron emission tomography
SPECT	Single photon emission computed tomography
PK	Pharmacokinetic
DCE-MRI	Dynamic contrast-enhanced magnetic resonance imaging

MVP	Microvascular pressure
IFP	Interstitial fluid pressure
TIFP	Tumor interstitial fluid pressure
WIN	Wick-in-needle
Flux	Tumor exudate flux at tumor rim/peritumoral flux
SNR	Signal-to-noise ratio
CNR	Contrast-to-noise ratio
DWI	Diffusion weighted imaging
MR	Magnetic resonance
SPGRE	Spoiled gradient-recalled echo
DAB	Diaminobenzidine
CBCT	Cone beam computed tomography
PDF	Probability density function
MNU	N-methyl-N-Nitrosourea
FET	Field effect transistor
PIN	P-type – Intrinsic -N-type
Q	Quality factor
SARRP	Small animal radiation research platform
AD	Active decoupling
SRS	Stereotactic radiosurgery
K-S	Kolmogorov-Smirnov

CHAPTER ONE

INTRODUCTION

This dissertation deals with measures of tumor physiology and vascular characterization of human glioblastoma in orthotopic rat models using dynamic contrast-enhanced (DCE) MRI[2-5]. The study presents DCE-MRI as an important measure of physiology in brain tumor studies and describes systematic errors that impact the subsequent pharmacokinetic (PK) analysis, potentially affecting DCE-MRI derived vascular parameter estimates[6,7]. The three chapters following this Introduction review glioma physiology, DCE-MRI's role in tracer PK analysis in embedded brain tumor models, and error propagation in DCE-MRI. Chapters 5 though 7 present three original studies in animal tumor models and phantoms, with results and inferences drawn from each experiment. The final chapter (Chapter 8) is the summary of all findings of this dissertation and a discussion of future work.

1.1 Introduction and motivation

MRI is a widely used noninvasive imaging modality with critical applications in clinical diagnostics and biomedical research[8,9]. It provides visualization of the structural and functional characteristics of soft tissues, making it particularly valuable in the detection and characterization of such pathologies as solid tumors[10]. Compared to other imaging modalities, MRI offers superior contrast-to-noise ratio (CNR) in soft tissue**,** rapid acquisition capabilities, and sensitivity to a wide range of endogenous and exogenous contrast mechanisms[3]. MRI is especially powerful in neurological research

due to its ability to differentiate white and gray matter and to visualize pathological changes in the central nervous system via paramagnetic contrast agents[11,12].

DCE-MRI has emerged as a frequently applied method for noninvasively evaluating tumor vasculature in both preclinical and clinical oncology[3,13,14]. DCE-MRI utilizes serial acquisition of T_1-weighted images before, during, and after intravenous administration of a low molecular weight paramagnetic contrast agent**,** typically gadolinium-based, to monitor the dynamic passage of contrast through tissue[4,15]. Contrast is mapped to contrast agent (CA) concentration and pharmacokinetic modeling such as the Tofts[16] or Patlak[17,18] model is applied to the resulting concentration-time curves to estimate key physiological parameters of tumor microvasculature. These include plasma volume fraction (v_p), blood-to-tissue forward volumetric transfer constant (K^{trans}), interstitial volume fraction (v_e) or the extravascular-extracellular space (EES), tumor exudate flux etc.

As with other imaging modalities, MRI is vulnerable to errors in data acquisition, both random-like that reduce precision, and systematic that introduce bias and jeopardize the accuracy of the image produced. In addition to physical motion and partial volume effects, the most common sources of systematic error, MRI is also vulnerable to artifacts arising from hardware-related issues, especially when high duty-cycle imaging procedures such as DCE or DWI are required by the imaging protocol[19-21]. Signal amplitude drift during DCE-MRI imaging resulting from the heating of active components of a phased-array receiver coil (e.g., FET, PIN diode, resistor etc.) was measured while using gradient echo sequences with high temporal resolution, short TR and TE, and a long total scan duration. The drift was visible in the baseline signal prior to

administration of contrast injection. The drift was observable in a phantom experiment, which showed that behavior was not the function of signal from the phantom; removing the phantom and repeating the experiment resulted in persistent signal amplitude drift in the noise. Moreover, cooling the surface coil with an ice-filled bag across its upper surface showed no radiofrequency (RF) drift, confirming that thermal effects in the receiver coil were the root of the problem. A correction strategy was explored to correct the observed baseline drift (discussed in chapter 6).

Human gliomas originate from glial cells, cells that normally support the function of neurons in the central nervous system (CNS). Gliomas exhibit a variety of phenotypes, from slow-growing low-grade gliomas to highly malignant glioblastomas (GBM). GBMs are the most common and lethal form of all gliomas[22-24]. Generally, tumor morphology and the associated microenvironment present structural and functional anomalies in contrast to the normal tissues. Such abnormalities are manifestations of their aggressive behavior and often reflect a microenvironment with high vascular permeability, hypoxia, poor lymphatic drainage, and highly elevated interstitial fluid pressure(IFP)[25,26]. GBMs usually manifest rapid tumor proliferation, diffuse infiltration to surrounding brain, and resistance to conventional therapies[27,28]. Despite decades of intensive research, prognosis remains dismal, with median survival rarely exceeding 15 months following standard-of-care therapy comprised of maximal surgical resection, radiation therapy, and temozolomide (TMZ) chemotherapy[22,27,29,30].

A major hurdle in evaluating treatments of gliomas is the lack of a pre-clinical brain tumor model that accurately reproduces the salient features of human GBM pathology[23,31-33]. More than 80% of promising pre-clinical agents fail in oncological

clinical trials; until recently, available models have not replicated the complexity of human GBM pathology[33]. Pre-clinical cell-line xenograft tumor models (e.g. U251N) derived from immortalized cells, are in common use but differ pheno- and geno-typically from human GBMs[23,34] . In contrast, patient derived orthotopic xenograft (PDOX) models, freshly resected from human GBM and cultured in a serum-free environment, are promising in preserving genetic and molecular properties[23,35-37]. These models are better suited for early-stage drug studies[23,33,38]. A knowledge of tumor vascular and microenvironmental parameters is a useful first step in designing and deploying efficient therapeutic strategies. In this dissertation, a quantitative assessment of PDOX GBM tumor microvascular parameters using a DCE-MRI technique, (discussed later in this chapter with details in chapter 2 & 3) is presented. The microvascular parameter estimates reported establish baseline values of tissue parameters in treatment-naïve PDOX tumors.

GBM tumors are known for increased interstitial fluid pressure (IFP), a hallmark of these malignant gliomas, a precursor of tumor aggressiveness, and a catastrophe to therapy[26,39-41]. In normal tissue, the blood-brain-barrier (BBB) is intact and the hydrostatic and the oncotic pressure gradient is maintained. In tumors, vasculature is abnormal, characterized by dilated, tortuous vessels, vascular shunting and poor drainage. Loss of the BBB leads to a loss of microvascular-to-interstitial oncotic gradient and an equilibration between perfusion pressure and tumor interstitial fluid pressure[39,41-46]. This loss of transcapillary pressure gradient thus limits the convective transport to the tumor[26,45,47,48]. When IFP approaches microvascular pressure (MVP), perfusion ceases, resulting in a local ischemia[45,49]. Mechanical stresses in the tumor border may also

generate a vascular collapse and reduction in perfusion pressure. Jain et al[45,46,48,50] and colleagues propose that local mechanical stresses related to tumor growth, among other factors, can compress fragile tumor vessels, causing vascular collapse that lowers perfusion pressure and thereby reduces blood flow, oxygen delivery, and drug transport.

Elevated tumor interstitial fluid pressure (TIFP) is a major impediment to the penetration of therapeutic agents[26,40,47]. Studies in pre-clinical tumor models have shown TIFP decreases after an acute dose of radiation[51,52]. Thus, selecting an appropriate time window with a low TIFP for drug delivery might improve drug distribution in the tumor and increase therapeutic efficacy[46]. A non-invasive estimate of TIFP using DCE-MRI has been proposed[41,53], but its correlation with such tumor microenvironmental parameters as tumor exudate flux, peritumoral distribution volume (V_D) etc., in treated embedded tumors with their potentiality as treatment response biomarkers has to the best of my knowledge not been sought. In this study, the interstitial fluid pressure was measured in an untreated and radiotherapy-treated cerebral glioma tumors using a wick-in-needle (WIN) technique and examined the therapeutic response in association with DCE-MRI derived microvascular parameters, including V_D and associated tumor exudate flux (Flux) estimates[1,41]. Further, a correlation between TIFP and V_D and/or Flux was investigated to evaluate if V_D and/or Flux alone could serve as surrogate measures of TIFP in treatment naïve gliomas. To the best of my knowledge this new concept has not previously been explored.

1.2 Dissertation specific aims

This dissertation has three specific aims. As the first aim, it uses DCE-MRI and established kinetic modeling (Patlak, Logan) to quantitatively characterize PDOX rat

models of both primary and recurrent GBM using cancer stem-like cell-enriched neurosphere preparation from the same patient—a novel approach that yields benchmark microvascular parameters for evaluating candidate therapies.

The second aim investigates TIFP as a biomarker of therapeutic response, correlating direct TIFP measurements in treatment-naïve and irradiated tumors with such DCE-MRI-derived parameters as V_D and Flux. These relationships[1,54] offer insight into interstitial fluid flow, mechanical stress, and edema, with implications for GBM recurrence.

The third aim addresses a technical barrier to accurate DCE-MRI analysis: systematic baseline signal drift in pre-contrast data. Identifying the source, implementing correction strategies, and reanalyzing affected datasets will improve pharmacokinetic modeling accuracy and serve as a methodological reference for future studies at Henry Ford Health (HFH) and beyond.

1.3 Dissertation organization

This dissertation contains eight chapters. They are organized as follows: This First chapter is the Introduction and motivation about this dissertation work with highlights on GBM tumor physiology, application of DCE-MRI in preclinical glioma model, and a unique example of systematic bias encountered in MRI influencing PK modelling in embedded gliomas.

Chapter Two describes pharmacokinetic modelling of DCE data with a classic approach of model selection for segmenting the tumor and normal tissue by utilizing Patlak[17,18] and Logan[55,56] graphical methods for estimating tumor physiological parameters.

Chapter Three discusses the role of DCE-MRI estimated microvascular and tumor microenvironment (TME) parameters in evaluating tumor physiology and their utility as and post-treatment biomarkers to glioma pathology.

Chapter Four describes error sources during MRI data acquisition procedure and their subsequent impact in imaging system and the MR data through error propagation.

Chapters Five, Six, and Seven present the original experimental work of this dissertation. Chapter Five is the quantitative characterization of major physiological parameters of PDOX GBM tumor model using DCE-MRI. Chapter Six is focused on an assessment of baseline signal intensity drift observed during DCE-MRI data acquisition in a 7T magnet and its impact on modeling, which also includes a correction method to cope with that. Chapter Seven presents TIFP measurements in 9L gliomas (treatment-naïve and irradiated) using the WIN method, along with DCE-MRI, to assess therapy response and examine a potential connection between TIFP, peritumoral distribution volume, and Flux.

Finally, chapter Eight provides the overall summary and conclusion of this dissertation, with study limitations and future perspectives.

CHAPTER TWO

PHARMACOKINETICS FOR DCE-MRI IN CEREBRAL TUMORS

This chapter describes the DCE-MRI experimental technique and subsequent PK analysis of the temporal behavior of contrast agent in brain using compartmental exchange theory[15,57]. This analysis yields estimates of the microvascular parameters of cerebral gliomas in rats. There is extensive prior work in Ewing laboratory[1,2,5,13,58-61] using indicator dilution theory for investigating the dynamics (perfusion and permeability) of injected CA in tissue using PK models. By exploiting standard models, i.e., extended Patlak[17,18] and Logan[56] graphical methods, DCE-MRI data is modeled using a data-driven approach to model selection to yield parameters in embedded cerebral tumors and their microenvironment. The purpose of this chapter is to provide a theoretical backbone for this dissertation via a review of analytical approaches to DCE-MRI data.

2.1 Pharmacokinetic modelling and tracer kinetics

PK modelling is the process of evaluating the time course of absorption, distribution, metabolism, and excretion (ADME) of a tracer or a CA in a biological medium based on models of compartmental exchange[18,57,62]. The use of a CA in medical imaging has been a common practice for decades, augmented with the advent of imaging technologies like MRI, positron emission tomography (PET), computed tomography (CT), single photon emission computed tomography (SPECT) etc. While many imaging methods use contrast agents for diagnosis, techniques like MRI and PET also need

quantitative analysis of tracer dynamics[63,64] because it provides more detailed functional information.

CA transport kinetics and concentration depend on tissue type and pathology, microvasculature, and the nature of CA itself. The spatio-temporal behavior of a CA injected intravascularly and arriving in tissue via a capillary can be understood by using indicator dilution models that explain the time course of CA concentration in the blood and tissue with such parameters as blood flow, plasma volume (v_p), forward volumetric transfer constant (K^{trans}), and reverse transfer constant (k_{ep}). Thus, given an arterial input function (AIF), a tissue-specific response function connects measured signal intensity changes to physiological properties of tissue perfusion and permeability[65-67]. The analysis yields parameters that might be understood as biomarkers in cerebral pathophysiological interpretation in brain imaging studies[59,68,69].

Permeability, an important property in tracer kinetic modelling in a vasculature study, can be described by the Renkin-Crone model[67,70]. Renkin[70] in 1857, developed an equation elucidating permeability of a fluid flowing through a vasculature assuming a steady state condition. Nearly a hundred years later in 1953, Crone refined it by proposing a single-capillary model[67] that described permeability of a reference substance (e.g., a radiotracer) through a single pass in blood capillaries under a non-steady state condition. Applying Fick's law of conservation of mass flow and diffusion, Crone described the vascular permeability of an indicator in arterio-venous blood and developed a relationship between efflux rate constant, capillary blood flow, surface area and permeability, with the latter two coined as permeability-surface area (PS) product to indicate their integrated effect.

Tofts and Kermode[57] were the first to employ tracer-kinetic modelling in MRI for studying cerebral tissue porosity. They quantified the uptake and clearance of intravenously injected paramagnetic CA by translating it into a concentration-time graph using model equations the yielded a set of vascular parameters. Although they laid the groundwork for dynamic contrast–enhanced MRI of the BBB, their mathematical model included only one compartment, the CA leakage space, i.e., the EES, and thus plasma was treated only as an input source, not as a separate volume whose contribution to the MRI signal would be estimated.

Well before Tofts' work, Patlak et al.[18] proposed a simplified compartmental exchange model consisting of blood plasma and tissue extravascular space. In this analysis, the tracer kinetics could be expressed as a concentration-time graph for evaluating vascular permeability parameters – the well-known Patlak plot. This model assumes that the tracer is irreversibly trapped in a final extravascular compartment. In that case a linearization of the tracer uptake yields the transfer constant as the slope of the fit and the plasma volume as the intercept. This model was further improved (the extended Patlak model) to include the possibility of CA reflux from extracellular-extravascular space to blood plasma[17]. The Patlak models were initially applied in MRI in measuring the blood-to-brain transfer constant of gadolinium-diethylene-triaminepentaacetic acid (GD-DTPA) in a rat model of transient cerebral ischemia[71] and for studying the effects of water exchange mechanism on the forward transfer rate constant[72]. Tofts et al. further refined their work and standardized parameters and units in a two-compartment model that evolved into what is known as consensus model[15], also called the standard model (SM). The SM is exactly equivalent to the extended Patlak

model[17]. It is an error of scholarship that no mention is made of the extended Patlak model, which preceded the SM by 14 years.

In a DCE-MRI study by Haroon et al[73], the volumetric forward transfer constant of CA was compared using the original 2-parameter Tofts model and the first pass PK model (e.g. Patlak model discussed later). The Tofts model yielded a forward transfer constant an order of magnitude higher than the first-pass model. These results were echoed in Harrer[74], where the results for the SM were an order of magnitude lower than the Tofts model. The reason for that elevated K^{trans} (KTK ~ 0.248 min^{-1} in Haroon's notation) was that the vascular plasma volume was not considered as a separate compartment; in voxels with high blood volume the signal from intravascular contrast was misinterpreted to leakage, inflating K^{trans}. Additionally, the use of the vein as a measure of vascular input function instead of an artery might have affected the K^{trans} estimate.

The SM is the most frequently used model for PK modelling of DEC-MRI data in estimating microvascular parameters. The uptake and clearance of a CA concentration in tissue using SM can be described as:

$$C_t(t) = K^{trans} \int_0^t C_p(\tau) e^{-k_{ep}(t-\tau)} d\tau + v_p C_p(t) \qquad \textbf{2.1}$$

where $C_p(t)$ and $C_t(t)$ are the concentrations of CA in blood plasma and tissue respectively at time t, K^{trans} is the forward volume transfer constant between the blood plasma and the EES, k_{ep} is the reflux rate constant from EES to blood plasma, and v_p is the plasma volume fraction. The volume of EES per unit volume of tissue i.e., the interstitial volume fraction v_e, is a fraction between 0 and 1, and is calculated as the ratio

of K^{trans} to k_{ep}. It is usual to report v_e rather than k_{ep} as it has physical meaning and relates more directly to the state of the tissue[2,5]. However, since the temporal behavior of the data is the measure employed, k_{ep}, a rate constant, is the parameter that is estimated directly from the data.

2.2 Data-driven approach to model selection: an art in pharmacokinetics

An essential first step in drawing inferences from PK modeling of a dataset is the formulation of model selection procedure[2,5,58]. In DCE-MRI, the model selection process is a data-driven method for choosing an appropriate algorithm that best describes the observed concentration-time behavior of injected CA data. The hypothesized candidate model is fitted to the temporal/acquired DCE data and optimized using non-linear least square fitting[2,5]. Goodness of fit is balanced against complexity of the model in F-statistic for nested models and/or Akaike[75] or Bayesian[76] information criteria (AIC or BIC) statistical tools, thus keeping a balance between variance and bias in the parameters estimated. In DCE-MRI, under- or over-fitting can make results unreliable by not including elements of true variation or by capturing noise instead of physiology. Each additional parameter not only requires an independent information in the dataset to estimate it reliably but also increases the model complexity. Testing the competing models using criteria like the F-test (in the case of nested models) helps in assessing whether picking a more complex model improves the fit[2,77] enough to justify the higher-order model.

In this dissertation, Patlak[17] and Logan[55,56] graphical analyses were applied to T_1-weighted DCE-MRI data, and a data-driven approach to model selection was used for evaluating the suitability of the nested subsets of the full SM. An appropriate model was

selected according to F-statistic criterion with an empirically selected threshold[2,5,58,60,61]. By considering vascular and interstitial space as two major compartments in brain tissue, models 1,2, and 3 are proposed: the lower order model being the subset of the higher model. Model 1: normal vasculature with no leakage, just contrast agent in the vessel; Model 2: tissue region with contrast agent leakage without detectable back-flux to the vasculature, the original Patlak model; Model 3: tumor tissue with contrast agent leakage and measurable back-flux from EES to the vasculature, the extended Patlak or SM. For model selection, the F-statistic was generated in each case and compared to its reduced model alternative, the higher-order model was accepted if the F-statistic exceeded a set threshold, usually chosen at 30. This allowed an unambiguous selection of the model and model parameters best supported by the data. The model names are indicative of number of non-zero parameters that can be estimated from each model. Therefore, the only non-zero parameter estimated from Model 1 is v_p; the two non-zero parameters estimated from Model 2 are v_p and K^{trans}; the three non-zero parameters estimated from Model 3 are v_p, K^{trans}, and k_{ep}.

It is to be noted that the model selection process described above is a nested one, as each succeeding model cannot occur without the lower model being true, starting at Model 1 with CA delivery to tissue. Model 2 cannot occur without Model 1 in place, and Model 3 cannot occur without Model 2 in place. Thus, these consecutive conditions form a system of nested models in both physiological and statistical sense.

Each nested model (Model 1 or 2) was compared to the next-higher one by applying the F-statistic, with a higher-order model selected only if the statistic exceeded the selected threshold, allowing an unambiguous model selection with approximately

unbiased model parameters for the data considered. This approach produces a model selection map comprising three different tissue regions in the brain (Figure 2.1); model 1,2, and 3 with model 2 often bordering model 3 tumor. The individual parameter maps formed are a nearly complete picture of v_p where Model 1 is accepted, a partial map of K^{trans} where Model 2 or 3 is accepted, and a smaller map of v_e where Model 3 is accepted. Hence, a stable, reproducible data-driven estimates of DCE-MRI vascular parameters were obtained in embedded cerebral tumors by voxel-wise analysis using model selection paradigm[2,5,58-61,78]. An example of vascular parameter maps and the model selection map obtained via data-driven model selection procedure along with H&E-stained histopathology section for 9L cerebral gliosarcoma tumor is shown in Figure 2.1. The model selection map and the vascular parameter maps presented exhibit an excellent match to the post-contrast T_1-weighted image delineating the extent and location of the tumor, and the corresponding H&E histopathology.

2.3 Arterial input function

The arterial input function (AIF) describes the CA concentration in arterial blood over time. It is a measure of delivery of CA to the tissue by its feeding arteries after a bolus injection. The transient response by the tissue manifests as signal change which depends on the shape of the input pulse[79,80]. Figure 2.2 shows a schematic of input function with the first-pass of bolus injection representing a unit impulse and the resulting smeared-out response in the tissue, also called the tissue concentration curve.

In DCE-MRI, an accurate estimation of such tissue perfusion measures as cerebral blood flow (CBF), cerebral blood volume (CBV), mean transit time (MTT) etc., and vascular permeability-based measures (e.g., K^{trans}. K_{ep}), requires a reliable estimate and

shape of vascular input function to correctly model the behavior of CA in the tissue[79-81]. In this work, a group-averaged radiological AIF estimated from previous investigation[82] was scaled to the contralateral normal brain hemisphere caudate putamen plasma volume (1% of entire plasma volume in rat brain[83]). In detail: the starting point of the AIF was aligned with the first appearance of CA in contralateral normal brain tissue and a global starting point for parameter estimation was selected, usually one or two points after the arrival of CA. The last ~7 minutes of data were integrated, and the group-averaged input function scaled to this integral under the assumption that the plasma volume of the caudate putamen was 1%. This scaled input function was then used as an estimate of the AIF for each DCE study[2,60].

2.4 Patlak and Logan graphical methods: a powerful tool in data linearization

As noted, Patlak and Logan graphical analyses have been extensively used in imaging modalities, including DCE-MRI, for decades[2,5,58-61]. Herein the theoretical aspects and their role in DCE-MRI were briefly discussed.

2.4.1 The Patlak plot

The Patlak graphical method is a powerful analytical tool in common use in other modalities, e.g. PET, where the linearity of the fitted data infers that the underlying model correctly describes the temporal behavior of the data. In present work, the original 2-parameter Patlak equivalent model (Model 2), where CA enters the EES but doesn't reflux back to the vasculature, the kinetics can be modeled by the equation:

$$C_t(t) = K^{trans} \int_0^t C_p(\tau)\, d\tau + v_p C_p(t) \qquad \textbf{2.2}$$

where the symbols have their usual meanings as noted. Equation [2.2] is a special case of equation [2.1], with $k_{ep} = 0$, i.e. when CA reflux is not measurable.

Reorganizing equation [2.2] and plotting the ratio $C_t(t)/C_p(t)$ (ordinate) versus $\frac{\int_0^t C_p(\tau)\, d\tau}{C_p(t)}$ (abscissa with units of time, often referred as 'stretch time') yields a linear relationship with a slope of K^{trans} and an intercept of v_p.

In the case where CA refluxes back to the blood plasma from the EES, the full model of equation [2.1] must be used and the variable $k_{ep}(\tau)$ accounts for the back-flux. It can be iteratively adjusted in order to yield the best-fit approximation of a straight line to the data, leading to Model 3 consideration or the full SM[2,5,15,17,58]. Thus, a graph of $C_t(t)/C_p(t)$ versus $\frac{\int_0^t e^{-k_{ep}(\tau)} C_p(\tau)\, d\tau}{C_p(t)}$ yields an estimate of K^{trans}, k_{ep}, and v_p. Of note, a DCE-MRI estimate of v_e is only possible in Model 3 region. Figure 2.3 illustrates the CA concentration-time data fits using a 2-parameter lower order model (Model 2, the original Patlak) and a 3-parameter higher order model (Model 3, extended Patlak). It is evident from the graph that Model 2 fit (the curved graph indicated by a thin arrow) essentially overlaps with Model 3 fit (linear graph indicated by a thick block arrow) in the lower portion of the fit showing that Model 2 forms a nested subset of Model 3. A comprehensive analysis on Patlak plot linearization using SM can be found in Figure 4 of publication by Aryal et al.[60], Figures 5,6,8 of Ewing et al[1].

2.4.2 The Logan plot

The Logan graphical approach is a method of evaluating tracer kinetics when it is reversibly trapped in the tissue compartment. This method was widely used in PET

imaging for quantitative analysis of neuroreceptors in the brain[55,56], but can be used in MRI imaging as well. The Logan graphical method was first applied to MRI[60,61] to estimate the CA distribution volume in cerebral tumors using DCE imaging. Assuming that the CA leaks from the vasculature to the EES in an amount sufficient to reflux back to the blood plasma, a steady state can be reached when the concentration of CA in vascular compartment equilibrates with that of interstitial compartment. The slope of the line linearizing these two CA uptakes provides a reliable estimate of V_D for the region of interest. Hence, the Logan plot estimate of V_D can be obtained only in Model 3 region. Mathematically, the linearization equation between these two CA uptakes can be expressed as:

$$\frac{\int_0^t C_t(\tau)\, d\tau}{C_t(t)} = V_D \frac{\int_0^t C_p(\tau)\, d\tau}{C_t(t)} + \text{Const} \qquad \textbf{2.3}$$

where the symbols have their usual meanings, with V_D, the fractional distribution volume which is mathematically equal to the sum of v_e and v_p, i.e., $V_D = v_e + v_p$, and Const is an arbitrary constant. If there is a time after which the plot of $\frac{\int_0^t C_t(\tau)\, d\tau}{C_t(t)}$ versus $\frac{\int_0^t C_p(\tau)\, d\tau}{C_t(t)}$ is approximately linear, the slope of the fitted straight line gives V_D. The Logan plot linearization example using DCE imaging can be found in Figure 2 of publication[61], Figure 4 (bottom) of publication by Aryal et. al,[60], Figure 7 of Ewing et. al[1].

The Logan plot fits a different portion of the data in the DCE-MRI study than the SM: the SM depends on changes in the response function (relative to the input function) to estimate the rate parameters K^{trans} and k_{ep}, while the Logan analysis demands that the response function doesn't change relative to the input function. Thus, the two analyses fit much different portions of the input-response data, although they both require a measure

of the data from time t=0, see the reference Aryal et al[60]. An example of Logan graphical fit to concentration-time data of injected CA is shown in Figure 2.4; the slope of the fitted straight line provides an estimate of peritumoral distribution volume, V_D, in this case.

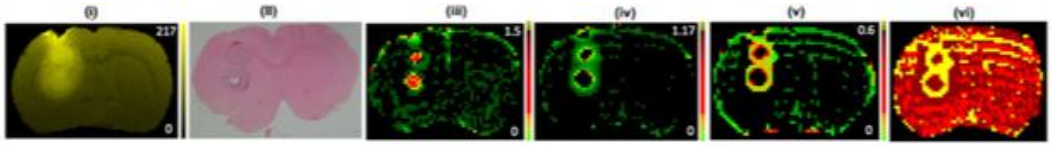

Figure 2.1: DCE-MRI derived parametric maps produced by data-driven approach of model selection in cerebral rat 9L gliosarcoma tumors. From the left: (i) T_1-weighted post contrast high resolution image showing the tumor extent and location, (ii) H&E histopathology section of the tumor, maps of (iii) v_p, (iv) K^{trans}, (v) v_e, (vi) model selection. For the model selection map, yellow is Model 3 acceptance, dark red is Model 2 acceptance, red is Model 1 acceptance. The color scale ranges are displayed on each vascular parameter.

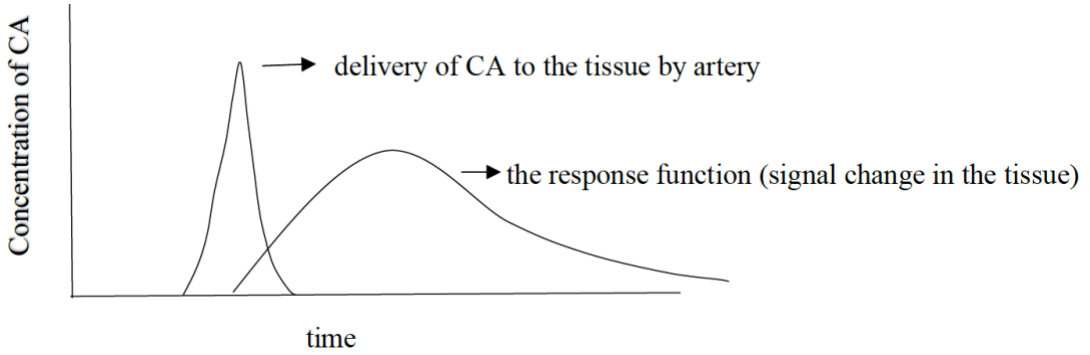

Figure 2.2: Graphical representation of an AIF and the response curve. The first peak showing the shape of unit impulse in bloodstream, and the tissue response curve lagging behind that. The CA takes some time to diffuse from the blood into the tissue, hence time delayed response.

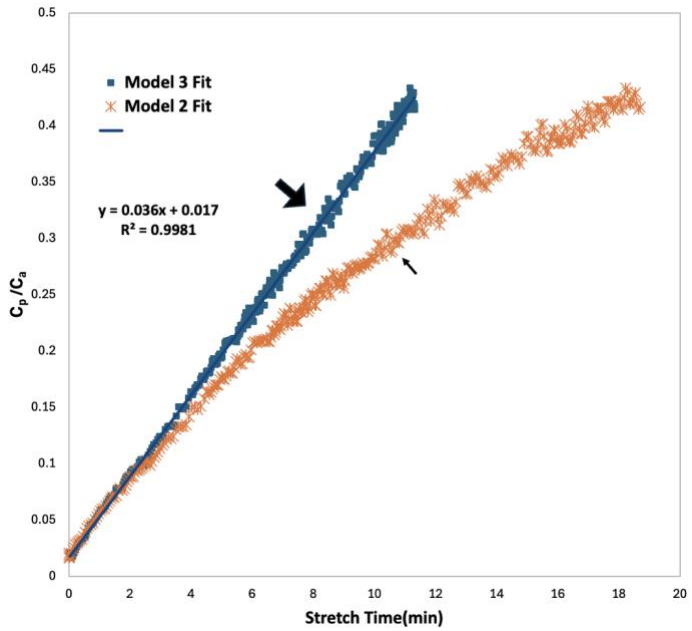

Figure 2.3: CA concentration-time data fitting using Model 2 (Patlak, concvex curve) as indicated by thin block arrow and the Model 3 fit (extended Patlak, linear curve) as indicated by thick block arrow. Note the initial lower portion of the fits where the two models essentially overlap explaining how Model 2 forms a nested subset of Model 3.

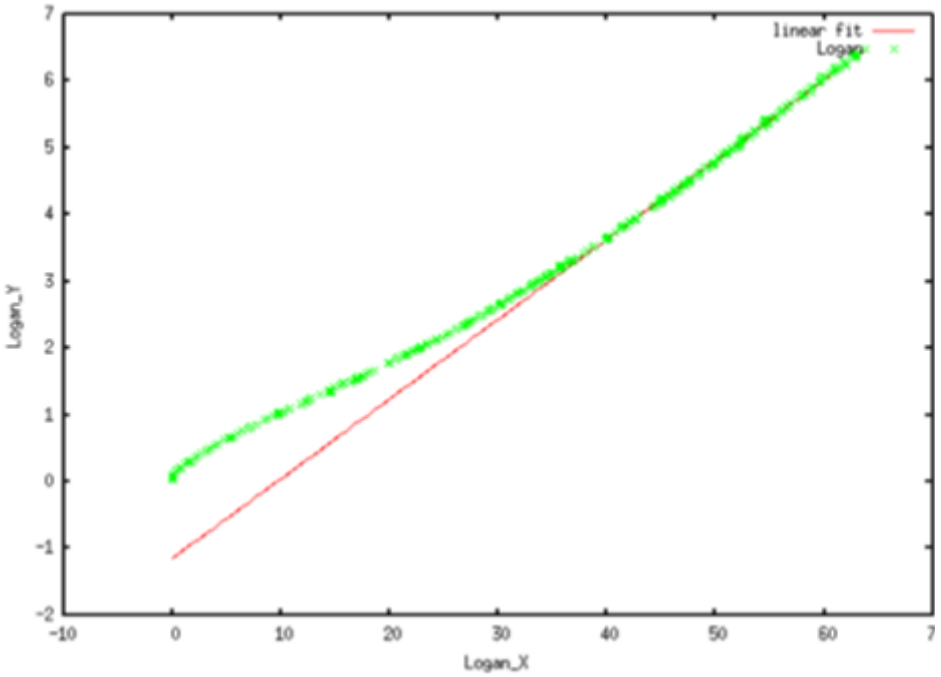

Figure: 2.4 Graphical analysis of data using Logan plot estimates for evaluating distribution volume (CA concentration on y- and time on x-axis). The solid line shows the linear fitting of the data; the slope of the fitted straight line provides an estimate of distribution volume. In this particular example, the straight-line fitting was made in the range 40:65 approximately, with a slope of 0.1183, equivalent to the distribution volume of 11.83%.

CHAPTER 3

DCE-MRI: ROLE AND SIGNIFICANCE IN CEREBRAL GLIOMA

In this chapter, the role of DCE-MRI parametric estimation in characterizing cerebral glioma physiology is presented, including how the DCE-MRI derived tumor microenvironment parameters might relate to treatment outcome. Particularly, a relation between peritumoral interstitial tissue space and the associated fluid flux have shown promise in explaining GBM tumor mechanics and their relation to tumor infiltration[1,60,84]. How these parameters behave in pre-clinical models of embedded cerebral glioma, e.g. PDOX or 9L tumors, may well be relevant to their response to therapy, especially in the context of highly elevated fluid pressures.

3.1 MRI and cerebral glioma physiology

Over 80% of all intracranial primary tumors in adults are gliomas, and about half of them are GBMs[85,86]. The overall incidence rate of malignant gliomas in the U.S.A. is about 5–8 cases per 100,000 people per year[87]. Despite a rigorous therapeutic approach, GBM still persists as the most challenging primary cerebral malignancy with median survival of about 15-23 months and a 5-year survival in less than 6% of cases[86-89]. Survival hasn't significantly improved over the last decades because of the resistance of GBMs to all conventional and novel treatments; recurrence is a near certainty[22,90]. The current standard treatment of GBMs is the maximal surgical resection followed by Temozolomide and radiation therapy for six weeks, and adjuvant TMZ as needed[27,29,30]; still these tumors continue to be lethal for nearly all patients.

Tumor physiology differs from that of the normal tissues in its hypoxic microenvironment and leaky blood vessels, escalated interstitial fluid pressure, impaired lymphatic drainage, extracellular acidosis, regional ischemia, and neo-angiogenesis[85,89-91]. The BBB normally isolates the brain parenchyma, forming an "immunologically privileged moiety."[92] A usually reliable marker of malignant gliomas is the disruption of the BBB. Compared to normal brain, tumor vasculature's incompetent vasculature leads to a breakdown of the microvascular osmolar gradient, increased TIFP, edema, hypoxia, necrosis, and tumor exudate flow.

The effective treatment of aggressive gliomas is challenged by their incomplete surgical resection because of the brain anatomy, aggressive cell proliferation and infiltration into surrounding normal brain, persistent tumor angiogenesis fostering tumor growth, etc[31,85,89]. Decades of research has established MRI as a powerful, non-invasive imaging modality being widely used in diagnosis and biomedical research for the initial diagnosis of tumors of the central nervous system (CNS) and brain, including a functional assessment of response to therapies[8,10,93-95]. A valuable contribution of functional imaging modalities in brain tumor research is their ability to non-invasively assess such tumor physiological properties as vascular permeability, perfusion, and cellularity[3,93]. MRI methods such as DCE-MRI, MR spectroscopy, diffusion-weighted imaging etc., have evolved as promising tools in evaluating tumor pathophysiology. DCE-MRI evaluates tumor vascularization, angiogenesis, and hemodynamics by probing CA kinetics, MR spectroscopy reflects tumor metabolism and helps distinguish tumor from normal tissue and tumor grading; and diffusion-weighting imaging characterizes tumor cellularity and edema by measuring water motion [10,60,94,96,97]. Tissue properties undergo continuous

changes with tumor growth and therapy that may well be reflected in vascular and tumor microenvironment parameters[10]. Thus, DCE-MRI provides the tools for studying the BBB and tumor microenvironment of cerebral tumors in rest and during the testing of novel therapies[41,57,59,69,98]. Multiparametric DCE-MRI in recent years has been established as a credible tumor biomarker due to its ability to accurately quantify tumor perfusion and permeability and detect early tumor response to therapeutic intervention[13,69,93,95,98-100]. Therefore, an assessment of MRI-derived imaging biomarkers can serve in devising a tumor specific, personalized treatment plan, potentially improving the patient outcome.

3.2 DCE-MRI biomarkers for tumor therapeutic response

Presently, DCE-MRI usage has increased in both pre-clinical and clinical research as it can provide direct insights into such aspects of glioma pathology as tumor vascular characteristics and function, disease progression, treatment response etc[101,102]. It can characterize tumor vasculature and cellularity, and is sensitive to changes in blood volume, blood flow and the increased vascular permeability associated with tumor angiogenesis[60,103,104]. Chapter 2 describes how DCE-MRI data can be processed to produce high-resolution maps of vascular plasma volume, transfer constant, and interstitial volume fraction. This is a common approach used in pre-clinical studies[2] and humans[5]. Each of these parameter estimates have potential to correlate with physiological and angiogenic processes and are associated with treatment outcomes[13,59,98,99]. DCE-MRI-derived parameters have shown strong correlation with histopathological features such as microvessel density, permeability, and extracellular matrix composition**,** thereby supporting their use as imaging biomarkers in cerebral tumors[11,12,37,98,99]. Importantly,

longitudinal changes in DCE-MRI parameters during the treatment can serve as early indicators of therapeutic response**,** making DCE-MRI a valuable tool for evaluating treatment efficacy in preclinical glioma models and in clinical trials[53,102,105]. The reproducibility and histological relevance of DCE-MRI measurements have made this technique central to the noninvasive assessment of GBM progression and therapeutic monitoring, both in animal models and human patients[106]**.** These metrics have been validated as reliable biomarkers for monitoring therapeutic effects[13,95,98,107,108] and can be used to predict the effectiveness of anticancer therapies prior to the treatment[109].

In preclinical glioma studies, DCE-MRI biomarkers have proven to be reliable indicators, showing strong associations with tumor grade[110,111] and a direct correlation with survival outcomes[112]. Unlike histological analysis (which requires euthanizing animals), it allows non-invasive, real-time monitoring of tumor progression and therapeutic response over time, helping clinicians tailor treatments based on real-time tumor response. In recent years, research has emphasized translational relevancy, suggesting that the outcomes from pre-clinical DCE-MRI studies can be applied to clinical trials in humans[8]. Moreover, their direct correlation with survival and glioma grading have strengthened their potential in reducing reliance on invasive biopsies[110-113]. Because of these advantages, efforts are ongoing for standardizing imaging protocols, improving data analysis methods, and integrating DCE-MRI into clinical practice[114].

3.3 Tumor distribution volume (V_D): key to cerebral tumor physiology

High-grade gliomas like GBMs, are highly infiltrative and lack a well-defined tumor boundary in conventional imaging modalities[9,115,116]. Tumor cells often extend beyond the contrast-enhancing core visible on MRI[117], infiltrating the peritumoral area

and causing high chance of recurrence**.** Tumor-induced vasogenic edema in GBMs expands the extracellular space affecting fluid dynamics in the peritumoral area[115]. As GBMs have an elevated IFP and a necrotic tumor core resulting from vascular collapse, the bulk of the tumor usually remains in an under-perfused state. The periphery of the tumor, spanning a space that is relatively rich in vasculature, presents key vascular and microenvironmental properties and is critically important in explaining glioma physiology. In this region, a DCE-MRI measure of tumor distribution volume might be extremely useful in assessing the extracellular space extension, tumor infiltration, and peritumor compression[1], providing critical parameters for understanding tumor progression and treatment response[116,117]. Aryal et. al[60] studied U251 cerebral gliomas in rats and found that interstitial volume fraction and the extracellular volume fraction (i.e., distribution volume), were both highly correlated with tumor cellularity. The study also showed that the estimate of distribution volume, V_D, agreed with the estimated sum of interstitial volume fraction and plasma volume fraction, as it should if it was a true measure of extracellular volume fraction.

In immune-suppressed rats, Ewing and colleagues[1] estimated V_D in the leaky rim of U251N cerebral tumors (the porosity) and in the immediately adjacent outer ring, which is mostly normal tissue, and showed that the distribution volume immediately outside the leaky tumor rim was approximately half of that in the inner leaky rim. The exudate flow and resulting flux across the boundary of the tumor were also estimated using the washout rate of the CA in the interstitium. The analysis revealed that the peritumoral compressive forces governs the tumor physiology, suggesting that local physiology and mechanical properties move cellular phenotypes towards proliferation

and invasion[118,119]. Further, tumor perfusion was mainly regulated by compression of the tumor periphery, and the exudate flow was controlled by perfusion pressure[1]. Hence, it turns out that compression of the tumor periphery, tumor exudate flow/interstitial fluid flow, and TIFP are all interrelated and change simultaneously according to the mechanical dynamics of the tumor and its surrounding. This suggests TIFP may correlate with tumor distribution volume and the flux at tumor rim.

3.4 Peritumoral flux and distribution volume in an embedded glioma tumor

As noted, DCE-MRI derived tumor distribution volume is of growing interest in that it can serve as important biomarker in cerebral glioma physiology characterization. Aryal and colleagues[60] first introduced the concept of tumor distribution volume in DCE-MRI and correlated it with tumor cellularity. Ewing and colleagues[1] further extended the analysis in U251N cerebral glioma model and showed that at the leaky rim of the tumor V_D and the exudate flux were highly correlated as shown in Figure 3.1, with an R^2 value of 0.9. This strongly implies V_D at the rim of the tumor controls tumor exudate flow[1]. The evaluation of peritumoral flux and its dynamics in an elevated fluid pressure environment have been appreciated by recent computational studies in explaining biphasic status of glioma physiology[84,120]. The strong positive correlation between V_D and Flux is a tumor biomarker not only for primary disease. Acharya et al[54]., have demonstrated a similar correlation for a recurrent PDOX glioma model as well. Testing the relationship for the case of treated gliomas would be interesting and could provide a clue for addressing treatment response in these highly heterogenous gliomas. Moreover, studies have indicated that peritumoral edema can serves as an independent predictive factor of recurrence patterns and recurrence-free survival for high-grade gliomas[115,121].

3.5 Tumor interstitial fluid pressure as a tumor response biomarker

In solid tumors, including brain tumors, interstitial fluid pressure is characteristically elevated. This arises primarily from abnormalities in tumor vasculature, which is typically tortuous, irregular, and hyperpermeable, resulting in fluid and macromolecule leakage into the interstitial space[25,48]. The imbalance between hydrostatic and oncotic pressures across the vessel wall, compounded by impaired vascular function and reduced blood flow, further contributes to fluid accumulation in the interstitial space[26,49]. In many tumor types, stromal fibroblasts can enhance IFP through increased contractility of the extracellular matrix[122], although this mechanism may be less pronounced in the brain, where fibroblasts are scarce. The rapid proliferation of tumor cells generates solid stress that compresses intra- and extra-tumoral blood vessels, reducing perfusion and sometimes collapsing vascular segments[45]. Meanwhile, the abnormally high MVP within surviving vessels, together with their leakiness, drives fluid filtration into the interstitium, contributing to elevated IFP. Because tumors lack efficient lymphatic drainage (and brain has no lymphatics, *per se*), the accumulated fluid cannot be cleared, leading to persistently high IFP[123]. Thus, TIFP is primarily governed by MVP. Because IFP rises until it approximates MVP, the loss of pressure gradients impairs perfusion, fluid and drug transport, and contributes to hypoxia and therapeutic resistance[26,45,123]. Moreover, elevated IFP in solid tumors creates outward fluid flow at the tumor margins, which can facilitate the transport of tumor cells, growth factors, and proteolytic enzymes into the surrounding normal tissue and lymphatic vessels or other clearance volumes, thereby promoting local invasion and metastatic spread[124,125].

Elevated TIFP is an important physiological biomarker and an indicator of tumor aggressiveness in human and experimental tumors that has implications for anticancer therapies and subsequent patient outcomes[40,41,52,126]. It is one of the major hindrances in the delivery of chemotherapy drugs and because it is associated with hypoxia, impedes the effectiveness of radiotherapy[40,41,126]. A clinical study conducted on melanoma and lymphoma patients showed that lower TIFP was associated with patients who best responded either to chemo- or immunotherapy, whereas non-responders to either of the therapies had higher TIFP[127]. Tumors exhibiting high IFP have been found to have poor prognosis after radiation treatment in cervix cancer patients and in melanoma xenografts[127,128]. Jain et. al[49,52] and others[129] have shown that TIFP decreases in both chemo- and radiotherapy in several human and experimental tumors. A preclinical study[52] conducted on mice carrying human colon adenocarcinoma xenograft showed a decrease in IFP in tumors treated with radiation dose above certain threshold. Another preclinical study[39] involving varieties of tumor models (human xenograft or induced or syngeneic mouse model), either in orthotopic or ectopic environment on nude mice showed significantly decreased TIFP after administering chemotherapeutic drugs. Hence, ongoing research has focused on understanding TIFP dynamics and identifying tumor physiology that may correlate. These circumstances imply that ongoing multimodality treatment of gliomas with elevated IFP is entangled with tumor physiology and microenvironment and needs to be unraveled to optimize therapeutic efficacy.

Using DCE-MRI I investigated TIFP dynamics and their correlations with tumor distribution volume and exudate flux in a group of naïve and RT-treated 9L syngeneic

tumors . I will examine these highly correlated parameters to determine whether they reflect changes in glioma physiology in association with TIFP.

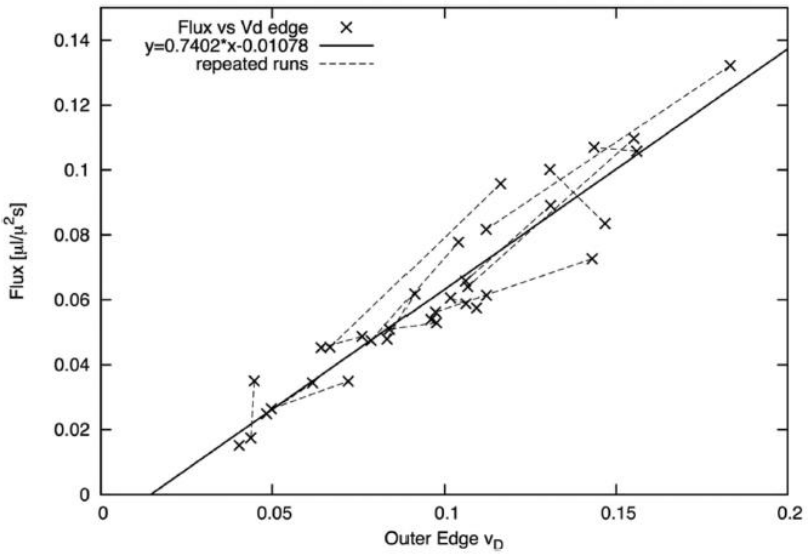

Figure 3.1 Graph showing relation between distribution volume at the outer edge of the tumor and the peritumoral flux with correlation coefficient, R^2=0.9 (Figure copied from Ewing et. al[1]). The study was conducted on U251N glioma model with each study separated by 24-hour interval. The dashed lines connecting two points are the repeated studies from the same animal.

CHAPTER 4

ERROR PROPAGATION IN DCE-MRI

Errors are inherent in any imaging system, including MRI, due to limitations in hardware design, electronic stability, and environment. In MRI, as in all processes, errors arise primarily from two categories of errors: systematic and random-like[7,130]. Systematic errors are consistent, reproducible biases that shift parameter estimates away from their true values, thereby affecting accuracy. These typically originate from hardware and sequence imperfections (such as flip angle miscalibration, Bo instability generated by eddy currents, B1 inhomogeneity, gradient non-linearities, or spatially varying coil sensitivity), from assumptions in modeling (e.g., inaccurate baseline T_1, errors in arterial input function estimation, or use of an inappropriate pharmacokinetic model), and from contrast agent–related factors (including nonlinear relaxivity at high concentrations or inaccurate dosing etc.)[6,7]. In contrast, random errors are stochastic fluctuations that reduce precision without introducing a consistent bias. They arise from thermal noise in the MR signal[131], physiological variability such as cardiac pulsation, respiration, and subject motion[132], as well as small differences in bolus arrival or limitations in temporal sampling[6]. Together, systematic errors undermine the accuracy of DCE-MRI biomarkers by consistently skewing their values, while random errors limit their precision by increasing variability across voxels or repeated scans.

In DCE-MRI, these errors are particularly critical as they can affect signal intensity measurements, pharmacokinetic modeling, and parameter estimation[6,7], potentially leading to misinterpretations of physiological biomarkers and pathology. One

such significant issue is the baseline signal drift, which may result from RF coil heating, B_0 field instability, or other hardware- and system-related fluctuations that alter signal intensity over time[6,7,21,133-136]. In this chapter, key sources of error in MRI systems, with a particular focus on baseline signal drift during DCE data acquisition, as well as strategies for mitigating and correcting these errors to improve image fidelity and diagnostic accuracy is presented.

4.1 Sources of error in MRI

As noted, errors are an integral to understanding the output of an MRI system. Identifying and assessing sources of error is crucial in developing a robust scanning protocol and pulse sequence, and in appropriately assessing random-like errors and identifying and removing or correcting for systematic errors. Potential sources of error in MRI systems can be diverse and may be broadly categorized as system-, acquisition-, physiological-and motion-induced[132].Subject movement and hemodynamic variability are generally considered random-like errors (non-systematic) from the scanner's perspective, however, they can introduce structured or repeatable artifacts that resemble systematic errors, e.g., ghosting, blurring. Each of the errors can distort underlying imaging, affecting both qualitative and quantitative imaging.

4.1.1 System-related errors

Absent subject movement, systematic errors in MRI are primarily hardware related. Although intended, the main magnetic field (B_0) inside the magnet bore is never uniform. Magnetic field variation due to B_0, inhomogeneities inside the imaging volume, can cause spatial variation in resonance frequency leading to geometric distortions. Similarly, applied gradient fields are not perfectly linear across the field of view which

causes gradient nonlinearities leading to spatial distortions[137]. At ultra-high field strengths (7T and above), particularly during high duty-cycle imaging, radiofrequency (RF) receiver coils may undergo heating, which alters their impedance and sensitivity. Moreover, the surface coil has non-uniform spatial sensitivity, making each voxel's signal dependent on coil proximity to the sample affecting signal uniformity[138]. Several other possible biases including incorrect system calibration (RF power and receiver gain), mechanical vibrations during gradient switching[139], inefficient shimming, image reconstruction algorithms etc. To rule out the chances of error and achieve optimized image quality, sources of bias should be identified and their magnitude estimated before deploying any imaging protocol.

4.1.2 Acquisition related errors

Artifacts or inaccuracies can also be introduced during the image acquisition process arising from sequence design, scan configuration, operator set-up etc.; these are acquisition-related errors. Thermal noise arising from electrical components (e.g., RF coils, amplifiers) and the object undergoing scan, can manifest as random fluctuation in the signal intensity limiting SNR degrading the image quality. Phase noise arising from phase-sensitive applications such as phase-contrast imaging[140,141] and susceptibility-weighted imaging techniques[142], is another key error source in this category. Rapid switching of RF gradients employed for encoding diffusion information can induce eddy currents in resonant circuit components[20,143] or nearby conductive materials leading to magnetic field distortion producing distorted images. Similarly, partial volume effect, aliasing, truncation artifacts are other artifacts that result from imperfections during data acquisition.

4.1.3 Physiological and motion-induced errors

As in every imaging modality, subject motion is an integrated part of error source in MRI too, which commonly manifests as motion artifacts in the images. Although there are situations where sensitivity to water molecules movement or blood flow are appreciated[140] (e.g., DWI in brain or stroke imaging) in generating useful image contrast, the bulk motion of an imaging volume (e.g., heart or lung movement) presents a significant source of error that may require rigorous corrections during image reconstruction. Subject motion leading to ghosting and blurring, and fluid flow generating phase shifts and signal loss are common consequences of motion related errors[144,145].

4.2 Error propagation impacts in DCE-MRI

As noted, DCE-MRI is a quantitative technique for estimating tissue perfusion and vascular permeability by analyzing the contrast agent kinetics. Error propagation in DCE-MRI[2,5,130,146-148] is a critical concern, as small uncertainties in signal can result in significant inaccuracies in the estimation of permeability parameters such as K^{trans} and v_e which carry physiological significance in brain tumor study. Ewing et. al[2,5] have described numerous potential sources of systematic errors and artifacts for a 7T system highlighting how the errors are introduced into the estimation of critical parameters like AIF, flip angle etc., and then get propagated to DCE-pharmacokinetic calculations, leading to erroneous vascular parameter estimation and a serious misinterpretation. These errors can emanate from multiple sources, viz, thermal noise, subject motion, partial volume effects, including system-related instabilities such as RF coil heating[21,136,138]. Generally, heating of RF receiver coil components (preamplifier components and PIN

diodes) may produce a baseline signal amplitude decrease caused by an increase in the resistance in both passive and active components, and a subsequent loss of quality factor (Q). This can introduce systematic deviations in estimation of pre- and post-contrast T_1 relaxation time, tip angle etc., which propagates into the concentration-time curve, affecting tracer kinetic modelling and pharmacokinetic parameter estimation[6,7,130]. Also, the non-linearity of signal to CA concentration conversion amplifies uncertainties present in the measured signal[149]. Hence, any minute drift/error in measured signal can be easily transmitted in subsequent calculations of CA concentration estimation, particularly in regions/situations with low baseline signal. Therefore, a robust analysis of measured MR signal should be conducted for any unexpected deviations, and correction strategy is of critical concern to address such issue and produce reliable measures of vascular parameters that truly inform the associated pathology.

4.3 Mathematical formulation of error propagation in DCE-MRI

I will briefly describe the mathematical basis of error propagation in DCE-MRI. Discussed below are the most common parameters used in pharmacokinetic modelling of CA having the chance of introducing deviation or error in the measured signal and eventually gets propagated in several forms if uncorrected.

4.3.1 Error propagation through T_1-estimate

In DCE-MRI, the general assumption is that the CA concentration in tissue is approximately proportional to R_1, where $R_1 = 1/T_1$, T_1 being the longitudinal relaxation time in the tissue[2,5-7]. Mathematically,

$$\frac{1}{T_1} = \frac{1}{T_o} + \gamma_1 \, C_{tiss}(t) \qquad \textbf{4.1}$$

where, T_o and T_1 are the longitudinal relaxation time pre- and post- CA injection, $C_{tiss}(t)$ being the CA concentration in the tissue at time t, and γ_1 the reflexivity of CA.

Rearranging equation [4.1], we get an equivalent observation equation:

$$R_1(t) = R_o + \gamma_1 C_{tiss}(t) \quad \textbf{4.2}$$

If an error δR_o is introduced in baseline estimation (prior to CA administration) such that $R_o' = R_o + \delta R_o$, then equation [4.2] can be written as:

$$C_{tiss}'(t) = \frac{R_1(t) - R_o'}{\gamma_1} \quad \textbf{4.3}$$

Substituting R_o' in equation [4.3] gives,

$$C_{tiss}'(t) = \frac{R_1(t) - R_o}{\gamma_1} - \frac{\delta R_o}{\gamma_1}$$

$$C_{tiss}'(t) = C_{tiss}(t) - \frac{\delta R_o}{\gamma_1}$$

$$\delta C_{tiss}(t) = - \frac{\delta R_o}{\gamma_1} \quad \textbf{4.4}$$

From equation [4.4], it's clear that an incorrect T_o estimate leads to erroneous estimation of $C_{tiss}(t)$ affecting PK modelling leading to systematic bias in vascular parameter estimation.

4.3.2 Arterial input function sensitivity

In DCE-MRI pharmacokinetics, tissue CA concentration is derived using the standard model[2,5,15,16] as follows:

$$C_t(t) = K^{trans} \int_0^t C_p(\tau)\ e^{-k_{ep}(t-\tau)}\, d\tau + v_p C_p(t) \quad \textbf{4.5}$$

where, $C_t(t)$ is tissue CA concentration, and $C_p(t)$ is the plasma CA concentration, also referred to as the AIF, K^{trans} the forward volume transfer constant, k_{ep} is the reflux constant from EES to blood plasma. The integral in equation [4.5] describes how the plasma CA concentration spreads through the tissue over time. If an uncertainty is introduced in AIF measurement, say $\Delta C_p(t)$, the perturbed form of tissue concentration becomes:

$$\delta\Delta C_t(t) = \Delta K^{trans} \int_0^t \delta\Delta C_p(\tau)\ e^{-\Delta K^{trans}(t-\tau)/v_e}\, d\tau \qquad \textbf{4.6}$$

where, $k_{ep} = \frac{K^{trans}}{v_e}$, v_e is the interstitial volume fraction. If a bias is introduced in AIF measurement and produces scaling error, then the measured AIF can be represented as:

$$C_p^{meas}(t) = \alpha\, C_p(t) \qquad \textbf{4.7}$$

such that $\alpha \neq 1$. This will affect the estimation of K^{trans} and v_p linearly; let represent them as $K^{trans'}$ and $v_{p'}$. Equation [4.5] can then be fitted as:

$$C_t(t) = K^{trans'} \int_0^t C_p^{meas}(\tau)\ e^{-k_{ep}(t-\tau)}\, d\tau + v_{p'}\, C_p^{meas}(t) \qquad \textbf{4.8}$$

Again, substituting equation [4.7] on equation [4.8], we get:

$$C_t(t) = \alpha\, K^{trans'} \int_0^t C_p(\tau)\ e^{-k_{ep}(t-\tau)}\, d\tau + \alpha\, v_{p'}\, C_p(t) \qquad \textbf{4.9}$$

Comparing equation [4.9] to equation [4.5], the equality holds if

$K^{trans} = \alpha\, K^{trans'}$, and $v_p = \alpha\, v_{p'}$, leading to

$K^{trans'} = \frac{\alpha}{K^{trans}}$, and $v_{p'} = \frac{\alpha}{v_p}$

Therefore, if AIF is underestimated (say $\alpha < 1$), the fitted K^{trans} and v_p would be overestimated by a factor $1/\alpha$, hence a bias in C_p amplitude introduces an inverse proportional bias in K^{trans} and v_p .

4.4 Baseline signal drift in DCE-MRI

Thermal perturbations are common in MRI system, where the temperature changes in system components due to heating of RF coils, gradient coils, environmental conditions etc., influences SNR and is reflected in signal instability, image artifacts, and gain related issues[21,133]. Heating increases the impedance of the resonant circuit, decreasing Q and decreasing the signal amplitude. DCE-MRI uses high duty-cycle gradient echo sequences which can give significant power load to the MR hardware inducing significant heating in the receiver coil when the sequence is run for relatively long periods. Baseline signal amplitude drift can directly affect T_1 quantification introducing systematic bias and interferes accurate pharmacokinetic modeling qunatitation[2,5-7,146]. In a different perspective, as DCE-MRI exploiting spoiled gradient-echoes are primarily intended for accurate T_1-estimation, inadequate T_1-saturation failing to reach a true steady state before starting acquisition can also cause signal evolution in the first few frames, appearing as baseline signal drift[6,7,146,148].

4.5 Detecting baseline signal drift in MRI

As DCE-MRI is a T_1-sensitive quantitative method, obtaining a stable, unperturbed baseline signal prior to CA administration is a top priority for pharmacokinetic analysis. Otherwise, as discussed in section 4.3, any error in pre-contrast T_1 gets propagated across entire pharmacokinetics leading to erroneous parameter estimates. Therefore, detecting and characterizing baseline drift is an essential step to

ensure data quality and credibility. Described below are some baseline drift detection techniques.

4.5.1 Signal-to-noise ratio analysis

Careful analysis of SNR is important in detecting artifacts or signal instabilities in MRI imaging. Evaluating baseline SNR in a phantom over time is an essential first step in detecting inconsistencies because drifting systems often exhibit gradual SNR degradation. Visual inspection can be applied to observe the temporal behavior of the data. Plotting voxel-wise mean signal intensity across time for the pre-contrast period can provide an intuitive impression of signal quality. Drifting signal often appears as a monotonic deviation (upward or downward) from an expected flat baseline.

During extended DCE-MRI scans, heating of the receiver coil and associated receiver electronics, both caused by RF power deposition and continuous scanning activity, can alter their electrical properties, leading to gain instability. Specifically, temperature-dependent changes in resistance, inductance, and capacitance can modify the coil's quality factor and impedance, which in turn affect the amplifier's effective gain. This gradual gain shift manifests as a drift in signal amplitude across the dynamic series, potentially confounding quantitative analyses. These thermal effects can therefore compromise the SNR and temporal consistency of the MR signal. Such gain variations are particularly relevant in high-field or high-duty-cycle protocols where thermal loading is significant.

4.5.2 Statistical analysis of acquired MR signal

The Kolmogorov–Smirnov (K–S) test is a non-parametric statistical method that can be used to evaluate whether the temporal distribution of MR signal intensities in a

voxel follows a reference distribution, typically Gaussian noise, during the pre-contrast baseline period of a DCE-MRI scan. Particularly in the background regions where no signal contamination is expected, this test helps identify pure noise voxels**,** which are essential for estimating the noise floor and assessing baseline signal stability. While the noise phase is uniformly distributed with zero mean, the magnitude of noise in background voxels is expected to follow a Gaussian distribution in the real/imaginary components. By applying a signal amplitude threshold, background regions can be isolated, and the K–S test can then be used to assess whether their temporal fluctuations are consistent with noise. However, there is a risk of obtaining too few noise-only voxels for reliable analysis. In such cases, identifying truly uncontaminated noise points becomes challenging.

4.6 Noise analysis in a magnetic resonance system

Assessment of noise in any MR system is extremely important for variety of reasons. Apart from providing an idea about image quality, the performance of MR system such as receiver coil and other electronics in the resonant circuit can be evaluated by noise assessment[138,150]. The random (background) noise is primarily thermal in nature, arising from radiofrequency coil resistance, electronic noise in the preamplifier, and dielectric and inductive losses in the imaged object[138,151]. The most common form of noise inherent to the MR complex data is complex white noise characterized by Gaussian probability distribution. However, the scenario is different when magnitude images are considered where the noise distribution is no more Gaussian, but Rician[138,152].

In MRI systems, signal is detected in quadrature using receiver coils sensitive to magnetic flux in two orthogonal directions. For a phased-array coil having 2x2

configuration, four independent coils are positioned in mutually perpendicular arrangement. Each coil produces a complex signal (S) having Gaussian distribution: S = I + iW, where I is the real part and W is the 90^{o} phase shifted or imaginary part from each coil, and are summed in the complex domain. The associated white noise arising from thermal and shot noise in the receiver circuit is independent and identically distributed (iid) and is additive with zero mean. For magnitude images, the resultant signal is the modulus of the complex signal from each coil with Rician distributed noise. The probability distribution function (PDF) of a Rician distribution can be written as:

$$P(m, A, \sigma) = \frac{m}{\sigma^2} \exp\left(-\frac{m^2+A^2}{2\sigma^2}\right) I_o\left(\frac{mA}{\sigma^2}\right), \qquad m \geq 0$$

where, m is the magnitude of the magnitude image, A is the true signal amplitude or the magnitude of the complex signal, σ is the standard deviation of the Gaussian noise in each real and imaginary channel of the complex MRI signal, the exponential term is the probability density of a 2D Gaussian in polar coordinates, and I_o is the modified Bessel function of first kind (zero order) which governs the peakedness of the distribution. This PDF provides the likelihood of observing a magnitude value m, given a true signal A and noise level σ. There are two important possibilities depending on the value of true signal A:

Case I: No signal (A = 0)

$$P(m, A = 0, \sigma) = \frac{m}{\sigma^2} \exp\left(-\frac{m^2}{2\sigma^2}\right)$$

This reduces to Rayleigh distribution, which describes pure noise voxels (e.g., background (air) outside the object. A non-zero magnitude is possible due to noise, resulting in a positive bias in the signal amplitude.

Case II: High signal ($A >> \sigma$)

The Rician distribution becomes approximately Gaussian, centered around A, with standard deviation σ. In high-SNR regions, the noise appears Gaussian.

The most commonly applied method for estimating random noise is to use the background (air) noise around a uniform phantom. Noise is measured as the standard deviation of the pixel intensity from the four corners of the background image around the circular phantom. The choice of the corners as the ROI ensures the exclusion of structured noise from the subject along the phase and frequency direction. As the pixel distribution in this ROI follow the Rayleigh distribution (no signal), the standard deviation of the Gaussian noise in the phantom is calculated by dividing the Rayleigh standard deviation ($\sigma_{Ralyleigh}$) by a factor of 0.66. The main idea used for the assessment of baseline drift in this study also lies in the SNR analysis of the measured MR signal in a phantom in the initial baseline period. The signal amplitude was fitted using a 3-parameter logarithmic heuristic equation and a global correction factor applied to entire DCE-MRI profile.

CHAPTER 5

DCE-MRI TUMOR VASCULAR PARAMETERS IN TWO PRECLINICAL PATIENT-DERIVED ORTHOTOPIC XENOGRAFT MODELS OF GLIOBLASTOMA

This chapter describes the quantitative characterization of patient-derived orthotopic xenograft model of human glioblastoma using DCE-MRI method. The bulk of the material of this chapter is published in the journal NMR Biomedicine[54].

5.1 Introduction

High grade gliomas such as glioblastomas present with a poor prognosis and a median survival of about 15 months[22,90]. The current standard of treatment is safe maximal resection of contrast-enhancing tumor followed by chemoradiotherapy[29,30]. With a high failure rate of clinical trials on new treatments[34,89,153], there is an urgent need for ongoing development and testing of putative therapies. The concurrent development of animal models that closely represent the clinical presentation[31] are crucial to the development of effective treatments for GBM patients. Several preclinical hetero- and orthotopic models are presently being employed using either immortalized glioma cells lines, e.g., U251N, 9L, U87, or patient derived xenografts developed from clinical biopsy samples. Of them, patient derived orthotopic xenografts (PDOXs) produced by neurosphere cultures developed in serum-free media best reflect human gliomas in genotype[35,154]. Some can also be induced to reflect the human phenotype, in that the breakdown of the blood-brain barrier and ring contrast enhancement typical of human imaging studies can be obtained in the rodent brain by altering the local extracellular matrix (ECM) at the time of implantation[37].

Pharmacokinetic analysis using DCE-MRI imaging is frequently employed to evaluate microvascular parameters for a contrast agent[98,155-158,15,62]. Plasma volume fraction v_p, blood-to-tissue forward volumetric transfer constant (K^{trans}) and interstitial volume fraction (v_e) provide useful measures of tissue physiology. Additional novel DCE-MRI measures have been described by us – i.e., tumor distribution volume at the tumor rim (V_D) and the peritumoral flux[1]. Tumor blood flow by arterial spin labeling (ASL) and a measure of the apparent diffusion constant are also available. An understanding of these indices of tumor microenvironment in the context of the blood-brain barrier and blood-tumor barrier can aid in optimizing delivery of drugs and in measuring signatures of response to therapy. DCE-MRI holds promise for predicting drug distribution in GBMs[159-161], and can suggest methods for altering and improving regional delivery to this typically heterogeneous tumor[159,162] .

In this work, a set of nested models centered around the original two-parameter Patlak model[18] are employed, with the higher-order alternative being the three-parameter extended Patlak model[17] (i.e., the Standard Model (SM)[2,5]), and a one-parameter estimate of plasma volume the lower-order alternative. After a venous bolus injection of CA, the dynamically changing longitudinal relaxation rate (R_1) in tissue ($R_1 = \frac{1}{T_1}$, where T_1 is the longitudinal relaxation time) was used as a measure of tissue CA concentration versus time[60,61]. Given an arterial input function, voxel-by-voxel parametric maps of microvascular parameters were formed. A data-driven approach to model selection[2,5,58] balanced bias and variance in parametric estimates. In addition, in the regions where the extended Patlak model was valid, the portion of the dynamic data where the concentration of CA in plasma equilibrated with that of the interstitial space was

identified and a Logan plot was used to estimate the tumor extracellular space, i.e., the distribution volume V_D[56,60]. Further, by application of the principles of the Logan and Patlak models, an estimate could be made of V_D and tissue exudate flux in the mostly normal periphery of these embedded cerebral tumors[1].

Apparent diffusion coefficient (ADC) has been conventionally employed as a biomarker for solid tumors in evaluating treatment efficacy, progression vs treatment progression and to predict clinical outcomes[96,163-165]. Estimates of ADC were computed for the two models in this study, and comparisons were made with distribution spaces derived from DCE-MRI data to assess their potential correlation with this classical MRI index. TBF was measured to as an imaging indicator of oxygenation status of glioma.

The two PDOX gliomas reported herein, HF3016 (primary) and HF3177 (recurrent) from a male patient, have been extensively characterized and shown to preserve the molecular properties of the source human tumors[166]. The HF3016 cell line was O6-methylguanine-DNA methyl-transferase (MGMT) unmethylated, transcriptional subclass proneural and untreated at the time of tissue collection. The recurrent HF3177 tumor, obtained after the patient underwent temozolomide and radiation treatment, had transitioned to the mesenchymal subclass and was classified as a gliosarcoma.

In summary, a battery of physiological parameters is reported from MRI studies of two untreated PDOX gliomas grown in athymic rats. Those data are accompanied by detailed histological analyses of both models. These baseline physiological parameters are expected to aid in the testing of novel anti-glioma therapies.

5.2 Materials and methods

5.2.1 A review of tumor models in pre-clinical research

A thoroughly characterized pre-clinical tumor model is a pre-requisite in brain tumor research for testing novel drugs and therapeutics. Glioblastoma tumor physiology has been investigated using variety of murine tumor models having similar genetic backgrounds. Selecting a proper tumor model is extremely important as it will have consequences on validity and translatability on experimental results. A brief description of most commonly used tumor models for glioma, including their major advantages and disadvantages in summarizing tumor physiology is presented below.

5.2.2 U251N tumor model

U251 is a glioblastoma cell line derived from a 75-year-old male patient with GBM[167,168].This cell line exhibits several salient features of primary human glioblastoma, e.g., cellular atypia, mitotic figures, necrotic cores, and edema[32,168-170]. Genotypically, mutant tumor suppressor genes (p53) and PTEN (phosphatase and tensin homologue deleted on chromosome 10) are present but remain dormant[168]. As these cells are highly proliferative, their neurospheres often propagate to glioblastoma stem cells[169,171]. The majority of proliferating cells are stained positive for ki67[168,170]. U251s have been used in both subcutaneous (heterotopic) and intracranial (orthotopic) murine models[172]. In addition to a necrotic core, the tumor borders with enhanced rim on T_2-weighted imaging, and an intense rim on T_1-weighted images are MRI manifested salient features of these gliomas[168]. Similar to human GBMs, U251s usually respond to TMZ and radiation[169]. U251s are often used as a model to study GBM physiology and investigate new treatments modalities, including improvement on concurrent therapies, and in studying

effectiveness of drugs like TMZ, Cilengitide, Bevacizumab etc. against GBM malignancies. However, somewhat decreasing its value as an ideal glioma model, the long-term sub-clonal U251 cell cultures lack the genetic and molecular heterogeneity that characterizes human GBM[169,173].

5.2.3 9L tumor model

This syngeneic glioma model is murine in origin which was initially developed by repetitive administration of MNU in Fischer rats[168,174,175]. These tumor cells are transplanted into rats having similar genotype and intact immune system which provides a complete tumor microenvironment[168,169]. The 9L gliosarcoma model is in common use for investigating glioma physiology, testing new chemotherapy drugs and radiotherapy efficacy[168,176-179]. Although these cell lines exhibit several similarities to human GBMs (e.g., mutant p53 gene, infiltrative), they lack diffusely invasive cells[168,174], hence fail to express tumor suppressor genes like, PTEN[168]. In spite of its wide use, these tumor models may not be very promising for studying invasive glioma properties due to their susceptibility to genetic drift over time as occurs with many other immortalized tumor cell lines. However, being grown in an immune-competent rat, they may offer some unique advantages to study anti-glioma immune therapies, and good model to study gliosarcoma with mesenchymal modifications, typical of recurrent GBM.

5.2.4 Patient-derived xenograft (PDX) tumor model

The U251 and 9L models do not satisfactorily recapitulate all essential features of human GBMs, and drift both genotypically and phenotypically from human GBMs in many respects. For example, unlike human GBM, the invasion in U251 does not occur along white matter tracts[168,169]. Patient derived xenograft (PDX) are the tumor cells

directly taken from the human patient post-surgery, usually grown in serum free media, with or without including growth factors, can be either implanted in orthotopic or ectopic microenvironment[36,180-184]. The development of PDX models is driven by the belief that they serve as superior preclinical tools with improved ability to reflect human cancer behavior and predict patient responses to therapy. PDX models retain much of the primary histological and genetic properties of their donor tumor and remain stable across multiple mouse passages[36,169,185]. PDX glioma model reproduces the hallmark features of human GBM like, pseudopalisading necrosis, diffused infiltration to the contralateral brain through corpus callosum, nuclear atypia, high mitotic index, endovascular proliferation etc.; these have encouraged its use to measure and predict the therapeutic outcomes to novel therapeutics. PDX models hold promise for tailoring cancer treatments to individual patients. It has also been established that PDXs have shown clinically relevant responses to tested therapies like TMZ[169,185]. In spite of these promising aspects, the improvement in implantation procedures and the use of robust translational imaging modalities for evaluating imaging response biomarkers were still recommended as areas of prospective research[36]. Several studies[186,187] have suggested that Matrigel application during tumor implantation could help enhancing BBB breakdown and have better visualization in MRI when administered with the contrast. In this dissertation, PDX tumor derived from human GBM was orthotopically implanted with tumor extracellular matrix modified by Matrigel application at the time of implantation, and major microvascular parameter quantitative characterization attempted with DCE-MRI, a promising imaging modality both in clinical and pre-clinical setting. The produced

imaging biomarkers are unique and deserving in the sense that PDX cells for primary and recurrent were derived from the same patient.

5.2.5 Patient-derived orthotopic xenograft (PDOX) preparation and implantation

Resected glioblastoma tumor cell specimens were acquired with written consent from patients in accordance with the requirements of an Institutional Review Board protocol of HFH, and subsequently processed at the Hermelin Brain Tumor Center, HFH. The two PDOX cell lines were grown in a serum-free neurosphere medium that preserved their genotype and induced cancer-like stem cell (CSC) properties in the subsequent xenograft models[35,154]. Cells were suspended in phosphate buffered saline (PBS). For implantation, 3 x 10^5 cells in 5 µl PBS were mixed with 5 µl Matrigel with reduced growth factors (Corning Discover Labware, Inc., Bedford, MA) [37].

Tumor implantation and experimental procedures were approved by the Institutional Animal Care and Use Committee-approved protocol (IACUC) (#1288). The protocol ensured humane treatment of all animals, minimizing pain and discomfort during all procedures. The animals were under anesthesia during the MRI scans with constant warm air flow to maintain body temperature. The animals underwent humane sacrifice, euthanized under anesthesia while collecting brain specimen for histopathology. Fifteen female immune-compromised rats (Charles River, Frederick, MD) were assigned to the two tumor subgroups. Seven untreated rats (mean age: 125.4 ± 9.09 days) bearing HF3016 and eight (mean age: 143.5 ± 16.05 days) bearing HF3177 PDOX tumors were studied. Following published procedures[37,60,61], the animals were anesthetized with isoflurane gas mixture (4% for induction, 1.5% for maintenance, balance N_2O:O_2 = 2:1). Under aseptic conditions, the surgical area of head was swabbed with Betadine solution

and alcohol, the eyes coated with Lacri-lube (Allergan Inc., Madison, New Jersey), and the head immobilized in small animal stereotactic frame (Kopf, Cayunga, California). After draping, a 1 cm incision was made 2 mm right of the midline and the skull was exposed. A burr hole was drilled 3.5 mm to the right of bregma keeping the dura mater intact. A 10 µl Hamilton syringe with a 26-gauge needle containing 5 µl of tumor neurosphere cells suspended in PBS and an equal volume of Matrigel with reduced growth factors was lowered to a depth of 3.5 mm and then raised back to a depth of 2.5 mm, creating a pocket. Cells were slowly injected into this pocket over 5 min until the entire 10 µl volume was injected. The needle was withdrawn gently; the burr hole sealed with sterile bone wax and the scalp closed with nylon sutures. The rats were observed until ambulatory and then placed back to the home cages. Seven untreated rats bearing HF3016 and eight bearing HF3177 PDOX tumors were studied. DCE-MRI scans were performed 49.3±5.9 and 59.4±10.8 days after implantation (mean ± SEM) for HF3016 and HF3177 cell lines respectively.

5.2.6 Experimental preparation and protocol

All implanted rats were monitored by MRI (post contrast high resolution T_1-weighted imaging – see below) for tumor size and location. When tumors grew to about 3 to 4 mm in diameter, an MRI and a DCE-MRI study were performed, as previously described[1,13,41,60,61,95,97,98]. The lateral tail vein was used for CA administration, and the body temperature was maintained at 37ºC with warm air supply and monitored using a rectal probe. The rats were euthanized at the end of the DCE study and the brain removed for histology.

5.2.7 MRI study

MRI studies were performed in a Varian/Magnex (Santa Clara, California), 7 Tesla, 20 cm bore magnet with a Bruker console using Paravision 6.0. Gradient maximum strengths and rise times were 250 mT/m and 120 μs respectively. All MRI image sets were acquired with a 32 x 32 mm field of view. Transmit and receive coils were a Bruker Quadrature Birdcage (transmit) and a 4-channel phased-array surface coil receiver (Rapid MR International, Columbus OH).

T_1-weighted high-resolution images were acquired pre- and post-contrast injection using a RARE sequence for co-registration with post-mortem histopathology images. These images were acquired with the following parameters: 256 x 192 matrix size zero-filled to 256 x 256, 27 slices, 0.4 mm thickness, 0.1 mm slice gap, number of echoes (NE) = 3, echo spacing = 6.4 ms, number of averages (NA) = 8, flip angle = 90^o, TE/TR = 12.7/800 ms. Magnevist (gadopentetate dimeglumine; 0.25 mmol/kg, Bayer Healthcare, Wayne, New Jersey) was used as the contrast agent in 11 animals and Dotarem (gadoterate meglumine; 0.5 mmol/mL, Guerbet LLC, Princeton, NJ, USA) as the contrast agent in 4 animals. TBF was estimated in single central slice using arterial spin labelling (ASL) and a segmented echo planar imaging technique (two segments) using published methods[71,188] with the following parameters: 128 x 128 matrix size, 1mm thick slice, NA = 1, TE/TR=14/5000, Arterial labeling = 1s, Total time ~ 5 min. ADC data were acquired via diffusion weighted imaging (DWI) pulsed gradient spin-echo sequence in three directions (x, y, z). The ADC was estimated voxel-by-voxel using log linear fit of signal intensities. The DWI parameters were as follows: matrix size=128 x 64 zero-filled to 128 x 128, 15 slices, slice thickness = 0.8 mm with 0.2 mm gap, TR = 1500 ms, TE = 40 ms,

diffusion b-values = 0, 895, 1792 s/mm^2, gradient amplitude = 107 mT/m, gradient duration = 10 ms. Two consecutive Look-Locker (LL) sequences were run before injecting the contrast agent, and two were also run after the completion of the 10 min DCE-MRI sequence to generate pre- and post-contrast voxel-by-voxel maps of T_1 in the tissue. The LL sequence parameters were as follows: flip angle (FA) = 25^o, 128 x 96 matrix size zero-filled to 128 x 128, five 1.9 mm slices, 0.1 mm gap, NE = 24 inversion-recovery echoes, TR = 2000 ms. The DCE-MRI sequence used was a dual-echo spoiled gradient-echo sequence with 400 acquisitions at 1.55 s intervals, 128 x 64 matrix size zero-filled to 128 x 128, three 1.9 mm slices with 0.1 mm gap, FA = 18^o, NE=2, NA=1, TE=2.0 and 4.0 ms, TR=24.2 ms, spectral width=150 kHz. The CA was injected by hand push via tail about one minute after the start of the sequence. The DCE-MRI total run time was ~ 10 min. Selected rats from each neurosphere cell line cohort were scanned at multiple time intervals to follow tumor growth patterns for recognizing unexpected tumor burden increases that would necessitate unplanned animal euthanasia and loss of data.

5.2.8 DCE analysis and tumor vascular parameters

Pharmacokinetic analysis of injected CA using compartmental exchange theory is the main tool used in analyzing the DCE-MRI data. After injection of CA, R_1, is approximately proportional to the CA concentration in tissue[189]. Prior to DCE-MRI and immediately after it, pre- and post-contrast LL sequences were run to provide an estimate of T_1 before and after the injection of CA and thus allow an independent estimate of M_0 (see Equation [5.1]). The change in CA concentration was estimated voxel-by-voxel over time via the change in R_1 in this highly saturated experiment. The signal from a spoiled gradient-recalled (SPGR) MRI sequence used in DCE experiment can be written as:

$$S(t) = M_o \frac{1 - e^{-[TR.R_1(t)]}}{1 - \cos(\theta)e^{-[TR.R_1(t)]}} \mathrm{Sin}(\theta) e^{-TE.R_2^*(t)} \quad \textbf{5.1}$$

where, S(t) is the signal intensity at time t, M_o the equilibrium magnetization of the tissue, TR the repetition time, θ the tip angle, TE echo time, and $R_2^*(t)$ is the transverse relaxation rate. Solving equation [5.1] for R_1(t) yields,

$$R_1(t) = \frac{1}{TR} \ln \left[\frac{1 - \left(\frac{S(t) \cos\theta}{M_0 e^{-[TE.R_2^*(t)]} \sin\theta} \right)}{1 - \left(\frac{S(t)}{M_0 e^{-[TE.R_2^*(t)]} \sin\theta} \right)} \right] \quad \textbf{5.2}$$

We note that $R_2^*(t)$ varies with contrast agent concentration in a nonlinear manner[2,5], thus requiring a point-by-point evaluation of its effect on the signal. $R_2^*(t)$ in equation [5.2] was estimated from the log ratio of the two echoes of the DCE-MRI dual-echo spoiled gradient-echo (2GE) sequence[2].

A baseline R_1 was obtained from the one-minute of data taken prior to the injection of CA. Baseline R_1 was subtracted from the post-contrast R_1 as the DCE-MRI study progressed, giving an estimate of the dynamic change in R_1, $\Delta R_1(t)$[2,5,58,60,61]. As noted, $\Delta R_1(t)$ was taken as a measure of the concentration of CA in the tissue after the intravenous administration. Pharmacokinetic parameters were estimated using the SM :

$$C_t(t) = K^{trans} \int_0^t C_p(\tau) e^{-k_{ep}(t-\tau)} d\tau + v_p C_p(t) \quad \textbf{5.3}$$

where $C_p(t)$ and $C_t(t)$ are respectively the concentrations of CA in blood plasma and tissue at time t, K^{trans} is the forward transfer constant of CA between the blood plasma and the EES, k_{ep} is the reflux rate constant from EES to blood plasma, and v_p is the plasma volume fraction. The volume of EES per unit volume of tissue (v_e) is a fraction between 0 and 1; which is calculated as the ratio of K^{trans} to k_{ep}, is referred to herein as

the interstitial volume fraction. The shape of the AIF was taken from a group-averaged radiological input function[82]. A scaling factor was generated from the time trace of activity in the caudate putamen contralateral to the hemisphere with the tumor. Employing the assumption that plasma volume fraction in the normal caudate putamen is 1%, the radiological function was scaled by integrating both the latter half of the radiological trace and the caudate putamen trace and requiring the integral of the radiological trace to be 100 times that of the caudate putamen trace. Using the time trace of ΔR_1 as a measure of concentration, equation [5.3] was then fitted[5,60], yielding the microvascular parameters of the SM or its reduced models.

A voxel-by-voxel data-driven approach to model selection[2,5,58,60,61] was employed to generate model parameter maps, including the selected model. Each model was contested against its nested lower order model, with the winner determined by an F-test. To summarize, (i) model 1: the tissue region with no detectable CA leakage to the EES, i.e, the normal vasculature ($v_p \neq 0$, $K^{trans} = k_{ep} = 0$); (ii) model 2: the tissue region with leakage, but having little or no measurable reflux from EES to the microvasculature ($v_p \neq 0$, $K^{trans} \neq 0$, $k_{ep} = 0$); (iii) model 3: the tissue region with highly leaky vasculature with measurable backflux from EES to the vasculature ($v_p \neq 0$, $K^{trans} \neq 0$, $k_{ep} \neq 0$).

The MRI slice with the largest tumor cross-section was chosen and data analyzed for parameter distribution estimates. The DCE data-driven model 3 region was used to define the tumor ROI excluding extraneous and any unconnected model 3 voxels. Summary estimates of mean, variance, skewness, and kurtosis were evaluated for each of the vascular parameters of the Model 3 tumor region[1,60,61,97]. Model 2 peritumoral regions

were similarly summarized and are reported in the Supplementary Material (Table S3). The choice of ROI and an example of the Patlak plot in the Model 2 region are shown in Figures S11 and S12, respectively in the Supplementary Material.

In contrast to the voxel-by-voxel approach, Flux and V_D were calculated by summing the dynamic $R_1(t)$ estimate in ROIs drawn at the tumor edge (defined by the edge of the Model 3 ROI), the immediately adjacent 1-pixel wide outer ROI, and a larger 'catchment' ROI placed outside the tumor edge as described earlier by Ewing et al.[1]. Logan[56] and Patlak[18] graphical analyses provided estimates of Flux and V_D. Consequently, one estimate of Flux and V_D per study was available, with no parameters to describe their inter-voxel distribution.

With T_1-weighted post contrast and hematoxylin and eosin (H&E) -stained histology images used as references; the Model 3 region was considered the source of truth for delineating the ROI. Histopathology was used to evaluate whether the Model 3 region was representative of the tumor region, and all parametric results were reported for Model 3 regions from all studies. All summed results from Model 3 regions, and Flux and V_D in the rim of the tumor are reported as mean ± SEM.

5.2.9 Histopathology

Following published procedures[37], rats were euthanized by isoflurane overdose, followed by decapitation. Whole brains were quickly removed and placed in a rat brain matrix. With the implantation needle entry as the center, 2 mm thick, coronal slices were cut anterior and posterior to the center to generate frozen and formaldehyde fixed, paraffin embedded (FFPE) tissues. Slices for frozen sections were placed on cork circles and were covered in OCT freezing medium prior to flash freezing in 2-methylbutane

cooled to -40 °C with dry ice. Slices for FFPE were placed in mesh cassettes and immersion fixed in formaldehyde for later paraffin embedding. Five µm thick sections from the FFPE slices were deparaffinized and processed through a graded alcohol series for H&E staining. Adjacent sections were stained for Ki-67 (IR62661-2; Agilent, Santa Clara, CA, USA) with diaminobenzidine (DAB) as the chromogen for visualization. The primary antibody was purchased and used at 'ready to use' dilution. Target retrieval and blocking endogenous enzymes, including peroxidases were performed using reagents supplied with the kit. Primary antibody was applied for 20 minutes followed by a buffer rinse, and Flex horse radish peroxidase applied for 20 minutes followed by a buffer rinse before the application of Flex DAB-substrate chromogen for 10 minutes. The sections were counter stained with Flex hematoxylin for 5 minutes and then given alternate buffer and distilled water rinses. Stained sections were then run down through 95% alcohol 5 minutes, 100% alcohol 5 minutes, and xylene for 5 minutes and coverslipped with mounting medium.

Additional 5 µm thick sections from the frozen slices underwent a 15 min incubation in pH 6.0 citric acid buffer for antigen retrieval, followed by incubation in Rodent Block M (Biocare Medical, Pacheco, CA, USA) for 20 min. They were then incubated with human marker major histocompatibility complex I (MHC; ab52922, Abcam, Cambridge, UK), 1:1000 for 60 min. After primary antibody incubation, slides were incubated for 30 min in Rabbit on Rodent Polymer (Biocare Medical) and for 4 min in Betazoid DAB (Biocare Medical). All the stained slides were scanned in a Leica scanner and analyzed using Aperio ImageScope system (Leica Inc., Deerfield, IL, USA). The images from H&E- and MHC-stained specimens were examined at increasing

magnifications for tumor location, pseudopalisading necrosis, mitotic bodies and infiltration patterns.

5.3 Results

As noted, seven untreated rats (mean age: 125.4 ± 9.09 days) bearing HF3016 and eight (mean age: 142.00 ± 18.46 days) bearing HF3177 PDOX tumors were studied. Tumor location and extent were visualized using T_2 and post-contrast T_1 images, confirmed post-mortem using corresponding H&E and MHC staining, and in their pharmacokinetic maps. Both cell lines led to the formation of space-occupying tumors with an infiltrative component, reminiscent of the patient gliomas from which they originated.

One of the studies (FG136) in the HF3177 studies stood out as an outlier and possibly biased by an underestimation of the true plasma volume in the caudate putamen. Interstitial volume estimates were non-physiological, and in some voxels, non-physical in that they estimated a very large interstitial volume fraction that was in some voxels greater than one. We were unable to positively identify a source of systematic error that led to these estimates; we suspect that an underestimate of the true plasma volume is at the root of this problem, but despite a very thorough examination of the circumstance of the experiment (see Supplementary Material), do not have conclusive proof for this hypothesis. The data point is included in the graphs of parametric estimates, but not in the analysis for correlations and/or means, etc.

Table 5.1 summarizes the estimated microvascular parameters for each tumor model, sans the data of FG136 (Please see Supplementary Material for a detailed consideration of the sources of systematic error in this study). The MRI-generated

parameter and model maps and corresponding histology images showed good spatial agreement in tumor extent in all the animals. All exhibited BBB breakdown in post-contrast T_1-weighted images (Figure 5.1). Examples of pre- and post-contrast T_1, and ADC map image are shown in Figure (5.1) (Figure 1A,1B, 1C) along with their respective microvascular parameters (v_p, K^{trans}, v_e) model maps (Figure 1D, 1E, 1F), the model selection map (Figure 1G), and MHC-stained brain section (Figure 1H). Two HF3016 and one HF3177 PDOX rats were scanned at multiple times to investigate the temporal development of microvascular parameters. Data from these longitudinal MRI studies are shown in Supplementary Material (Figure S1) to demonstrate the temporal changes in glioma vascular kinetics of the space-occupying tumor mass.

A Logan plot estimate of distribution volume in the two models at the mostly normal outer rims of the tumors and their relationship with exudate flux to the peritumoral tissue were performed. In agreement with previous studies in U251N[1] and 9L models (unpublished data), the fluxes estimated were found to be strongly correlated with tumor distribution volumes at the rim of the tumor (R^2=0.84 for HF3016 and R^2=0.91 for HF3177) as shown in Figure 5.2 (A). Compression of the mostly normal tissue rim encircling the glioma periphery was observed in HF3016 (slope <1.0) by comparing V_D estimates from the outer mostly normal rim with that of the inner, mostly tumorous adjacent voxels, Figure 5.2 (B). However, the mean $V_D \pm$ SEM in the entire model 3 region of HF3016 tumors, $28.50 \times 10^{-2} \pm 5.94 \times 10^{-2}$, did not differ significantly from that of HF3177, $30.70 \times 10^{-2} \pm 2.91 \times 10^{-2}$ (p=0.7, t-test).

Parameter estimates (v_p, K^{trans}, v_e) in Model 3 regions were normally distributed with a small positive skewness. The mean values were close to the median (<4%

difference), the skewness and kurtosis were both near-normal. Parameter estimates from the two PDOX models studied in this work were compared with those of U251N and 9L cerebral tumors in earlier studies[61,97]. Estimates of K^{trans} and v_p were comparable with those of the U251N and 9L tumor models but v_e in both PDOX models were significantly higher than the estimate in U251N studies ($p < 0.002$, unpaired t-test). Moreover, v_e for PDOX HF3177 studies was significantly higher than the estimate for 9L tumor model ($p < 0.003$, unpaired t-test). The PDOX HF3016 v_e estimate was larger than that of 9L studies but the difference was not statistically significant. As to V_D, the peritumoral distribution space in the PDOX tumors, the mean estimated V_D ($14.4 \times 10^{-2} \pm 3.37 \times 10^{-2}$ and $15.4 \times 10^{-2} \pm 2.79 \times 10^{-2}$ for HF3016 and HF3177, respectively) were significantly greater than the estimates for U251N tumor model ($p<0.03$). The mean V_D estimate from HF3177 was also significantly greater than that of 9L tumor model ($p<0.04$) whereas the V_D estimate from HF3016 was larger than in the 9L model, but not statistically significant.

The larger estimates for both V_D and v_e in PDOX lines points to a highly edematous tumor line, and a subsequently different physical state of these models compared to standard models in current use. The higher V_D for both the cell lines was clearly reflected by similarly elevated values of v_e in the body of the PDOX tumors, since the two measures are produced by independent methods but report on similar tissue properties.

A plot of the distribution volume in the tumor rim versus the mostly normal outer rim (Figure 5.2 (B)) showed a strong correlation between inner edge distribution volume (tumor tissue) and the outer edge distribution volume (mainly normal tissue) with a

regression slope of 0.62 for HF3016 and significantly higher regression slope (> 1) for HF3177. The relative compression of tissue in the HF3016 tumors was expected from previous studies[1]; the lack of compression in the HF3177 tumors was not expected.

The estimated ADC values were (2.16×10^{-3}) ±(8.12×10^{-5}) and (2.13×10^{-3}) ±(5.88×10^{-5}) mm^2 sec^{-1} for HF3016 and HF3177 respectively. ADC and v_e showed a significant positive correlation for HF3016 tumor model but the degree of correlation was moderate (R^2=0.53, Figure S4 (E1), Supplementary Material). Contrarywise, our data did not reveal a trend between those two parameters for the HF3177 model (Figure S4 (E2), Supplementary Material). Estimates of TBF were expressed as fractions of contralateral normal brain blood flow. The mean TBFs were 0.67 ±0.14 and 0.58 ±0.17 for HF3016 and HF3177, respectively, demonstrating decreased blood flow in the tumor.

Further examination of H&E-stained specimens recapitulated the major histological features related to clinical assessment of high-grade glioma pathology (Figure 5.3). They included increased cell density compared to normal brain, mitotic bodies, irregular blood vessels with vascular stasis, and regions with pseudopalisading necrosis. Typical histological assessment of HF3016 tumors showed hypercellular infiltrative tumors with nuclear atypia and increased mitotic activity (Figure 5.4 A). Some of the tumors exhibited necrosis, some with pseudopalisading necrosis (Figure 5.4C). MHC immunohistochemistry highlighted the infiltrative nature of the tumor cells showing their infiltration to the adjacent brain parenchyma, including the corpus callosum, as well as subpial and perivascular tumor cell aggregation (Figure 5.4 B). The Ki-67 proliferation index was elevated and approximately ranged from 20 to 80% in a number of animals studied (Figure 5.4 D). On the other hand, the histological assessment

of HF3177 tumors demonstrated hypercellularity with spindled architecture with nuclear atypia and increased mitotic activity (Figure 5.4 E,F). The tumors appeared compact with focal infiltration into the adjacent brain parenchyma (Figure 5.4 E,F). Foci of early necrosis were noted in some of the animals studied (Figure 5.4 G). The Ki-67 proliferation index was elevated and approximately ranged from 20 to 30% in the set of animals studied (Figure 5.4 H). Along with these typical histological GBM signatures in the space-occupying, contrast enhancing component, both HF3016 and HF3177 tumors also showed an MRI-invisible, infiltrative component extending beyond the central tumor mass. The patterns of infiltration were confirmed by concurrent MHC-stained specimens (Figure 5.4 B) (Supplementary Material, Figure S2, S3). Tumor-normal tissue profile of HF3016 MHC images showed a significant amount of infiltrating tumor cells beyond the peritumoral area indicating a high degree of infiltration(Supplementary Material, Figure S3). Compared to that, HF3177 showed a higher number of tumor cells in the main tumor mass with fewer infiltrative cells beyond it. In both models, intra-tumoral profile sections also reflected regions of high cellularity and pseudopalisading necrosis (Figure S3).

5.4 Discussion

In this work, we measured several microvascular and tumor microenvironment (TME) properties in a unique combination of two PDOX models of human GBM. The models were generated from neurospheres derived from biopsy samples of a primary GBM (HF3016) and its recurrent version (HF3177). To our knowledge, reports from preclinical characterization of such paired tumors from the same patient are scarce. Salient features of these models, as prepared with the co-injection of Matrigel, included

the presence of a space-occupying, contrast-enhancing mass with MRI-invisible infiltration.

The microvascular parameter estimates reported in this work are useful in establishing baseline values of tissue parameters in PDOX tumors. One of the more striking observations is the elevated interstitial volume fraction and distribution volume in the entire tumor mass. The tumor distribution volume at the peritumoral tissue and its strong correlation with exudate flux at the boundary confirms an earlier finding in U251N tumors[1], and in 9L rat gliosarcoma model (unpublished data); these also have shown a strong positive correlation between Flux and the V_D estimates at the edge of the tumor. However, there are markedly higher distribution volumes in these PDOX models than in previously studied U251N human[13,61] and 9L rat glioma[97] tumors, indicating that PDOX gliomas are relatively low density tumors with necrotic cores, as evident in post contrast T_1 weighted and H&E histopathology images. Analyses in earlier studies[37,190,191] have highlighted pseudopalisading necrosis as the salient feature of human glioblastomas, and our observation is in line with that finding. Such regions represent hypoxic tumor core from which the cells are receding away. These data parallel the overall TBF values that were lower than normal brain regions.

We note here that the PDOX cells were co-implanted with Matrigel-low growth factors because a previous study showed that this approach helps formation of a tumor with contrast-enhancement[37]. Relevant to this observation are data from clinical reports wherein visualization of contrast-enhancing component of both newly diagnosed and recurrent glioma are necessary for resection and the MRI-invisible infiltrative component is then subjected to chemoradiation in efforts to delay or prevent further recurrence[192,193].

Thus, an animal model that reproduces both these radiological GBM features is useful for preclinical drug testing. Moreover, an animal GBM model with an embedded tumor lends itself to tumor resection techniques in order to reproduce the clinical approach. Mouse GBM models are prevalent due to the ability to quickly generate specific knock-out and knock-in models and for the ease of high throughput studies. However, there are some concerns that the small mouse brain results in a lack of tumor necrotic features and also fails to show microvascular abnormalities[34]. Therefore, after the initial testing of a putative pharmacological treatment using a high throughput mouse model to target a specific pathway, the next level of testing could be done using a rat glioma model with radiological fidelity to the human images to increase the translational applicability of the data.

Overall DCE-MRI properties of the two PDOX models were comparable, albeit with some differences. HF3016, derived from primary glioma, exhibited a slightly smaller K^{trans}, v_e and V_D values than HF3177, the recurrent glioma. These factors led us to a comparison of the two PDOX models with two other rat models of glioma, viz., U251N and 9L. Of note, the human-derived U251N model is considered as representative of primary glioblastoma and the syngeneic 9L model to represent recurrent GBM with gliosarcoma-like features[34,170].

The HF3016 tumor line displayed a regression slope between the inner and outer rim distribution volumes that was less than 1, as expected from previous studies[1] and indicative of compression of peritumoral, mostly normal tissue. Contrariwise, the HF3177 tumor line did not show this compression. This may be due to a more edematous environment in the mesenchymal-type recurrent glioma. Evidence for this interpretation

lies in the significantly larger distribution volume in both the HF3177 tumor body, and in its rim. A comparison of T_2-values in the catchment ROI around the tumors showed a highly significant increase in T_2, indicative again of a greater water load in the surrounding tissue. A comparison of T_2 estimates across the glioma tumor models showed that mean T_2 estimates in PDOX cell lines (61.70 ± 1.07 ms and 66.81 ± 1.46 ms, respectively, for HF3016 and HF3177) were significantly greater than that of 9L glioma (56.40 ± 0.81 ms), ($p < 0.002$). Similarly, the mean T_2 estimate for HF3177 was significantly greater than that of U251 glioma (61.0 ± 0.71) ms, ($p<0.0006$); mean T_2 estimate from HF3016 was greater than the U251N but not statistically significant. Computational modelling of glioma tumors by Rey et. al[84,120] based on DCE-MRI derived parameters explained several biphasic properties of high-grade gliomas, primarily the highly elevated tumor interstitial fluid pressure, compressive solid stress at the tumor rim, tissue porosity etc., and their consequence on various vascular parameters of interest. They have shown that there had been significant interstitial fluid flow and flux at the periphery of the tumor from the prominent interplay of those physical forces in tumor microenvironment. The high fluid content balances the compressive forces due to tumor growth and, despite the high number of tumor cells, produces an increase in interstitial volume.

The scale of measurement in this paper ranges from the 2 mm slice thickness of the MRI Dynamic studies to the micron scale of the histology slides. The in-slice resolution is ~250 μm, and thus the boundary of the tumor as described by model selection has at best that resolution, whereas the histological slides were 5 μm thick and had in-slice resolution on the order of μm. Nevertheless, the macro-characteristics of the

tissue, as described by DCE-MRI analysis (leakiness, blood flow, interstitial space), matched well with the micro-characteristics described in histology (atypical vasculature, pseudopalisading necrosis). This supports the inference that DCE-MRI studies with data-driven analyses can provide a useful summary of the local physical state of a realistic animal model of an embedded cerebral glioma.

It is interesting to note that 9L model showed larger v_e and V_D values[97] in comparison to U251N[61], similar to the comparison of HF3177 to HF3016. Implying a comparatively lower tumor cell density in both recurrent GBM models, 9L as well as in HF3177, tumor cell density has been shown to be inversely proportional to V_D [60]. These comparisons with established GBM models help highlight that PDOX models can recapitulate the salient radiological features of rat GBM models from immortalized cell lines. The need for reliable and comprehensive models that recapitulate features of human GBM for conducting impactful pre-clinical trials is critical[31]. With their genetic fidelity to patient GBM and formation of a space occupying, MRI-visible tumor mass with infiltration, rat PDOX models derived with co-injection of Matrigel provide a robust GBM animal model to study tumor pathophysiology and responses to putative therapies[37]. Data sets from other similar naive (i.e., unperturbed by any treatment) PDOX glioma models can be used as the baseline for further longitudinal studies on signatures of response to therapy and understanding factors that influence cancer cell growth and invasion.

5.5 Study limitations

New drug regulations during the course of study led to non-availability of Magnevist and we had to switch to using Dotarem for some DCE-MRI studies. Pilot

studies indicated less than 10% variation in DCE-MRI vascular kinetic parameter estimations between the two contrast agents. Therefore, data from the two agents have been pooled where applicable. All studies were done using female rats. Previous studies employing immortalized cell lines such U251N and 9L in both female and male rats have shown no significant sex-dependent differences in glioma vascular kinetics and their responses to radiation[194]. However, whether or not such responses are sex-dependent in PDOX models needs to be investigated in future studies.

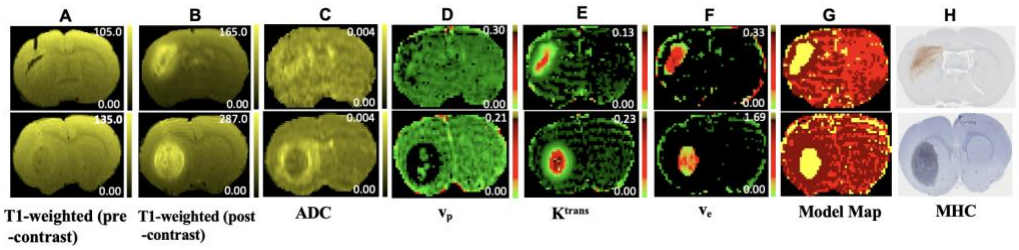

Figure 5.1: Representative images showing tumor status and the associated vascular parameter maps in two different animals derived from DCE-MRI data analysis using a model selection paradigm demonstrating various imaging biomarkers. Top row, HF3016; bottom row, HF3177. Rows from left to right: T_1-weighted pre-contrast (A) and post-contrast (B) image acquired using a RARE sequence, (C) ADC map, (D) v_p, (E) K^{trans}, (F) v_e, (G) model selection maps, and (H) MHC-stained brain section. Note the fidelity of imaging data with histology regarding tumor location and extent. Value ranges for each parameter are shown in the color bar to the right of each map. For the model selection map, yellow is Model 3 acceptance, dark red is Model 2 acceptance, red is Model1 acceptance. The goodness of fit for derived model parameters in Model 3 region are provided in Supplementary Material table S2.

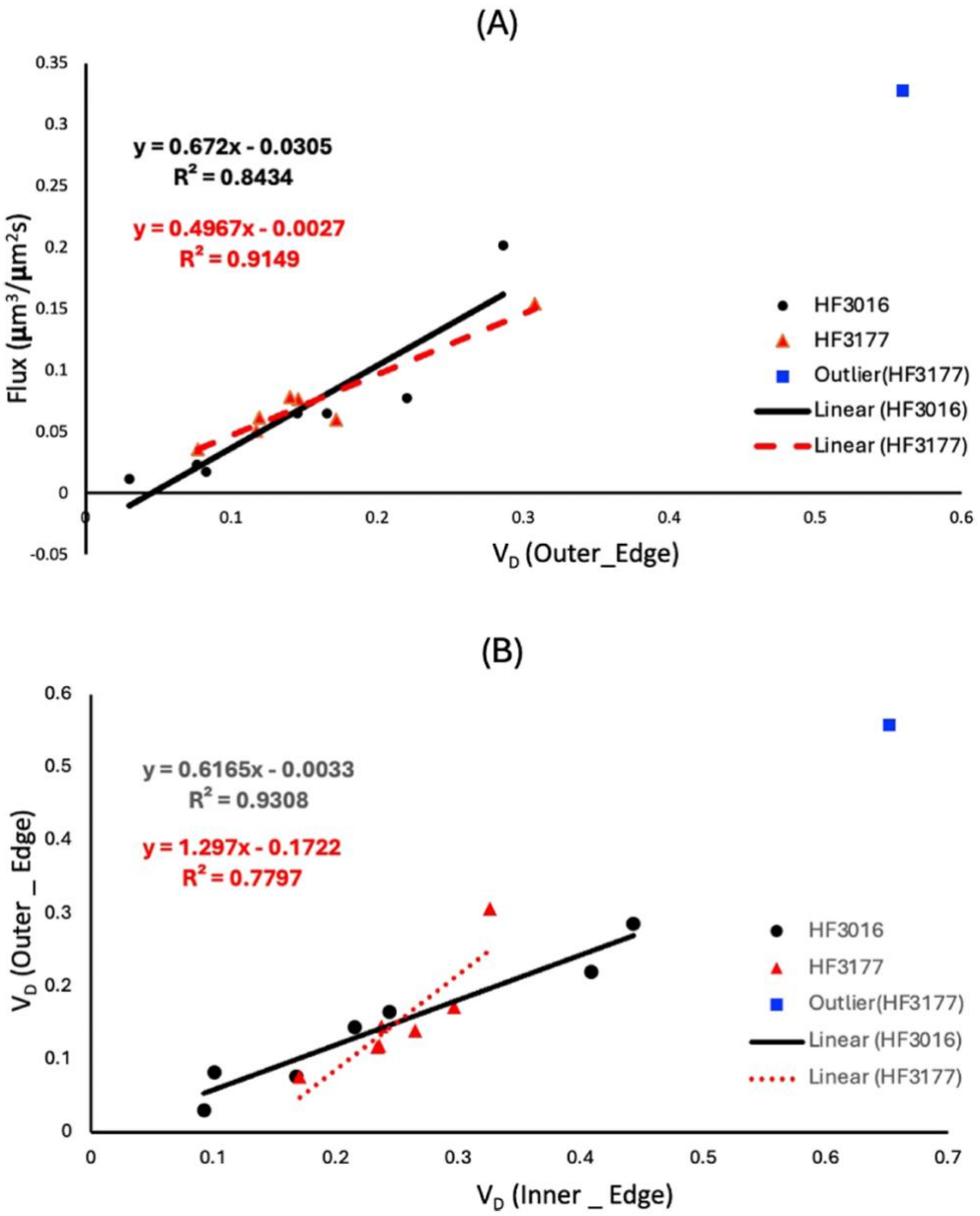

Figure 5.2: Panel (A): Flux vs distribution volume at the outer rim of the tumor for HF3016 and HF3177 demonstrating that in both models, as in other cerebral models, Flux and V_D are highly correlated (R^2= 0.84 for HF3016 and R^2 = 0.91 for HF3177).
Panel (B): Plots of inner edge (tumor) versus outer edge (mainly normal tissue) distribution volume data. A regression slope of 0.62 for HF3016 tumor model indicates that the outer, mostly normal rim of tissue is compressed relative to the inner tumorous tissue. However, a significantly higher regression slope (> 1) resulted for HF3177.

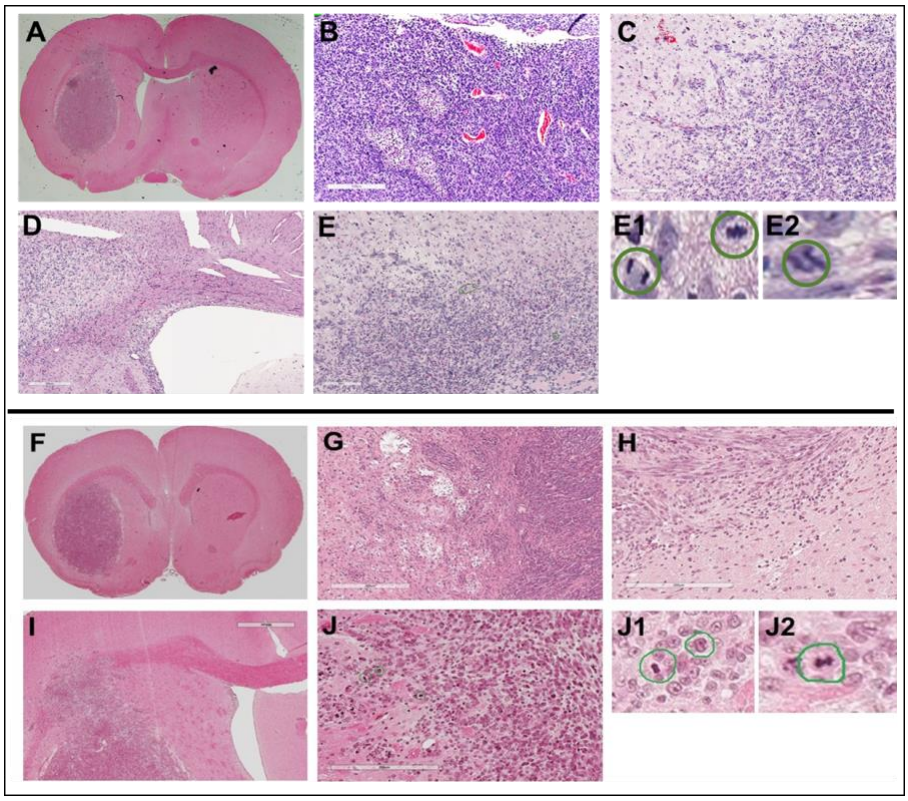

Figure 5.3**:** Representative hematoxylin and eosin(H&E)-stained brain sections showing tumor tissue at different magnifications to highlight their histological details. Top panel, A-E2, are from HF3016, and the bottom panel, F-J2, are from HF3177. In both, A and F are the complete sagittal cross section of the brain showing the location and extent of the embedded glioma. B, and G, show regions with pseudopalisading necrosis, C and H show irregular vasculature with stasis and tumor-brain interphase with infiltrative cells. D and I show infiltration across corpus callosum in these models. E and J exhibit mitotic bodies (green circles). The green circles around mitotic bodies in E and J are shown enlarged in E1, E2 and J1, J2.

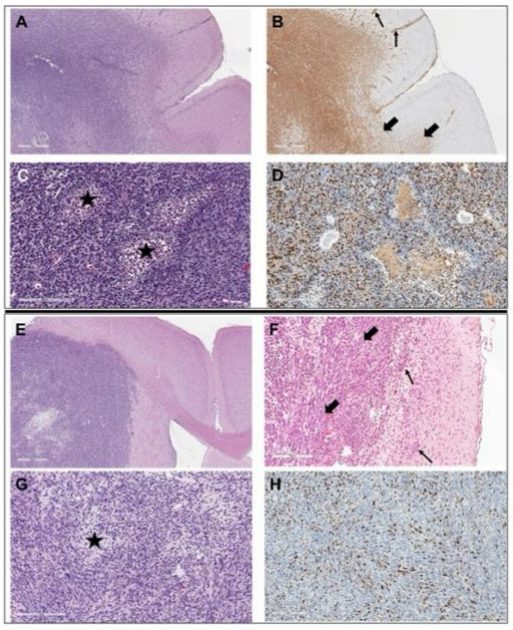

Figure 5.4: Comparative histopathological analysis of H&E, MHC and Ki-67 staining patterns in the two models. Top four panels A to D are from HF3016, and the bottom four panels E to H are from HF3177. HF3016 animals show hypercellular infiltrative tumors (A; H&E). The infiltrative nature of the tumor is highlighted as it crosses the corpus callosum (block arrows in B; MHC) and demonstrates subpial and perivascular aggregation (thin arrows in B). Pseudopalisading necrosis (asterisks), as demonstrated in this case, is seen in some of the animals (C; H&E). The Ki-67 proliferation index is high, approximately 40% (D; Ki-67). HF3177 animals show hypercellular tumors that appear compact (E; H&E). The tumor displays spindling architecture (block arrows, F: H&E) and focal infiltration (thin arrows in F). Focal early necrosis (asterisk) is appreciated in some animals (G; H&E). The Ki-67 proliferation index is high, approximately 25% (H; Ki-67).

Cell line	Parameter (unit)	Mean ($x10^{-2}$)	Variance	Skewness ($x10^{-1}$)	Kurtosis ($x10^{-1}$)
HF3016	v_p [mL/mL]	1.17 (±0.33)	3.50 (±1.51) $x10^{-4}$	10.40 (±4.02)	30.40 (±13.90)
	K^{trans} [mL/min-mL]	4.13 (±0.52)	6.80 (±1.76) $x10^{-4}$	8.75 (±1.80)	8.23 (±5.82)
	k_{ep} [mL/min-mL]	18.59 (±2.18)	5.27 (±1.62) $x10^{-3}$	-2.59 (±4.23)	19.18 (±16.31)
	v_e [min^{-1}/ min^{-1}]	26.60 (±5.84)	4.23 (±2.57) x 10^{-2}	8.34 (±3.26)	21.40 (±11.00)
	V_D [mL/mL]	28.50 (±5.94)			
	ADC [mm^2/sec]	2.16 $x10^{-1}$ (±8.12 x 10^{-3})	9.20 (±2.91) x 10^{-8}	-0.10 (±2.69)	10.80 (±8.02)
	TBF$\frac{[mL/gm-min]}{[mL/gm-min]}$	67.10 (±13.90)	7.03 (±1.21) x 10^{-1}	23.80 (±16.20)	66.50 (±55.10)
HF3177	v_p [mL/mL]	1.16 (±0.37)	1.78 (±0.95) x 10^{-4}	5.00 (±1.23)	8.85 (±3.87)
	K^{trans} [mL/min-mL]	4.06 (±0.64)	2.90 (±1.42) x 10^{-4}	3.54 (±1.80)	0.16 (±3.19)
	k_{ep} [mL/min-mL]	11.22 (±1.22)	4.13 (±1.35) $x10^{-3}$	-1.60 (±1.13)	2.24 (±2.01)
	v_e [min^{-1}/ min^{-1}]	33.40 (±2.93)	1.44 (±0.32) x 10^{-2}	14.00 (±3.46)	43.20 (±13.4)
	V_D [mL/mL]	30.70 (±2.91)			
	ADC [mm^2/sec]	2.13 $x10^{-1}$ (±5.88 x 10^{-3})	15.0 (±2.45) x 10^{-8}	4.24 (±4.17)	37.40 (±9.04)
	TBF $\frac{[mL/gm-min]}{[mL/gm-min]}$	57.90 (±16.80)	4.62 (±1.14) x 10^{-1}	-5.45 (±8.11)	9.11 (±8.36)

Table 5.1: Summary statistics of DCE-MRI microvascular parameters v_p, K^{trans}, k_{ep}, v_e and V_D in the Model 3 region of interest, and respective ADC and TBF values. TBF values are shown relative percents of contralateral corresponding normal brain values. Variance, Skewness, and Kurtosis are reported to reflect the distribution of parameter values per voxel in the ROI. Each value reported is the mean ± SEM, with K^{trans} and k_{ep} in (mL/mL-min) and the rest unitless. Top panel for HF3016 and bottom panel for HF3177. V_D is estimated from the summed $R_1(t)$ values across the ROI. Hence, no distribution parameters are available.

CHAPTER 6

RECEIVER COIL AMPLITUDE DRIFT DURING DCE-MRI SIGNAL ACQUISITION AT 7T

This chapter presents the analysis of systematic bias resulted from the heating of active and passive components of small animal imaging 7T magnet receiver coil used in the Henry Ford Health small animal imaging laboratory. This chapter has been submitted for publication in the journal Magnetic Resonance in Medicine and is under review.

6.1 Introduction

In small animal MRI studies (rats and mice), receiver coils with active decoupling (AD) are required in order to protect the amplifier gain, but in sequences that rely on the assumption of a stable receiver[21,136] AD heating may introduce bias in data acquisition. Rapidly applied radiofrequency (RF) fields and long scan times can lead to significant heating effects in a receiver coil due to heating in AD circuits, with a consequent reduction in Q. This can result in a temporal drift in the efficiency of signal acquistion[19-21,135,138].

Dynamic contrast-enhanced MRI for estimating tissue perfusion and other microvascular parameters is a high duty-cycle sequence that typically uses a multislice or 3D spoiled gradient-recalled echo (SPGRE) sequence[2,6,60,61] for rapid acquisition of T_1-weighted images after contrast agent injection. DCE-MRI, depending as it does on saturated T_1-weighted images is a sequence that is inherently a high-duty cycle on the RF transmit side. While there have been reports of duty-cycle related transmit coil heating of

the MRI experiment[20], and in gradient supplies and coils[20,195], there is a dearth of reports of heating on the receiver side[19,196].

In a cohort of studies in a rat cerebral tumor model, we found an unexpectedly large variability in estimates of the forward vascular volumetric transfer constant K^{trans}, an important parameter in pharmacokinetic modelling. DCE-MRI studies using a Bruker BioSpin 4-channel phased-array coil, compared to a similar 2-channel coil from the same manufacturer but with different AD and a less demanding duty cycle, resulted in larger test-retest variances, even though signal-to-noise appeared comparable between the two coils and sequences. Consequently, a review of our DCE data analysis was initiated.

At Henry Ford Health (HFH) receiver signal drift in a DCE-MRI study was examined in a phantom, and in animal studies. Two vendor-supplied pre-tuned and -matched coils from Bruker BioSpin were studied, one a true 4 channel array (Coil 1), and, and the other a 2-channel array (Coil 2) with an integrated combiner. Coil geometries were similar but differed in AD details. In Coil 1, heating effects significantly changed the receiver signal amplitude, producing both a short-term (tens of seconds) and long-term (ten minutes) decrease in signal amplitude. This effect was diminished in Coil 2. Cooling Coil 1 removed the drift. Both Coil 1 and 2 are commonly used in small-animal MRI systems. Sequence details were held constant across studies with an intent to develop an approach that would identify a correction for systematic biases in previously acquired data sets.

Follow-up studies were conducted by Bruker BioSpin staff with a shortened protocol and a focus on varying experimental conditions (tip-angle, pulse duration, slice number) so that a hardware source of systematic error could be identified and corrected.

This was a forward-looking investigation of measures that might be taken to minimize future sources of bias. The results of both efforts are reported herein.

6.2 Materials and Methods

6.2.1 Small animal magnetic resonance system

The HFH small animal imaging laboratory uses a Varian/Magnex (Santa Clara, California) 7T 20 cm bore magnet for rat or mouse imaging with a Bruker console running Paravision 6.0.1 software. Gradient maximum strengths and rise times are 250 mT/m and 120 ms respectively. Transmit and receive coils are a Bruker Quadrature Birdcage and Coil 1, a 4-channel phased-array rat head surface coil receiver with active components (Bruker BioSpin 2 x 2 array, Model No 1P T11483V3, Serial No S 0104). As noted, Coil 2, a backup coil Bruker BioSpin Model No 1P T20010V3, Serial No S 0041, with similar geometry was available. Coil 1 was generally used rather than Coil 2, save when Coil 1 was sent back for repair.

The coils are placed as the top half of a rat head-holder, with the vertical plane of the coil at right angles to the horizontal. Active elements are grouped together at their tops. AD is on only when the transmit coil is pulsing. Both coils use a decoupling circuit with the "pole insertion" method (see Mispelter, 9.3.2)[197] and draw a total current of 100mA when AD is on. Differences are Coil 1: A true 4-channel array with 4 preamplifiers, 4 elements each with the above-mentioned AD scheme and a resistor in series with the PIN diode to stabilize the bias current. Coil 2: a 2-channel array with two preamplifiers and an integrated combiner, two elements each with the above-mentioned AD scheme and no resistor in series with the PIN diode.

6.2.2 DCE-MRI study protocol

The HFH MRI imaging protocol uses Coil 1 in rats for acquiring T_1- and T_2-weighted high resolution images, cerebral blood flow using arterial spin labeling with a segmented echo planar acquisition, diffusion weighted images using pulsed gradient spin-echo with b-values up to 1792 s/mm^2, two consecutive LL sequences before and after the administration of CA, and six gradient-echo sequences with varying repetition times in order to independently estimate tip angle, and proton density. The DCE-MRI sequence used is a dual-echo spoiled gradient-echo sequence with 400 acquisitions at 1.5 s intervals, 128 x 64 matrix, three 1.9 mm slices with 0.1 mm gap, FA = 18^o, NE=2, NA=1, TE=2.0 and 4.0 ms, TR=24.2 ms, spectral width=150 kHz. Note that previous studies using Coil 2 that had little apparent drift acquired slice packs at 4 s intervals using a 27-degree tip angle. In both previous and present studies, the DCE-MRI sequence was initiated with one minute of baseline scan prior to CA injection, followed by CA injection via rat's tail vein. The DCE-MRI total run time is ~ 10 min. All MRI image sets are acquired with a 32 x 32 mm field of view. Details of the previous DCE-MRI protocol, MR sequences, and summary results can be found in earlier publications[1,2,58,97].

6.2.3 Bruker BioSpin Studies

In follow-up experiments at Bruker facilities, the HFH studies were first confirmed by Dr. Saausan Madi at the U.S. Bruker facility in Billerica, MA. Further experiments were performed at the central Bruker BioSpin facility in Ettlingen, Germany in a Biospec 70/30 (7T) running ParaVision 6.0.1 and using a receive coil identical to that of HFH. The basic sequence used was a single-echo spoiled gradient-echo sequence with 60 acquisitions at 2.4 s intervals, 96x96 matrix, one 1 mm slice, FA = 15^o,

TR/TE=25/12.5 ms, FOV = 60 mm. In a sweep of sequence parameters, pulse width, flip angle, and number of slices were varied to characterize the source of systematic variation in signal amplitude.

6.2.4 Agar phantom preparation

Gel phantom with different Agar and copper sulfate ($CuSO_4$) concentrations were prepared at HFH laboratory following established procedures[198,199]. The idea of using different agar concentrations was to check the phantom's stability at room temperature. For 2% agar, 1 gm of agar powder was dissolved in 50 ml of normal water. Similarly, for 4% agar, 2 gm of agar powder was doped with 10 mg of $CuSO_4$ in 50 ml of normal water. The solution was kept on the stirring hot plate and operated at moderate temperature until the solution turned transparent that ensured the solutes properly dissolved in water. After that, the solution was poured into cylindrical plastic tubes and let intact to cool it down to room temperature. Three different $CuSO_4$ concentrations in 50 ml of water (0.025, 0.05, and 0.1%) were doped with each type of agar concentration so that it would provide different estimates of T_1. The phantom with T_1 value approximately close to the T_1 estimate in DCE experiment in rats (~ 700 ms) would be chosen for MRI scan and analysis. A summary of agar phantom preparation is summarized in Figure 6.1.

6.2.5 Surface coil ice-drape design

To investigate the thermal drift issue, the phantom was scanned under thermal equilibrium using a custom-made ice mold conforming to the surface coil. The mold was wrapped in thin plastic to prevent moisture from reaching the coil electronics. First, a negative mold of the coil was formed in Plaster of Paris. After hardening, a positive mold was created and draped with ice in a refrigerator. The resulting ice mold was placed on

the coil for several minutes before scanning to ensure equilibrium, after which imaging commenced.

6.2.6 DCE-MRI data acquisition in a phantom

A 4% agar phantom that produced an estimate of T_1 close to the median T_1 in a DCE experiment in a rat cerebral tumor(~ 700 ms) was chosen for the analysis. The phantom was scanned using Coil 1 employing the high duty-cycle DCE sequence (1.55s slice-pack acquisition, 18-degree tip-angle). Afterward, the phantom was removed from the magnet and the DCE scan repeated in the same set-up to produce an image of pure noise. In another experiment, Coil 1 was first brought to thermal equilibrium by cooling the coil with an ice pack and the DCE scan then repeated. Phantom scans were also repeated under identical conditions using Coil 2, but with no ice draping.

6.2.7 DCE-MRI data acquisition in rats with an implanted 9L cerebral tumor

All animal studies were done under an IACUC-approved protocol (#1604). Ten-to-twelve weeks old Fisher rats (Charles River Laboratories, Wilmington, MA) were orthotopically implanted with 9L cells following published procedures[97,194]. Animals were anesthetized with isoflurane (3% for induction, 1–2% for maintenance, balance N_2O:O_2 = 2:1). A 1-cm incision was made 2 mm to the right of the midline, and the skull was exposed. A burr hole was drilled 3.5 mm to the right of the bregma, taking care not to penetrate the dura mater. A 10 μL Hamilton syringe with a 26-gauge needle containing 2×10^4 9L tumor cells in 10 μL of phosphate buffered saline (Life Technologies, Carlsbad, CA), was lowered to a depth of 3.0 mm and then raised back to a depth of 2.5 mm to create a pocket. Cancer cells were injected at a rate of 0.5 μL/10 s.

For the MRI study, between 12 and 14 days after tumor induction, each animal was anesthetized using isoflurane and allowed to spontaneously respire. A tail vein was cannulated for magnetic resonance contrast agent administration. Body temperature was maintained at 37° C with warm air and monitored via an intra-rectal type T thermocouple. Identical procedures were carried out in the two MRI studies conducted 24 h apart (test-retest) for each animal.

6.2.8 Modeling drift data

As shall be demonstrated, visually significant signal drift occurred across the entire time of the experiment, both with and without the phantom. The following heuristic equation with at most three parameters yielded a visually acceptable fit to the acquired DCE signal regardless of signal amplitude:

$$S(t_i) = a + b \,.\ln\,(t_i\ + c) \qquad \textbf{6.1}$$

where, $S(t_i)$ represents the measured signal intensity, t_i the scan time, and a, b, and c are the fitting parameters.

The parameter 'a' might be thought of as a 0-time-intercept if c is near 1. Parameter 'b' is related to the slope of the logarithmic portion and dependent on the strength of the drift; b < 0 indicates signal decay over time. Parameter 'c' accounts for the time shift indicating the onset of thermal drift, if present. In phantom and animal, or in the noise studies (with no phantom in place), an estimate of the signal amplitude of the i^{th} acquisition $S(i) = a + b \cdot \ln(i + c)$ was employed, where the integer i refers to the i^{th} slice pack acquisition $(1 \leq i \leq N)$, with N = 400 in the usual HFH experiment, and in lesser total acquisitions in other studies designed to study the systematic behavior of signal drift.

Identifying receiver signal amplitude drift in a phantom across the time of the DCE-MRI experiment is fairly straightforward; one can expect the signal to be constant, and a deviation from the constant identifies signal drift. The case is more difficult in the DCE-MRI experiment in animals because of the introduction of contrast agent to the tissue and the subsequent change in signal amplitude across time due to that perturbation. Thermal contact of surface coil with the animal, forced-air heating to maintain animal temperature during the scan etc. also might influence coil sensitivity.

6.2.9 Pharmacokinetics

Changes in receiver sensitivity across time in the DCE-MRI experiment can propagate into significant systematic errors in the DCE-MRI experiment. In our studies, DCE-MRI utilizes PK modeling of a bolus of CA in embedded cerebral tumors exhibiting BBB breakdown in rats[1,2,5,61].

DCE-MRI analysis assumes that the temporal change in the longitudinal relaxation rate R_1 ($R_1 = \frac{1}{T_1}$) is proportional to the CA concentration in the tissue[2,5,60,189]. In our practice, a baseline R_1 is obtained from the one-minute of data taken prior to the injection of CA. The baseline R_1 is then subtracted from the post-contrast R_1 as the DCE-MRI study progresses, giving a voxel-by-voxel estimate of dynamic change in CA concentration which is then utilized to generate model parameter maps using data driven model selection[2,5,58,60].

CA concentration in tissue over time is modeled using compartmental exchange theory[17,18]. The highest order model applied to DCE-MRI data in brain tumors is usually that of the Standard Model[15],

$$C_t(t) = K^{trans} \int_0^t C_p(\tau) e^{-k_{ep}(t-\tau)} d\tau + v_p C_p(t) \qquad \textbf{6.2}$$

where $C_t(t)$ is the concentration of CA in the tissue, $C_p(t)$ is the concentration of CA in the plasma, t is time, and the model parameters v_p, K^{trans}, and k_{ep} are plasma volume fraction, blood-to-tissue forward volumetric transfer constant, and reflux constant from EES to blood plasma. In this approach, it is assumed that the time trace of arterial CA concentration, i.e. the AIF, can be measured, that the selected model can be applied to the data on a voxel-by-voxel basis, and that CA exits and returns to the vasculature of its voxel.

The overall fit of the model to the data is generally excellent, with R^2 typically > 0.95 (Supplementary Material Figure S8 and ref[5]). However, we have found cases using Coil 1 where the parametric estimates, even with an excellent fit, can be non-physiological, and in some voxels, non-physical, in that v_e is estimated to be larger than 1(Figure reference same as the one earlier in this paragraph). This points to a systematic error in estimating PK parameters. The source of this systematic error appears to be in calibrating the estimate of the amplitude of the arterial input function.

In our practice, a region of interest in the normal caudate putamen is defined where it is known that no extravasation of CA occurs and the plasma volume is approximately 1% of the tissue volume[83]. Because it is seldom possible at 7T to obtain a complete time trace of R_1, a group-averaged radiological input function is used, and scaled by the integral of the latter half of the time trace of $\Delta R_1(t)$ in the caudate putamen It is assumed that the relaxivity of CA in this scenario is that of tissue[2,5], and that the scaling factor between $\Delta R_1(t)$ and CA concentration in both blood and tissue is the same.

In this case, $C_t(t) = a\Delta R_{1t}(t)$ and $C_p(t) = b\Delta R_{1p}(t)$, where a = b. Suppose a and b are not equal. Let $\kappa = b/a$; equation 6.2 is then stated as

$$\Delta R_{1t}(t) = \kappa\left[K^{trans}\int_0^t \Delta R_{1p}(\tau)e^{-k_{ep}(t-\tau)}d\tau + v_p\Delta R_{1p}\right] \qquad \textbf{6.3}$$

A scaling error ($\kappa \neq 1.0$) in the estimate of the AIF affects the estimate of K^{trans} and v_p linearly. Because $\Delta R_{1t}(t)$ is a measured quantity, an error by a factor of 2 (e.g.) in κ should cause a compensating inverse error by a factor of 2 in both K^{trans} and v_p.

6.3 Results

Shown in Figure 6.2 are the time trace of the average signal (top panel: Left: Phantom cross-section and ROI, Right, Coil 1, and bottom panel Coil 2) taken in the ROI across 400 images in the phantom using the standard DCE-MRI sequence. There is a clear drift in the signal of both coils across time, albeit there is less drift with Coil 2 compared to Coil 1 (0.8 % vs -2.1 % in 10 minutes). The smooth line shows a fit of the function of equation [6.1]. This behavior is not a function of signal from the phantom; removing the phantom and repeating the experiment results in the time trace of Figure 6.3 (Top panel, Right), fitted with the same function. On the other hand, phase across time when the phantom is removed shows no trend: a histogram of phase distribution in all 400 images in any one of the 4 coils of Coil 1 shows a mean of 0.009 ± 0.01 and a standard deviation of 0.905, as expected from white noise (mean 0.0 and standard deviation 0.907 is theoretical). Data not shown.

Cooling eliminates the significant downward drift (Figure 6.3, bottom panel). A 5-minute experiment in which the coil was cooled by draping an ice-filled bag across its upper surface showed no decrease in signal amplitude. Heating of Coil 1 generates a

visually evident decrease with time in receiver signal amplitude. All of the above findings were confirmed by Bruker scientists in similar experiments, with attention focused on resistive elements in the AD circuit.

6.3.1 Describing and correcting receiver gain drift

Coils 1 and 2 are both placed as the top half of a rat head-holder, with the vertical plane of the coil at right angles to the horizontal. Each coil and the associated active components sense varying parts of the signal from the sample in all of the slices and echoes. The horizontal intensities of the coil in a large phantom are approximately constant across the image, while in vertical (sagittal) sections there is a log-linear decrease from top to bottom (Supplementary Material, Figure S13).

The mean signal from horizontal ROIs in the phantom of single lines of the data (one pixel rows) across the time of the experiment produced a visually acceptable fit to the heuristic function of equation [6.1], with $c \cong 1.0$ when the slice pack index 1<i<400 is used as a measure of time; when $c \cong 1.0$, a is the 0-intercept. The factors a and b are highly correlated: across 102 horizontal ROIs in the phantom the correlation is 0.991±0.004. Thus, the correction for individual slices appears to vary mostly according to the 0-time value of each pixel with its shape common across slices, as might be expected when common components experience the same heating. This suggests that a function constructed by dividing the constants a and b by the estimated a from all data normalized to the 0-intercept can be applied directly to correct for receiver gain by dividing the time trace of each pixel by that factor:

$$S_c(x, y, i) = S(x, y, i) / \left[1.0 + \frac{b}{a} \cdot \ln(t_i + c)\right] \qquad \textbf{6.4}$$

where $S_c(x, y, t_i)$is the corrected intensity in pixel x,y of the i[th] slice pack, $S(x, y, i)$ is the uncorrected data, and a, b, and c are the derived constants from the baseline section of all data in the image. The derived common correction function was applied in one animal dataset and result presented in Figure 6.4. The image shows slice 3, echo 1 of a typical study in an animal with an implanted 9L tumor. The middle graph shows the sum of all data in each image of Slice 3, echo 1, points 3:100, with uncorrected and corrected data scaled by the function of equation [6.4] that was fitted to that data prior to CA injection. The right graph shows the effect of this scaling, with the same parameters a,b, and c, across all slices and echoes. The baseline is flat, thus allowing a stable estimate of the pre-contrast $\Delta R_{1p}(t)$, the change in longitudinal relaxation rate in plasma, and a stable estimate of the scaling factor for the group-averaged AIF.

Presented in Figure 6.5 (centre) is an example of compromised AIF estimate in an animal FL201, affected by the systematic error as a consequence of receiver grain drift. The Figure shows the group-averaged AIF and time trace of $\Delta R_1(t)$ in the caudate putamen. After the third image acquisition, it appears that the trace of $R_{1p}(t)$ approaches saturation, providing a baseline from which $\Delta R_{1p}(t)$ can be calculated upon delivery of CA. However, the signal itself approaches baseline in the second half of the time trace, thus requiring a relatively high scaling factor – in this case ~180, where the scaling factors in previous studies using Coil 2 average around 86. When applied with the same correction strategy that was applied to Figure 6.4 to this case, the data from caudate putamen (Figure 6.5, Right) was revised and the scale factor recalculated, resulting in a scale factor of 89 rather than 250. The new scaling factor lies within the confidence limits of prior studies with Coil 2 and a slice-pack repetition time of 4 seconds.

A subset of 9L test-retest animal studies was re-analyzed by applying the correction strategy explained in this study. Table S4 in the supplementary material presents the comparison summary of scale factor (SF) and K^{trans} constants for the paired studies before and after applying the correction.

The mean scale factor between the test-retest studies under uncorrected and corrected conditions were significantly different, lower for the corrected group ($p < 0.05$, Wilcoxon rank sign test). The mean of K^{trans} estimates were also lower, although the difference wasn't statistically significant. The mean K^{trans} for the corrected studies weren't significantly different ($p > 0.05$, unpaired t-test) from the previous studies[97] (acquired by Coil 2 at a lower duty cycle).

6.3.2 Identifying the source of receiver drift

The results of ours and the vendor's cooling experiments pointed to thermal effects as the source of loss of receiver amplitude signal. Thermal imaging of the coil (Supplementary Material, Figure S14) confirmed widespread heating of coil elements, mostly due to a source in the AD circuit.

As noted, a sweep of sequence parameters was conducted (Fig 6.7). The number of slices, the length of the transmission pulse, and the transmission pulse amplitude were varied. The single-echo SPGR study was not well spoiled; stimulated echoes, both additive (one slice) and subtractive (three slices), were evident in the study, but the trend across time was as observed in other studies, with a significant decrease in signal amplitude across time. Remarkably, little variation among sweep parameters was evident, with the exception of pulse length, where a longer pulse length (keeping flip-angle constant at 15°) visibly increased the receiver drift. This pointed conclusively to the PIN-switching circuit,

particularly to a resistor introduced to limit current in this coil (Coil 1), but not in Coil 2. Reducing the value of the resistor reduced the receiver drift (Supplementary Material, Figure S15).

6.4 Discussion

In this study, signal drift associated with Bruker 4-channel phased array receive coil during DCE-MRI acquisition was analyzed using a phantom study, and a correction based on that study was applied to a small sample of controls data in animals. The components in the coil heated significantly during a high duty-cycle sequence, resulting in the amplitude changes in the received signals, despite there being no change in the sample. The signal drift was persistent, independent of several experimental conditions: with or without phantom in place, with or without warm airflow supplied to keep the animal intact with ambient during the scan etc. In separate studies by Bruker BioSpin staff, the initial HFH studies in the phantom were confirmed, and the source of the heating and subsequent loss of Q in the receiver circuit was traced to a resistor meant to limit current in the AD circuit.

The coils in question are standard issue in Bruker small animal MRI systems for high-field studies in rodents. In general, stochastic studies that depend on an assumption of a constant receiver gain can be affected by this systematic source of error. In. particular, the 2% baseline signal drift in about 10 minutes of scan appears as a serious source of bias in DCE imaging applications in animal studies, where an accurate estimate of the dynamic change in CA concentration primarily depends on an accurate estimation of baseline R_1.

As noted, the heuristic fits of signal amplitude in phantom and the noise (Figures 6.2, 6.3) look promising. We accept some loss of accuracy in this fit because the correction is still relatively small (~2%) and because the next highest appropriate model, $S(t_i) = a + bt_i + ce^{-dt_i}$ has at least 4 nonzero parameters and often does not converge under lower signal conditions. The example of drift correction applied to AIF in one of the study (FL201) that resulted in stable flat baseline (shown in results, Figure 6.6) with the new scale factor lying within the confidence limits of prior studies with Coil 2 shows that the proposed drift correction provided a useful correction in existing DCE-MRI studies for systematic errors due to receiver gain drift. A correction for systematic errors in AIF amplitude will decrease the variance of estimates of the AIF contrast agent concentration, and thus correct estimates of K^{trans}, v_p, and of the derived estimate of v_e. Additionally, estimates of Flux and V_D in the mostly normal rim of the tumor[1], which are by-products of DCE-MRI derived parameters, are also affected by this corrected scaling factor.

These findings demonstrate that baseline drift observed during our DCE-MRI acquisition arises from thermal effects mainly in the active components of the receiver coil. This receiver-induced signal instability systematically affected AIF estimates and propagated to pharmacokinetic modeling and inflated scale factors across many studies. The resulting bias compromised the quantification of vascular parameters, e.g, K^{trans}, and the other microvascular parameters, emphasizing the critical need to consider hardware-induced artifacts in high-field, high-duty cycle dynamic imaging. Future studies should incorporate thermal stabilization strategies or correction algorithms in order to ensure the reliability of DCE-MRI-derived biomarkers.

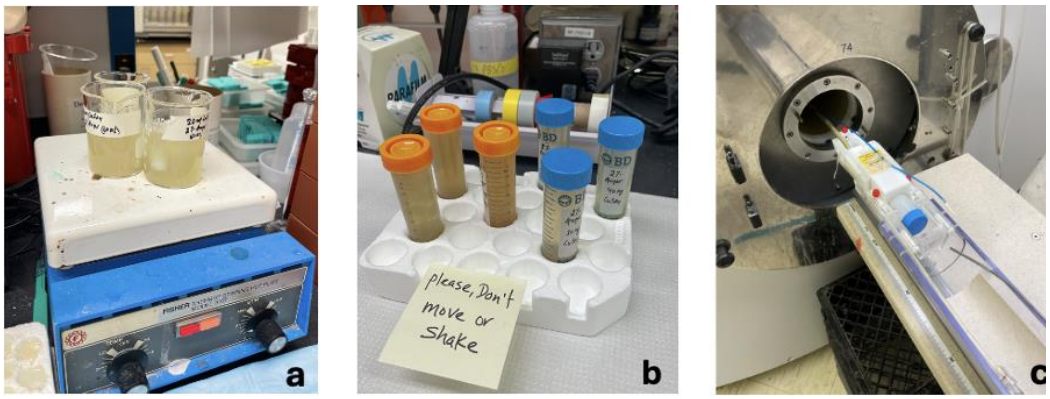

Figure 6.1: (a) Beakers containing Agar and $CuSO_4$ solution set on stirring hot plate set at moderate temperature for proper mixing (b) Plastic tubes filled with dissolved solution waiting for cooling to room temperature (c) Phantom set-up in the magnet: the phantom was firmly clipped into a plastic holder and positioned in the magnet with the surface coil in.

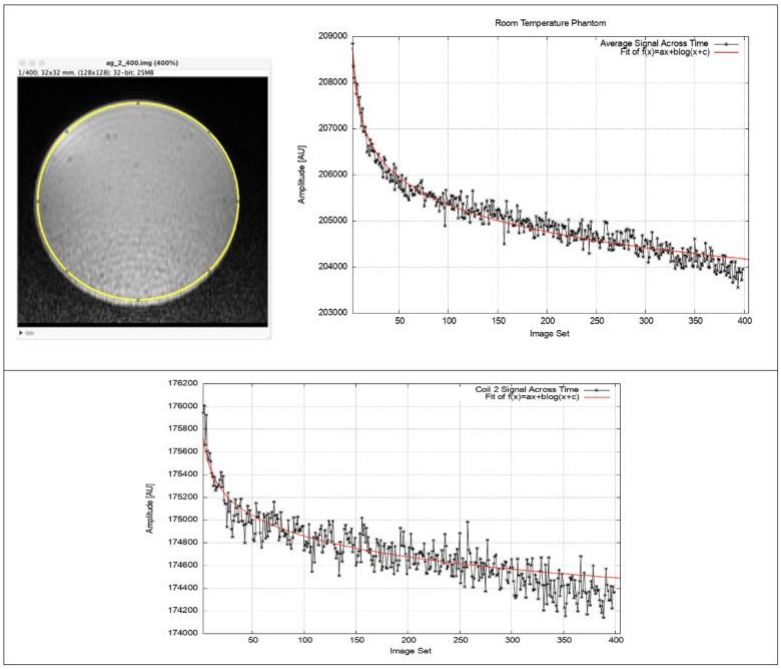

Figure 6.2: Top: Left: ROI in phantom. Phantom intensities are normalized to their means. Right: Coil 1 Amplitude change of -2.1% in average phantom intensity across ~10 min DCE-MRI study, 1.8% across 5 min. Bottom: Coil 2 Amplitude change of 0.8% in average phantom intensity across ~10 min, 0.6% across 5 min. A 3-parameter heuristic fit is shown as a solid line in both studies.

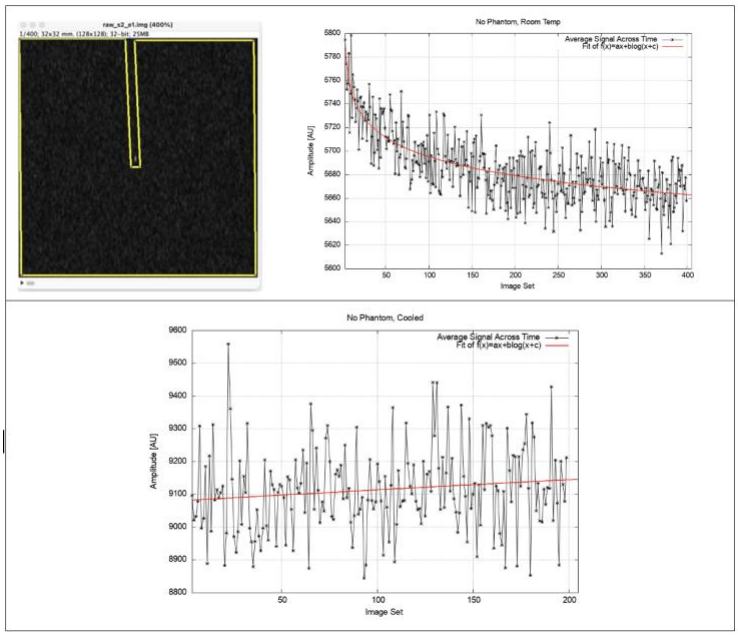

Figure 6.3: Top: Left: Images with no phantom. The ROI was selected to eliminate residual DC signal. Right: Coil 1 amplitude change in the selected ROI of -2.1% in average noise intensity across 10 min experiment, 1.7% across 5 min. Bottom: Amplitude change of ~ +0.6% in noise with cooled Coil 1 across ~ 5 min experiment. Apparent increase may be a result of more efficient cooling over time as the ice pack melted and made better contact with the coil.

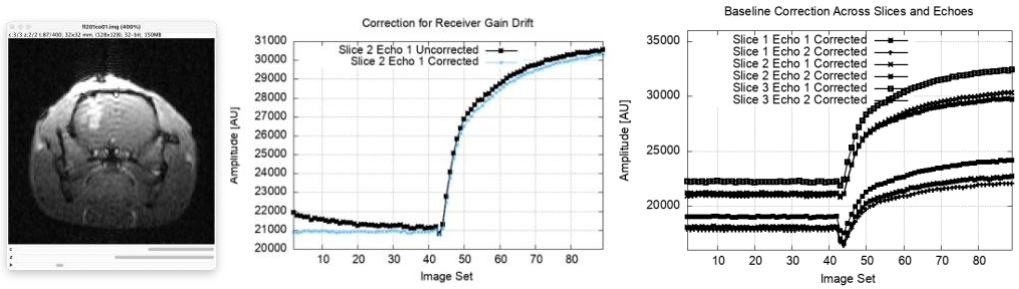

Figure 6.4: Receiver Gain Correction: Left: Slice image (Third) the correction was applied. Middle: All of the signal in the trace of Slice 3, Echo 1 is plotted for the first 100 points and the interval 3:41 is fitted with the function $S(i) = a + b \cdot ln(i + c)$. The correction of Equation [6.4] is applied, with the original data showing drift, and the corrected data showing a flat baseline. Right: In all slices and echoes, the correction results in a flat baseline.

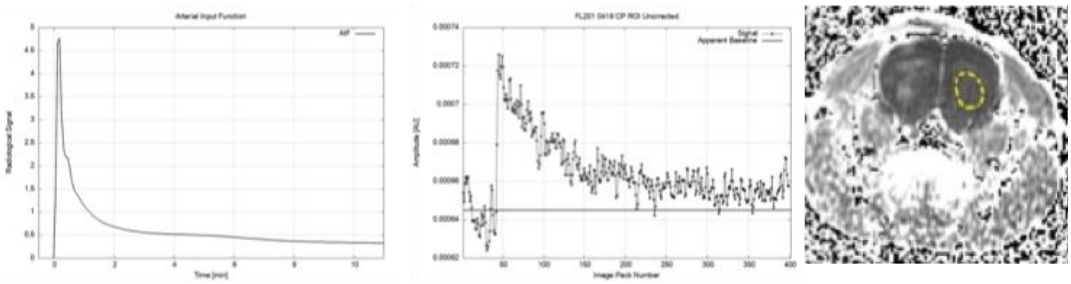

Figure 6.5: Left: The group-averaged AIF radiological estimate of change in contrast agent concentration taken from our earlier studies[79,53,54] (Radiological count on Y-axis, Time in minutes on X-axis). Center: Study, FL201_041922 - $R_{1p}(t)$ profile (R_{1p} on Y-axis and image pack number on X-axis). The group-averaged AIF was scaled by comparing the integral of the latter half of both traces. The baseline for pre-contrast R_{1p} was selected by examination and used to estimate $\Delta R_{1p}(t)$. Note that regions of the trace approach negative numbers, forcing an estimate of scaling constant to large values. Right: Example of the region of interest selection in contralateral normal brain caudate putamen.

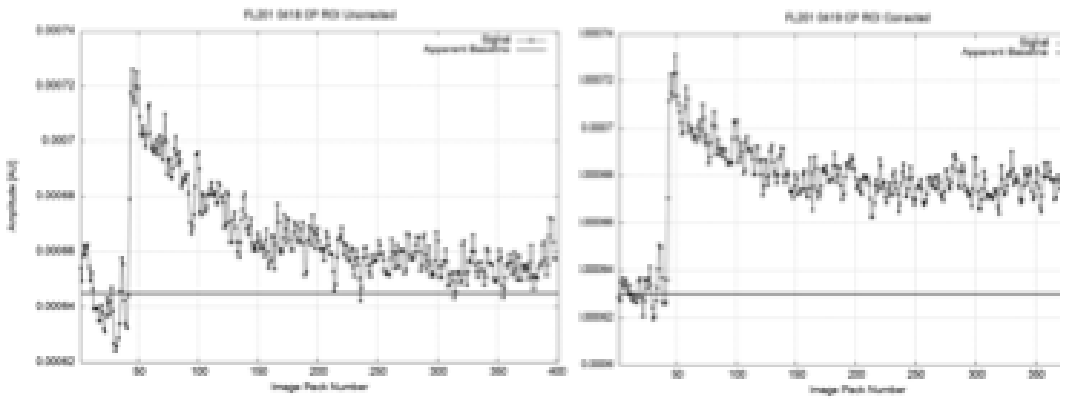

Figure 6.6: Left: Uncorrected data from the ROI of Figure 6.4. Right: Corrected data using the correction applied in Figure 6.3.

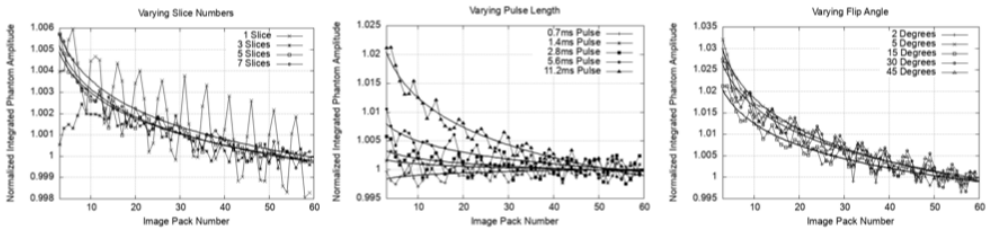

Figure 6.7: Left to right: Sequence parameter sweeps in Slice, Pulse Length, and Flip Angle. Constructive and destructive effects from stimulated echoes are evident, but only the Pulse Length sweep shows a strong relationship between receiver drift and the sweep variable.

CHAPTER 7

TUMOR INTERSTITIAL FLUID PRESSURE AND PERITUMORAL DISTRIBUTION VOLUME AS SIGNATURE OF RESPONSE IN AN IRRADIATED 9L RAT GLIOSARCOMA MODEL

This chapter presents the measurement of interstitial fluid pressure in 9L gliosarcoma tumor in rats and assesses treatment response to stereotactic radiosurgery using invasive TIFP and DCE-MRI. This chapter is prepared for submission for publication.

7.1 Introduction

Gliosarcoma(GS) is a rare but deadly neoplasm that shares many properties with GBM, including a similar median survival of about 14 months[22,30,89,91,200]. A subtype of GBM of mesenchymal phenotype/origin, GS can develop either as a nascent primary, or more commonly as secondary neoplasia after therapeutic craniospinal irradiation of primary GBM[184,201]. The mainstay treatment of GS mirrors the treatment of primary GBM[29,30] as its clinical features, including survival and failure patterns, mimic those of GBM [91,202]. The poor prognosis of GBM and its subtypes highlights the urgent need for new effective therapies.

Delivery of drugs, understanding of triggers to growth, and signatures of response to therapy, all require an understanding of tumor physiology in the context of the blood-brain and blood-tumor barriers. Over the past decades, studies[41,44,51,203] have demonstrated that tumor interstitial fluid pressure is a marker of tumor aggressiveness and response to therapy and a major obstacle to delivery of drugs to the tumor and

radiotherapeutic efficacy. Consequently, TIFP is an emerging biomarker of response in solid tumors.

The microenvironment of a solid tumor and its surroundings presents a complex domain of interaction of a number of physical parameters associated with tumor growth – vascular leakiness and its associated elevated TIFP, compressive stress, stiffness, tissue fluid content etc.[41,84,204-207]. In an embedded U251N orthotopic xenograft animal model of GBM[1], these physical forces, leading to compression of peritumoral tissue, resulted in an exudate flux that strongly correlated with the extracellular distribution volume in the tumor's rim[1]. It is hypothesized that the dynamics between TIFP, V_D, Flux in association with other relevant vascular parameters can be predictive of response to therapies in embedded tumors, such as those typically found in the brain.

Jain et al[49,52], and others[39,51] have reported a decrease in interstitial fluid pressure in a group of tumors treated either with chemo- or radio-therapy. In this study, we explored the changes in TIFP and other associated vascular parameters that occurred following radiotherapy.

Tumor bearing rats were irradiated with stereotactic radiosurgery (SRS) at the dose expected for total control in half the animals (the TCD_{50} dose)[13,194,208], subsequently scanned using DCE-MRI[2,5,41,58,60,61,97], then subjected to a measurement of TIFP. Hence, this study focused on the relationship between measures of TIFP and DCE-MRI derived V_D and Flux under irradiated and unirradiated conditions in an orthotopic model of gliosarcoma in rats. TIFP was measured in tumors under stated conditions using the WIN technique following published methods[41,52]. Physiological parameters of the tumor and peritumoral regions were evaluated to identify a signature of response in the irradiated

group. V_D and other microvascular parameters, v_p, K^{trans}, v_e, and Flux were estimated using DCE-MRI data.

7.2 Materials and methods

7.2.1 Tumor implantation

All experimental procedures were approved by the IACUC according to federal regulations of Policy on Humane Care and Use of Laboratory Animals (Protocols #1279 and #1546). Twenty-two male immune-competent Fischer-344 rats (~7 weeks old; Charles River, Kingston, NY) were intracerebrally implanted with 9L cells following published procedures[58,97]. Briefly, animals were anesthetized with isoflurane (4% for induction, 0.75 to 1.5% for maintenance, balance N_2O:O_2 = 2:1). Under aseptic conditions, the surgical area of head was swabbed with Betadine solution and alcohol, the eyes coated with Lacri-lube (Allergan Inc., Parsippany-Troy Hills, NJ) and the head immobilized in a rat stereotactic device (Kopf, Cayunga, CA). A 1 cm incision was made 2 mm right of the midline and the skull exposed. A burr hole was drilled 3.5 mm to the right of bregma, keeping the dura intact. A #2701 10 μL Hamilton syringe with a 26-gauge needle containing 9L tumor cells freshly harvested from log phase growth (5×10^4 in 10 μL of phosphate buffered saline) was lowered to a depth of 3.0 mm and then raised back to a depth of 2.5 mm. Cells were injected at a rate of 0.5 μL/10 s until the entire volume was injected. The needle was then gently withdrawn; the burr hole sealed with sterile bone wax and the scalp incision closed with sterile nylon sutures.

7.2.2 Experimental preparation

All tumor implanted rats were monitored by MRI (post contrast T_1-weighted high resolution) for tumor size and location. When tumors grew to about 3 to 4 mm in

diameter, an MRI study with DCE-MRI was performed, as previously described[2,5,58,60,61,97]. The lateral tail vein was used for contrast agent administration, and the body temperature was maintained at 37°C with warm air supply and monitored via an intra-rectal type T-thermocouple. Two DCE-MRI studies were acquired for each animal studied. The initial scan was performed before irradiation and 24 hours prior to the second scan which followed radiation and preceded a WIN measurement; the second scan was performed after two hours after irradiation. The two DCE-MRI scans in rats not receiving radiation were also separated by 24 hours. All second MRI studies were followed by the TIFP WIN procedure, after which the rats were euthanized and the brain removed for histology.

7.2.3 MRI study

The MRI studies were performed in a Varian/Magnex (Santa Clara, California), 7 Tesla, 20 cm bore magnet system with a Bruker console using Paravision 6.0 software. Gradient maximum strengths and rise times were 250 mT/m and 120 μs respectively. All MRI image sets were acquired with a 32 x 32 mm field of view (FOV). Transmit and receive coils included a Bruker Quadrature Birdcage (transmit) and a 4-channel phased-array surface coil receiver (Rapid MR International, Columbus OH). T_1-weighted high-resolution images were acquired pre- and post-contrast injection for co-registration with post-mortem histopathology images. These images were acquired with the following parameters: 256 x 192 matrix size, 27 slices, 0.4 mm thickness, 0.1 mm slice gap, number of echoes (NE) = 1, number of averages (NA) = 4, TE/TR = 16/800 ms. Magnevist (gadopentetate dimeglumine; 0.25 mmol/kg, Bayer Healthcare, Wayne, New Jersey) was used as the contrast agent in 12 animals and Dotarem (gadoterate meglumine; 0.1

mmol/kg, Guerbet LLC, Princeton, NJ, USA) as the contrast agent in 10 animals. CBF was estimated in single central slice using ASL spin echo technique using published methods[71,188] with the following parameters: 128 x 64 matrix size, 1mm thick slice, NA = 1, TE/TR=14/5000, Arterial labeling = 1s, Total time ~ 5 min. ADC data was acquired via diffusion weighted imaging (DWI) pulsed gradient spin-echo sequence in three directions (x, y, z) and summarized by reporting the trace of the matrix of ADC values. The DWI parameters were as follows: matrix size=128 x 64, 15 slices, slice thickness = 0.8 mm with 0.2 mm gap, TR = 1500 ms, TE = 40 ms, diffusion b-values = 0, 895, 1792 s/mm^2, gradient amplitude = 107 mT/m, gradient duration = 10 ms, Two consecutive Look-Locker (LL) sequences were run before injecting the contrast agent, and two were also run after the completion of the 10 min DCE-MRI sequence to generate pre- and post-contrast voxel-by-voxel maps of T_1 in the tissue. The LL sequence parameters were as follows: FA = 25^o, 128 x 96 matrix size, five 1.9 mm slices, 0.1 mm gap, NE = 24 inversion-recovery echoes, TR = 2000 ms. The DCE-MRI sequence used was a dual-echo spoiled gradient-echo sequence with 400 acquisitions at 1.5 s intervals, 128 x 64 matrix size, three 1.9 mm slices with 0.1 mm gap, FA = 18^o, NE=2, NA=1, TE=2.0 ms, TR=24.2 ms, spectral width=150 kHz. The CA was injected by hand push via tail vein about one minute after the start of the sequence. The DCE-MRI total run time was ~ 10 min. A three-dimensional FLASH gradient echo sequence was also acquired to co-register the MRI images to cone beam CT (CBCT) images with the following parameters: matrix size = 256 × 192 x 96, slice thickness = 24 mm single slice, TE = 2700 ms, NE = 1, FOV = 42 × 32 × 24 mm^3, spatial resolution of 0.164 × 0.167 × 0.25 mm^3, NA = 1, flip angle = 20^o.

Initially, a review of our DCE-MRI data showed that the data acquired using a Bruker BioSpin 4-channel phased-array rat heat coil used in this study resulted in a greater test-retest variances compared to a similar 2-channel coil from the same manufacturer but with a different active decoupling electronics and a less demanding duty cycle. Phantom studies were performed to investigate the issue, and it was found that the heating in active components of the coil changed the receiver signal amplitude ~2.1% during the DCE acquisition. Follow up studies by Bruker Biospin staff replicated our finding. A correction strategy was developed based on heuristic logarithmic function and the dataset was re-analyzed to correct the underlying drift, leading to a flat, stable baseline.

7.2.4 Tumor irradiation

When the embedded portion of the tumor were about 3-4 mm, rats were irradiated in an XSTrahl (XSTrahl, Suwanee GA, USA) small animal radiation research platform (SARRP). The SARRP beam produced 220 kVp photons that generated an approximate effective energy of 70 KV using 0.15mm copper filter. Rats were positioned in a temperature-controlled cradle under isoflurane anesthesia (3% for induction, 1-2% for maintenance, balance N_2O:O_2 = 2:1). The head was immobilized using a mouth bite piece and body alignment was checked using laser registration. Images were acquired using SARRP's CBCT system and co-registered with 3D-GRE MR images. A treatment plan was produced using Xstrahl's MuriPlan software with four non-coplanar beams with a common isocenter located approximately at the center of the tumor volume. An SRS dose of 25 Gy was delivered treating the entire tumor to 80% isodose level with a dose rate 2.5

Gy per minute. Rats were imaged with DCE-MRI to assess vascular and physiological changes 2 to 3 hours after irradiation.

7.2.5 DCE analysis and tumor vascular parameters

DCE-MRI data was analyzed using published methods[2,5,59,97] based on Patlak[18], extended Patlak[17], and Logan[56] graphical approaches. In general, the change in the tissue's longitudinal relaxation rate R_1 after administration of contrast is approximately proportional to the CA concentration in tissue[60,189]. Thus, the voxel-by-voxel concentration-time trace was estimated using $\Delta R1(t)$[2,5,61,97]. A voxel-by-voxel data-driven approach to model selection[5,58,60,61] was employed to segment the brain tissue based on the three-parameter standard model, or nested lower order model, with the winner determined by an F-test. Following this, model-selection generated maps of microvascular parameters were produced along with a map of the number of parameters used to characterize the selected model itself. This produced at most an approximately unbiased estimate of K^{trans}, v_p, and the reflux rate constant from the EES to blood plasma (k_{ep}); v_e was calculated as the ratio of K^{trans}/k_{ep}. In detail, the models by the number of parameters were, (i) model 1: the tissue region with no detectable CA leakage to the EES, i.e., the normal vasculature ($v_p \neq 0$, $K^{trans} = k_{ep} = 0$); (ii) model 2: the tissue region with leakage, but having little or no measurable reflux from EES to the microvasculature ($v_p \neq 0$, $K^{trans} \neq 0$, $k_{ep} = 0$); (iii) model 3: the tissue region with highly leaky vasculature with measurable backflux from EES to the vasculature ($v_p \neq 0$, $K^{trans} \neq 0$, $k_{ep} \neq 0$). In contrast to the voxel-by-voxel approach, Flux and V_D were calculated by summing the dynamic $R_1(t)$ estimate in ROIs drawn at the tumor edge (defined by the edge of the Model3 ROI), the immediately adjacent 1-pixel wide outer

ROI, and a larger 'catchment' ROI placed outside the tumor edge as described by Ewing et al[1]. Logan and Patlak graphical analyses provided estimates of Flux and V_D.

7.2.6 Image processing and statistical analysis

The data-driven DCE-MRI data analysis and the selection of ROIs in model 3 tumor followed established procedures[2,41]. The MRI slice with the largest model 3 tumor cross-section from each scan was selected for parameter summary in each animal studied. The mean from each ROI considered was taken as the final summary parameter, and the normalized mean difference of estimated parameter between the first and the second study ([second minus first]/[second plus first]) in each cohort were reported as mean ± SEM. This latter statistic differs from the usual calculation of percentage change but has the virtue of avoiding bias in its measure. TBF was normalized to the contralateral normal brain, and the normalized mean difference between the first and the second scan was reported as mean ± SEM as noted. An unpaired t-test was used to evaluate any difference in reported parameter means between irradiated and unirradiated control studies.

7.2.7 Tumor interstitial fluid pressure in cerebral gliomas

Highly elevated fluid pressure is the hallmark of solid tumors. Leaky tumor vessels, absence of lymphatic drainage, abnormal structure and function of the interstitium and dense tumor architecture, confined cranial space etc., collectively elevate TIFP in cerebral tumors[41,44,48,49]. In a normal tissue bed, the intact BBB retains plasma proteins within the vasculature, thus maintaining a microvascular-to-interstitial oncotic pressure gradient that counterbalances the hydrostatic forces generated by microvascular pressure[45,209]. Normal microvasculature is then supported by a balance between intravascular pressure and the much lower pressure in the surrounding tissue, so the

vessels remain open and perfused. In tumors, however, IFP can rise to levels approaching the MVP due to leaky vessels, protein accumulation in the interstitium, and the absence of efficient lymphatic drainage[26,45,48,210]. When the pressure outside the vessel (IFP) nearly equals or even transiently exceeds the pressure inside, the mechanical result is partial or complete vessel compression; a phenomenon Jain et al. refer to as vascular collapse[45]. The consequence is the reduction in the effective perfusion pressure because the gradient between arterial input and venous output is reduced. Blood flow becomes sluggish and spatially heterogeneous, creating pockets of hypoxia even in well-vascularized tumors[45,50]. This interplay between high IFP, vascular compression, and reduced perfusion pressure not only limits oxygen and nutrient delivery but also significantly impairs the transport of therapeutic agents[26,211], reinforcing the importance of strategies that normalize the vasculature and lower IFP to restore both perfusion and drug delivery[46,212].

7.2.8 TIFP measurement using wick-in-needle technique

TIFP measurements followed the established procedures as described by Elmghirbi et al[41]. A 23-gauge fluid-filled needle inserted into the tumor bearing rat's brain through the same burr hole drilled at the time of tumor cell implantation was used to measure TIFP. Prior to the measurement, the needle and the pressure gauge transducer system were first calibrated using an experimental set up that remained intact throughout the entire course of pressure measurement in the animal. The needle had a side port length of 2mm located approximately 3.5 mm from the needle tip; the tip was sealed applying bone wax to avoid any possibility of clogging. The distal 1 to 2 cm portion of the needle was filled with a polyester multifilament thread. A 6 cm long pipette

containing artificial CSF (aCSF) was mounted vertically in a metal stand and the needle was connected at its bottom. The needle was then connected to a transducer (FLUKE Biomedical) via a Luer-Lock connection and coupled with the strain gauge meter (model PAXLSG, Red Lion Controls, York, PA) via a small pipette using a T-connector. The entire pipette connection and the needle were thoroughly rinsed with aCSF and any air bubbles present in the system were removed. After completing the apparatus set-up, the strain gauge meter was calibrated in a pressure range from 0 to 30 mmHg.

After the MRI study, the animal was removed from the scanner and placed in the same stereotactic frame that was used for tumor implantation. The head was immobilized, a middle incision was made, and the skull exposed. The rat's head was positioned at the same level as the pressure transducer during the calibration. The WIN needle was inserted vertically into the tumor through the existing burr hole. The needle was advanced in steps of 0.5 mm each time and kept stationary until the measured pressure reading stabilized; the pressure was recorded every 2 minutes. The process continued until the side port of the needle completely passed the tumor diameter. Following the WIN-TIFP, the animal was placed back to the scanner and T2 weighted MRI was repeated to check the needle track and make sure that the needle passed through the central slice of the DCE-MRI measurement. The pressure-depth profile was plotted, and central pressure was estimated by averaging three pressure readings around the plateau, viz, at a reference point in the plateau according to the tumor depth, 0.5 mm above and below it.

7.2.9 Histopathology

Histopathology procedures followed published methods[97]. Following the TIFP measurement, the animals were maintained under isoflurane anesthesia and perfused

transcardially with normal saline, followed by 4% paraformaldehyde as a fixative. The brains were carefully removed and kept in fixative overnight. Using a rat-brain matrix (Activational Systems, Inc., Warren, MI), 2-mm-thick coronal sections through the tumor region were prepared. The tissue was then processed with a VIP Tissue Tek Processing system and embedded in paraffin. From the paraffin block, 6-µm-thick sections corresponding to the selected MR imaging slice were cut and mounted on Superfrost Plus (Fisher Scientific) slides. The section containing the largest tumor region was stained with H&E for ROI evaluation. Images were acquired with a Nikon Eclipse E800 microscope using ACT1C software.

7.3 Results

Twenty-six tumor bearing rats were randomly divided into two groups containing thirteen animals in each. All manifested BBB breakdown in post-contrast T_1-weighted images and in their pharmacokinetic maps. Tumor extent and location were examined based on post contrast T_1 and T_2-weighted images and confirmed with post-mortem H & E-stained images. The animals were either treated with radiation therapy (the treated group) or received no radiation (the control group). Two DCE-MRI images were acquired for each animal, and TIFP measurements were performed after the second MRI. One animal from the treated group and three animals from the control group were censored from DCE-MRI data analysis for variety of reasons such as excessive motion during MR scan, bad input function, etc., leaving a total of 12 animals in the treated group and 10 animals in the control group for DCE-data analysis. No WIN-TIFP measurements were censured.

The mean TIFP ± standard error of the mean (SEM) was 11.58 (±1.38) mmHg and 8.14 (±0.81) mmHg for control and treated groups respectively (Table 7.1). TIFP in the treated group was significantly lower ($p < 0.05$) indicating a signature of radiation response. An example of a pressure-depth profile obtained from one of the 9L animals under study is shown in Figure 7.1 (Right). The profile showed an initial sharp rise in pressure on entering the tumor mass, a gradual rise reaching a central plateau, and a sharp decrease while exiting the tumor. A T_2-weighted high-resolution image post-TIFP measurement shown on the left of Figure 7.1 depicts the needle track through the tumor mass confirming the needle advanced right through the body of the tumor.

The group mean of the normalized mean test-retest differences of microvascular parameters v_p, K^{trans}, v_e, and V_D for treated and control groups are summarized in Table 7.2. TBF, V_D, and Flux are also reported. Taking the mean in each animal of the model 3 region for each parameter as a measure of tumor physiology, and the test-retest normalized difference in each animal under each group as a measure of response to radiation, the grouped mean differences for estimated vascular parameters were evaluated. The Flux, V_D, and TBF were significantly reduced in the treated group ($p < 0.05$, t-test); v_e was also reduced in the treated group but only marginally significant ($p = 0.052$). Although K^{trans} also decreased in the treated group, it wasn't significantly different than the control group ($p = 0.9$). The distribution volume in entire model 3 tumor and v_p also weren't significantly different between the two groups.

The Flux and V_D in the treated and the control cohorts were strongly correlated as shown in Figure 7.2 ($R^2 = 0.84$ and 0.92 for the control and the treated groups respectively), with slope and y-intercept of the regression lines significantly different

from each other ($p < 0.05$). A significantly different regression trend in the treated group from that of the control points to a different physical state of glioma, with IFP and the majority of the measured tumor parameters reduced in the aftermath of radiotherapy. The graph of Flux and V_D including all the first scans (test studies having no irradiation) in each cohort was compared with that of the second studies (retest, no radiation) from the control group (Supplementary Material S16), which resulted in regression lines with identical slopes (0.50, 0.52) and R^2 (0.84, 0.79) fortifying the robustness and consistency of the relationship. Similarly, Figures 7.3 and 7.4 are the graphs plotted between measured TIFP and V_D or Flux for each cohort, exhibiting a weak correlation between them. However, it can be noted from the graphs that the means of the V_D and Flux estimates in the treated group are below the control group, in consort with the reduced fluid pressure after RT. The estimate of the mean distribution volume in the inner ROI of model 3 tumor was significantly larger than that of the immediately adjacent outer ring in both the first and the second study in both groups ($p < 0.004$, Wilcoxon rank sign test) and were highly correlated as shown in Figure 7.5. This points to a lowered porosity, probably related to a concentration of compressive forces in the tumor periphery. Moreover, the mean inner and outer edge V_D for the treated group were significantly lower than those in the control group ($p < 0.004$, t-test), suggesting an increase in compressive forces following irradiation.

Figure 7.6 shows an example of (i) tumor central necrosis acquired with post-contrast T_1-weighted image, (ii) H&E-stained section, (iii) DCE-MRI model 3 map, and (iv) magnified view of necrotic region shown by rectangle in Figure (ii).

7.4 Discussion

In this study, the physiology of therapeutic intervention 2-3 hours after irradiation was explored using DCE-MRI. In addition to the conventional assessment of whole-tumor parameters (tumor blood flow, vascular permeability, etc.), novel measures of peritumoral distribution volume and the associated Flux were evaluated. Ewing et. al[1,54], established that the tumor exudate flux and V_D were highly correlated in a variety of treatment-naïve preclinical glioma models. This led to a suggestion that the relationship might be used to noninvasively estimate TIFP[41], and to the development of computational mechanical studies of solid stresses and fluid fluxes based on the DCE-MRI data[84,120].

The present study explores Flux-V_D relationship, TIFP, and TBF, as well as other measures, in radiotherapy-treated and untreated 9L syngeneic gliomas. Earlier findings of strong positive correlation between the Flux and V_D in both treated and untreated cohorts were reproduced. TIFP was measured using the WIN technique, showing, as expected, a significant reduction in the RT group; V_D and Flux showed a strong positive correlation and were significantly reduced in the RT group, suggesting a signature of treatment response. A plausible explanation (supported by the significant decrease in relative blood flow) is that an acute dose of RT decreases perfusion[13,213], reducing fluid input into the interstitium and pressure gradients[26]; the end result is the reduced TIFP and Flux. These reductions are associated with a decrease in interstitial space in the tissue external to the tumor, suggesting that RT-associated cellular swelling acutely throttles vessels feeding the tumor, in line with Jain's observations[205]. We note that this presents a picture of embedded tumor physiology that is essentially dependent on the supply of nutrients delivered from

the surrounding parenchyma and is regulated by the physical state of the tissue at the boundary of the tumor.

As noted from Figure 7.5, both the treated and the control group displayed a regression slope between the inner and outer rim distribution volume that was less than 1 (0.57 for control and 0.42 for the treated group), indicative of compression of peritumoral distribution volume. While the slope was lower for the treated group, suggesting more compressive forces than in the control group, the difference in slopes was not statistically significant.

The parameters K^{trans} and v_p did not change significantly between the treated and the control groups, but v_e was reduced in the treated group and was marginally different ($p = 0.051$). A reduction in v_e in irradiated gliomas indicates the loss of extracellular-extravascular space. Both this, and the consistent gradient in V_D at the rim of the tumor, point to cellular swelling post irradiation[13,99]. Similarly, a significant reduction in TBF in the treated group is indicative which supports the hypothesis that cellular swelling post-RT is the source of solid stresses that compress feeding vessels and throttle the delivery of fluid to the tumor. Since K^{trans} is the product of extraction fraction and flow, the small net decrease in K^{trans} is a signal of increased permeability-surface area product due to vascular radiation damage in the treated group. An inconsistent trend in change of K^{trans} as an acute response to drugs, to radiation, or to a combination of both in different tumor models have been reported by several authors[13,59,95,98,99], and lends a note of caution to its use in evaluating response to therapy.

Figures 7.3 and 7.4 investigated whether V_D or Flux alone would be an alternative to characterize interstitial fluid pressure in embedded gliomas as they were strongly

correlated and had a clear signature of treatment response (Figure 7.2). Although the graphs (Figure 7.3, 7.4) showed virtually no correlation, both Flux and V_D in the treated group largely tend to cluster below the control group, suggesting treated tumors rest in a different physiological state as characterized by various imaging biomarkers analyzed earlier in this study. However, it should be noted that the peritumoral distribution volume compression is not the function of IFP alone, but a biphasic approach that takes into account the solid compressive stress resulting from tumor growth, tissue porosity etc., would give a more complete picture of mechanical compression at the tumor rim[84,204,207].

To summarize, the behavior of IFP in a preclinical embedded cerebral glioma and its correlation with DCE-MRI derived vascular and tumor microenvironment parameters was studied. An acute dose of radiation (25 Gy) produced a significant reduction in TIFP accompanied by a significant reduction in TBF, Flux, and V_D. The combination of acute changes in these measured parameters after RT point to the tumor-parenchyma interface as the essential regulator of tumor physiology, and to post-RT cellular swelling as the responsible player in the acute reduction of TBF and TIFP. This finding may suggest that planning the sequence and/or timing of RT and adjunct therapies could improve the delivery and efficacy of both.

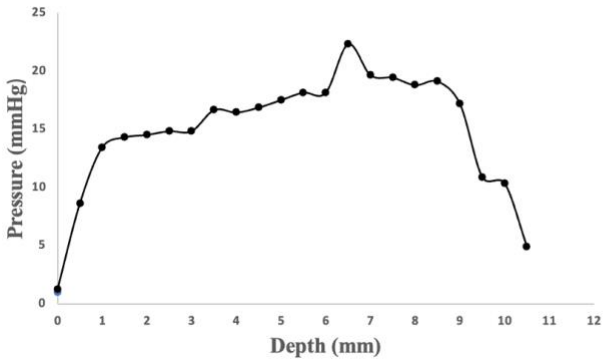

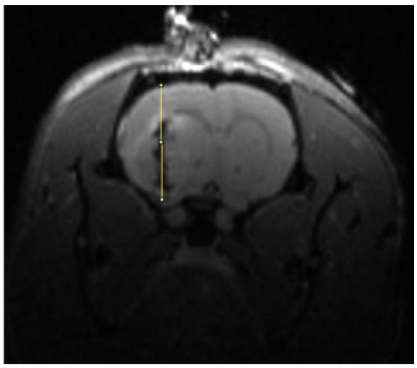

Figure 7.1: Left: Pressure-depth profile obtained from WIN measurement in one of the 9L animals. The profile shows an initial sharp pressure rise, a gradual increase reaching a central plateau, and a sharp fall off exhibiting sharp peripheral gradient while exiting the tumor. Right: High-resolution T_2-weighted image acquired post TIFP showing the needle track through the tumor mass; line drawn in the tumor mass to make the needle track visible.

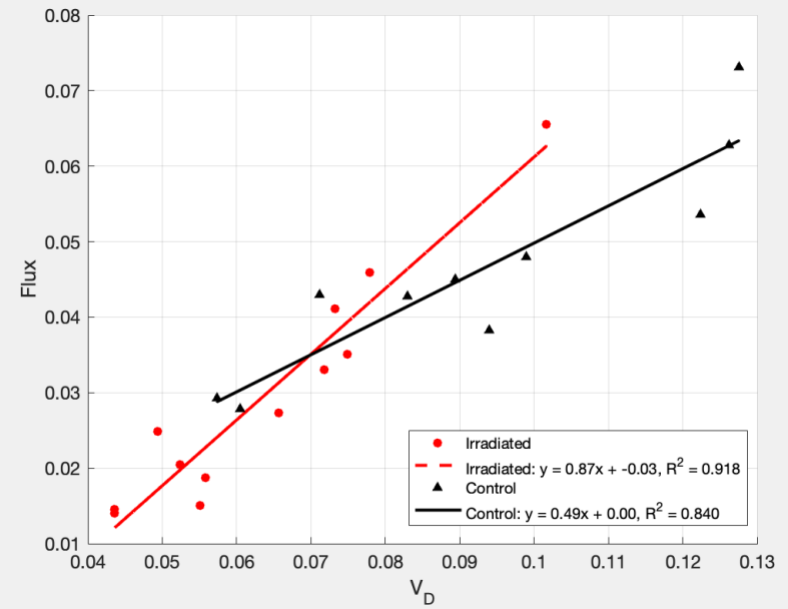

Figure 7.2: Peritumoral distribution volume vs Flux, showing a strong correlation, $R^2 = 0.92$ and 0.84 for treated and control group, respectively. Note the slope and y-intercept of the regression lines which are significantly different to eachother ($p < 0.05$).

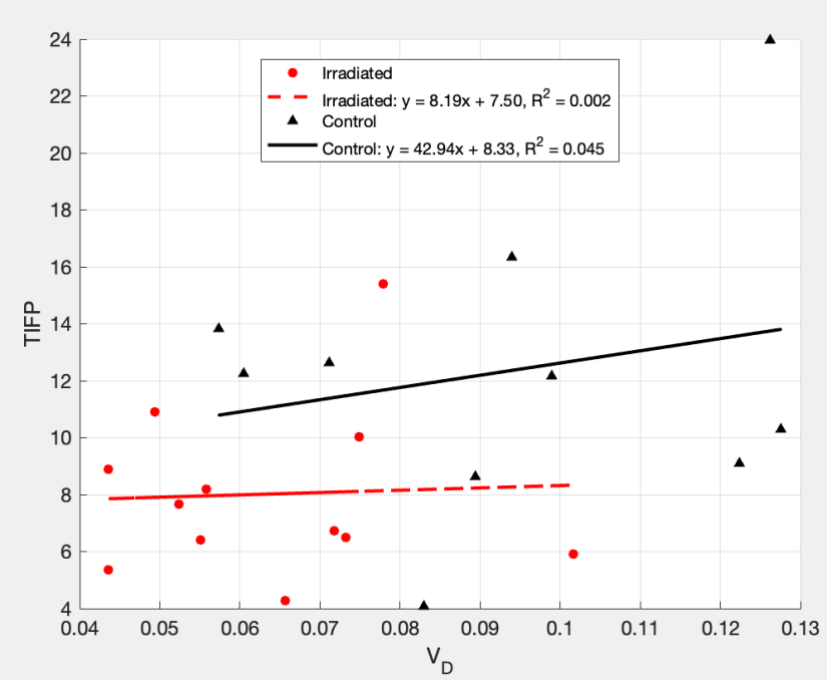

Figure 7.3: TIFP vs V_D for treated and control group. They are weakly correlated, but majority of the V_D values in treated group tend to cluster down the control group.

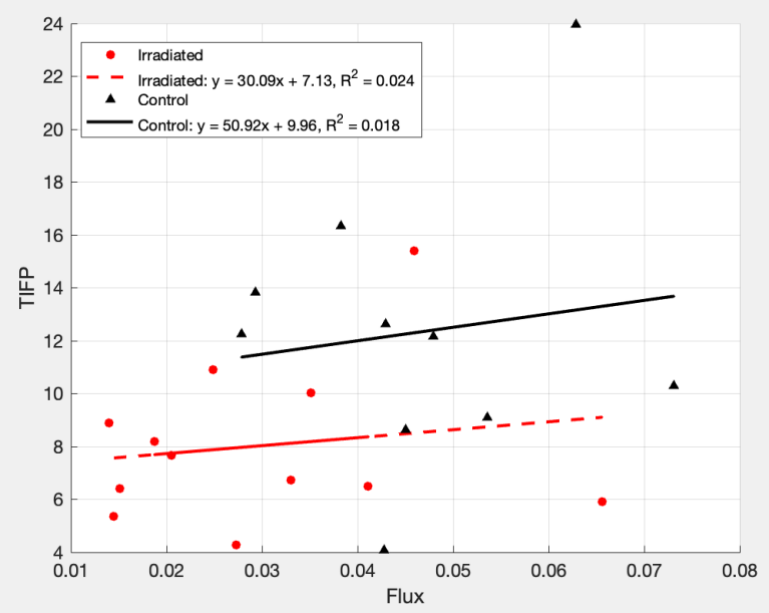

Figure 7.4: TIFP vs Flux for treated and control group. They are weakly correlated, but majority of the Flux values in treated group tend to cluster down the control group.

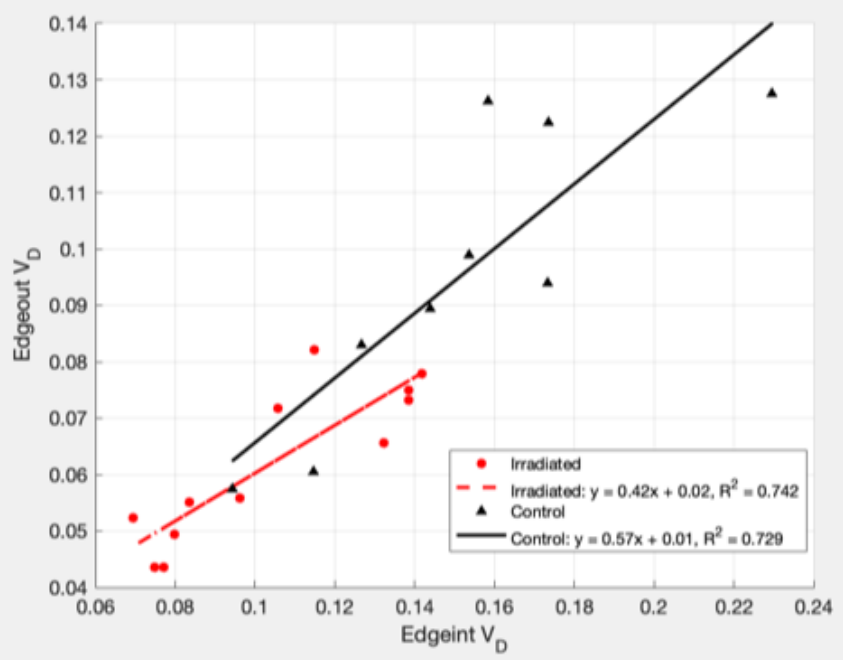

Figure 7.5: Inner (Edgeint) vs outer (Edgeout) edge V_D comparison for treated and control groups. They are highly correlated ($R^2 = 0.7$ for either group) with mean inner and outer edge V_D significantly lower in the treated group.

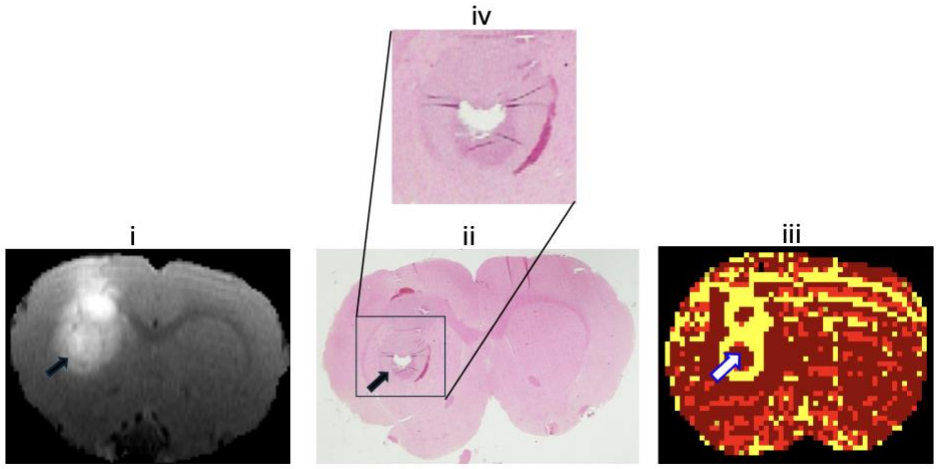

Figure 7.6: Example of central necrosis in the tumor: (i) Post-contrast T_1-weighted image exhibiting necrotic core (indicated by black block arrow), (ii) H&E-stained histopathology image (necrotic core indicated by black block arrow), (iii) DCE-MRI generated model 3 tumor map (central necrotic region shown by white block arrow inside yellow model 3 tumor). Note the fidelity of model map with the histopathology image shown. (iv) Magnified view of necrotic area of the tumor shown in (ii) by rectangle.

Treated	TIFP (mmHg)	Controls	TIFP (mmHg)
FL150	5.91	FL142	7.13
FL152	6.733	FL154	12.633
FL153	7.666	FL169	7.1
FL156	10.033	FL180	13.033
FL158	6.4133	FL212	4.06
FL163	8.8867	FL213	13.83
FL165	9.62	FL214	8.616
FL219	5.35	FL223	9.0833
FL221	6.4833	FL224	10.3
FL222	4.2833	FL226	23.95
FL229	10.9	FL227	12.15
FL230	8.2	FL232	12.25
FL231	15.4	FL233	16.35

Table 7.1: Tumor interstitial fluid pressure in RT-treated and control group measured using wick-in-needle method.

Parameters	Controls (Mean ± SEM) x 10^{-2}	Treated (Mean ± SEM) x 10^{-2}	p-value
v_p	4.85 ± 6.83	19.24 ± 8.24	0.22
K^{trans}	-3.80± 11.03	-5.33 ± 7.34	0.91
v_e	1.39 ± 4.02	-8.02 ± 2.52	0.051
V_D (peritumoral)	6.08 ± 2.60	-2.96 ± 2.53	0.02
Flux	8.61 ± 3.72	-6.88 ± 5.28	0.04
TBF	-4.01 ± 1.55	-17.30 ± 3.93	0.004

Table 7.2: Estimates of major vascular parameters in treated and the control group reported as mean ± SEM as noted in methods. The mean here refers to the normalized mean difference between the corresponding parameter means between the first and the second MRI studies. The units of K^{trans}, TBF, and Flux are mL.gram^{-1} min^{-1}, ml/100 ml-min, and $\mu m^3/\mu m^2 s$ respectively, others are unitless.

CHAPTER 8

SUMMARY AND FUTURE DIRECTIONS

A summary of major findings of this dissertation is presented and further avenues for extending this research are recommended.

8.1 Summary

This research focused on three critical aspects of DCE-MRI studies. First, DCE-MRI was used to quantitatively assess microvascular and tumor microenvironment parameters in a PDOX GBM model to strengthen its role as a pre-clinical platform. Second, fluid dynamics were investigated by measuring interstitial fluid pressure in 9L gliomas under radiotherapy-treated and untreated conditions, integrating invasive measurements with DCE-MRI parameters to identify biomarkers of IFP and treatment response. Third, a systematic bias from a RF coil heating in a 7T magnet while employing DCE-MRI was characterized, and a correction method was developed to improve the accuracy of pharmacokinetic modeling.

In the first part of this research presented in chapter 5, measures of physiology in PDOX models of primary and recurrent GBM (HF3016, primary, and HF3177, the recurrent) resected from the same patient were studied. The microvascular parameters v_p, K^{trans}, v_e, and peritumoral exudate flux and distribution volume in TME were assessed using DCE-MRI. Moreover, ADC was measured using DWI and TBF with arterial spin labeling techniques. The parameter summary of table 5.1 serves as benchmark values of tissue parameters in PDOX tumors. This serves as a baseline for testing novel therapies. The most important finding of this section was the significantly elevated peritumoral

distribution volume, and the large interstitial volume fraction compared to that of 9L and U251 tumor models. Estimates of v_e in both PDOX models were significantly higher than those of U251N studies ($p < 0.002$, unpaired t-test). Moreover, v_e for PDOX HF3177 studies was significantly higher than the estimate for 9L tumor model ($p < 0.003$, unpaired t-test). The PDOX HF3016 v_e estimate was larger than that of 9L studies but the difference was not statistically significant. As to V_D, the peritumoral distribution space in the PDOX tumors, the mean estimated V_D ($14.4 \times 10^{-2} \pm 3.37 \times 10^{-2}$ and $15.4 \times 10^{-2} \pm 2.79 \times 10^{-2}$ for HF3016 and HF3177, respectively) were significantly greater than the estimates for U251N tumor model ($p<0.03$). The mean V_D estimate from HF3177 was also significantly greater than that of 9L tumor model ($p<0.04$) whereas the V_D estimate from HF3016 was larger than in the 9L model, but not statistically significant. Moreover, the Flux was strongly correlated with estimate of V_D (R^2=0.84 for HF3016 and R^2=0.91 for HF3177) as shown in Figure 5.1 and consistent with earlier finding assessed in U251 glioma model. Moreover, T_2-estimates across the two PDOX models (61.70 ± 1.07 ms and 66.81 ± 1.46 ms, respectively, for HF3016 and HF3177) were significantly greater than that of the 9L glioma. Similarly, the mean T_2 estimate for HF3177 was significantly greater than that of U251 glioma (61.0 ± 0.71) ms, ($p<0.0006$); mean T_2 estimate from HF3016 was greater than the U251N but not statistically significant. All these findings in PDOX lines points to a highly edematous tumor, and a subsequently different physical state of these models compared to standard models in current use. H&E-stained histopathological features exhibiting pseudopalisading necrosis. MHC immunohistochemistry features such as, highly elevated Ki-67 proliferation index (> 20%) and infiltration to adjacent brain parenchyma, including the corpus callosum etc..,

reminiscent of human GBM features, provide strong support to our hypothesis that PDOX tumor models are superior in reproducing the major salient features of human GBMs. The histopathological and MHC features are displayed in Figures 5.3 and 5.4 that provide a complete picture of this part of exploration.

In chapter 6, an intriguing issue related to MRI hardware was presented that has been sparsely reported in publications. MRI signal amplitude decrease resulting from heating of a 4-channel phased-array receiver coil in a 7T small animal imaging magnet during high duty-cycle DCE-MRI is presented. The observed drift in baseline signal (signal intensity prior to the administration of CA) in animal data was found to affect the PK modeling of DCE-data by elevating the scale factor that was used to adjust the arterial input function of CA in blood plasma and led to an unexpected variability in DCE-MRI derived parameters. The decrease in signal amplitude was modeled using a heuristic approach using a 3-parameter equation (Equation [6.1]). A central slice/first-echo was selected and for each time point of the data before CA injection all the data in that image was summed to produce an estimate of the baseline signal, and its drift. The heuristic equation was fitted to that data and normalized to its first point, thus producing a correction across the entire time of the study and for all voxels in the study. That is, the uncorrected signal intensity was divided by the common correction factor noted (refer to equation 6.4 in chapter 6), that led to a consistent, flat baseline (Figure 6.4). A subset of 9L test-retest DCE studies were reanalyzed applying the correction factor generated (note the uncorrected and corrected AIF plot in one of the 9L animal presented in Figure 6.6) , that produced lower variances in both the scale factor and K^{trans} estimates compared to uncorrected drift data (see the Supplementary Material Table S4).

Third, this study measured TIFP using the WIN technique in treatment naïve and in irradiated 9L gliosarcoma cerebral tumors in rats. The signatures of acute treatment response were investigated using dynamic contrast-enhanced MRI (DCE-MRI). Such tumor microvascular parameters K^{trans}, v_e, and microenvironmental parameters - peritumoral V_D and Flux, were assessed in these cohorts in paired experiments 24 hours apart, with intervening RT in the treatment animals. TIFP and tumor blood flow were significantly reduced ($p<0.05$) post RT in irradiated cohort. DCE-MRI biomarkers showed a decrease post RT; notably Flux and V_D significantly decreased post RT ($p<0.05$) and were strongly correlated indicating a clear signature of radiation response. The regression fits of Flux versus V_D also differed ($p<0.05$) between the two cohorts (Figure 7.2). However, TIFP exhibited only a weak correlation with V_D or Flux in either cohort. A marked reduction in tumor perfusion, together with centrally localized necrosis confirmed by H&E histopathology, was indicative of vascular collapse (Figure 7.6).

DCE-MRI with data-driven approach of model selection technique described in this dissertation provides stable and unbiased estimate of vascular and TME parameters representative of several important aspects of glioma physiology. Since each individual DCE-MRI parameter provides an insight into a distinct physiological pathognomonic of malignancy, an analysis of the spectrum of MRI biomarkers in relation to each other can classify pre and post therapeutic responses. Additionally, the assessment of receiver coil heating-induced signal drift and its adverse effect in DCE-MRI PK modelling, a slightly different context but equally relevant aspect of MRI technology, was addressed, thus identifying and correcting biases that might have leaked into DCE biomarkers, thus allowing their use in assessing their relation to the physical state of cerebral tumors.

8.2 Future directions

The first part of this research work characterized quantitatively the major imaging biomarkers of PDOX gliomas in primary(HF3016) and recurrent glioma (HF3177), backed by strong histopathological findings that showed the tumors to be reminiscent of human GBM. As PDOXs are superior in reproducing the majority of histological features of GBM pathology, these tumors might be used for testing anticancer drugs and radiation therapy to identify signatures of response in pre-clinical models that are more relevant to human studies.

Secondly, radiation therapy had clear signature of response in 9L gliosarcoma tumors as presented in chapter 7, proven by significantly reduced TIFP and DCE-MRI derived biomarkers in the treated group. Significantly different regression fit of peritumoral flux and V_D for the treated group with reduced TIFP suggests possibility of covariance between the TIFP and V_D or Flux, but no strong correlation was found. These DCE-MRI derived Flux and V_D and the measured TIFP in 9L tumors, are being used for computational modelling to study the interplay between the solid and fluid phase of the tumor and its surrounding by our collaborators at University of Florida led by Dr. Sarntinoranont and her team. This will help in getting a more comprehensive picture of glioma physiology.

Third, as noted in chapter 6, the 3-parameter exponential heuristic fit of observed signal drift loses some accuracy, especially towards the latter portion of DCE washout profile. A 4-parameter quadratic fit would improve the accuracy but the 3-parameter DCE model selection approach should also be revised for a 4-parameter summary which is out of scope of this dissertation but is a subject for future research.

Supplementary Material

A. Discussion

FG136: Search for a source of systematic error

FG136 was an athymic rat received on January 12, 2021. Weight at receipt was 200g; at sacrifice on April 23, 2021, it was ~225g. HF3177 cell line implantation (sans Matrigel) took place on Feb 4, 2021. Imaging took place on April 20, 2021. Post-contrast T_1- and T_2-weighted imaging revealed a very large tumor (9.5 mm height, 7.4 mm width) that, at its center, occupied nearly a third of the cross-sectional area of the brain at this section, not including the infiltrating portion and effects of edema (Figure S5) centerline shift, compression of fluid spaces and the contralateral hemisphere is evident. The post-mortem H&E-stained sections of Figure S6 demonstrate a lack of post-mortem tissue integrity, which in turn implies extensive necrosis and an elevated interstitial volume.

The early delivery of contrast agent to this large tumor (Figure S7, Center) reveals a ring-enhancing lesion. The difference between the pre-injection and post-injection tissue contrast 19 seconds later (Figure S7, Right) demonstrates that the major delivery of contrast (and therefore perfusion) takes place at the tumor rim and strongly suggests that the central portions of this tumor were under-perfused, with large areas of necrosis. H&E staining of post-mortem tissue (Figure S6 Center & Right), with extensive tearing in the region of the tumor, supports this view

Model limitations, model failures

The model applied to DCE-MRI data is usually that of the Standard Model:

$$C_t(t) = K^{trans} \int_0^t C_p(\tau) e^{-k_{ep}(t-\tau)} d\tau + v_p C_p(t) \quad \textbf{1}$$

In this approach, it assumed that the time trace of arterial CA concentration, i.e the arterial input function can be measured, and that the compartmental model can be applied to the data on a voxel-by-voxel basis.

In the case of FG136, the overall fit of the model to the data was very good, with an R^2 of ~0.99 (Figure S8). However, the parametric estimates of this excellent fit were non-physiological, and in some voxels, non-physical. That is, the estimate of the extracellular, extravascular volume fraction, v_e approached or sometimes exceeded 1.0; essentially all of the tissue was described by this model as vacuolated, despite a clear uptake of CA in the tissue.

The tissue concentration of CA is taken to be proportional to the temporal change in the relaxation rate, $\Delta R_1(t)$. In our practice, we define a region of interest in the normal caudate putamen where it is known that no extravasation of CA occurs and the plasma volume is approximately 1% of the tissue volume[83]. We assume that the relaxivity of CA in this scenario is that of tissue [2,5], and that the scaling factor between $\Delta R_1(t)$ and CA concentration in both blood and tissue is the same. In this case, $C_t(t) = a\Delta R_{1t}(t)$ and $C_p(t) = b\Delta R_{1p}(t)$, where a = b. Suppose a and b are not equal. Let $\kappa = \frac{b}{a}$; equation [1] is then stated as

$$\Delta R_{1t}(t) = \kappa \left[K^{trans} \int_0^t \Delta R_{1p}(\tau) e^{-k_{ep}(t-\tau)} d\tau + v_p \Delta R_{1p} \right] \quad \textbf{2}$$

It should be clear from this that a scaling error in the estimate of the AIF affects the estimate of K^{trans} and v_p linearly. That is, because $\Delta R_{1t}(t)$ is a measured quantity, an

error by a factor of two (e.g.) in κ will cause an inverse error by a factor of two in both and K^{trans} and v_p.

In practice, because the high concentration of contrast agent in blood attenuates the early signal due to T_2* dephasing, even in a dual-gradient echo experiment a direct measure of $\Delta R_{1p}(t)$ in the early portion of the AIF is usually unavailable[2]. Our approach, in line with that of others, is to employ a group-averaged input function[82]. The group-averaged function is aligned to the start of CA administration and scaled by integrating the latter half of the tissue concentration curve of the caudate putamen and the corresponding half of the group-averaged function, assuming that the plasma volume, the only tissue that contains CA, is 1% of the total tissue volume.

The group-averaged AIF and time trace of $\Delta R_1(t)$ in the caudate putamen of FG136 is shown in Figure S9. After the third image acquisition, it appears that the trace of $R_1(t)$ approaches saturation, providing a baseline from which $\Delta R_1(t)$ can be calculated upon delivery of CA. However, the signal itself approaches baseline in the second half of the time trace, thus requiring a relatively high scaling factor – in this case ~700, where the average scaling factors in the group average ~200. This points to a systematic error in the trace of $\Delta R_1(t)$. Therefore, estimates of K^{trans} and v_p, but not k_{ep}, could be biased a factor ~3.5. The estimate of v_e, since it depends on the relationship $v_e = \frac{K^{trans}}{k_{ep}}$, should also be biased by the same factor. Estimates of Flux and V_D in the mostly normal rim of the tumor are also affected by this scaling factor. In FG136, the mean of the estimates of V_D, v_p, K^{trans}, k_{ep}, and v_e were 0.812, 0.0271, 0.129, 0.156, 0.916, respectively. (Note that, because v_e is calculated as a ratio, its value is not equal to

the ratio of means of K^{trans} divided by k_{ep}.) If the parametric estimates were corrected by a factor of 3.5, their values would lie well within the confidence limits of the group means for HF3177 tumors. It seems highly probable that the plasma volume in the caudate putamen was underestimated.

A consideration of sources of this apparent underestimate of plasma volume in the caudate putamen identifies two possibilities. First, it is assumed that the baseline estimate of $R_1(t)$ is correct and does not vary. Second, it is assumed that the plasma volume in the caudate putamen is 1% of the tissue volume.

Reports of thermal drift in receiver gain[19,20] prompted a thorough investigation of our four-element surface coil with active elements (Model No 1P T11483V3, Serial No S 0104). Phantom studies confirmed that thermal drift did occur in the DCE-MRI protocol, but that its occurrence in animal studies might vary from study to study, depending on thermal contact with the animal, and on the on/off state of the air stream used for maintaining animal temperature (a complete report of this work is in preparation for publication). If receiver gain is constant, true noise amplitude in the system can be expected to remain constant. If points of true noise can be identified by point-by-point examination of phase stability, changes in receiver gain can then be followed via estimates of change in noise amplitude. In FG136 we found evidence for a minimal change in noise amplitude across the time of the experiment (Figure S10).

The assumption that plasma volume in the caudate putamen is 1% of the tissue volume in this animal may be wrong. The expanding mass of the tumor in the confines of the animal's skull certainly compresses and displaces the remaining normal tissue and diminishes its capacitance spaces. We do not presently have an objective measure of

vascular space in this animal, other than the DCE-MRI study, so this remains a matter of conjecture, but it appears that the most likely explanation for the apparent underestimation of the caudate putamen's vascular volume fraction is compression of its vasculature by the tumor in the contralateral hemisphere.

Vascular parameter estimates in model 2 region

The SM parameter estimates from model 3 tumor region were presented in the main text. Shown below (Figure S12) is an example of model 2 (original two-parameter Patlak[17,18]) fit from one of the animals used in the study, PS73. K^{trans} and v_p are the two parameters estimated from model 2 region; these are presented in table S3. The parameters from model 2 regions, which lay uniformly outside the tumor's model 3 region, were about an order of magnitude lower than that from model 3 tumor region. The region of interest chosen was the extended outer rim of the tumor (model 2 region, Figure S11), which is primarily the normal tissue. The fit is approximately linear in the later portion of the curve, but there is time lag initially subtly undershooting the origin, leading to negative plasma volume estimate which is indicative of model failure. This indicates contrast agent is leaking to model 2 region from adjacent voxels of model 3 tumor but is not being re-absorbed by the source which clearly violates the conservation of mass, a model failure of standard pharmacokinetic modelling.

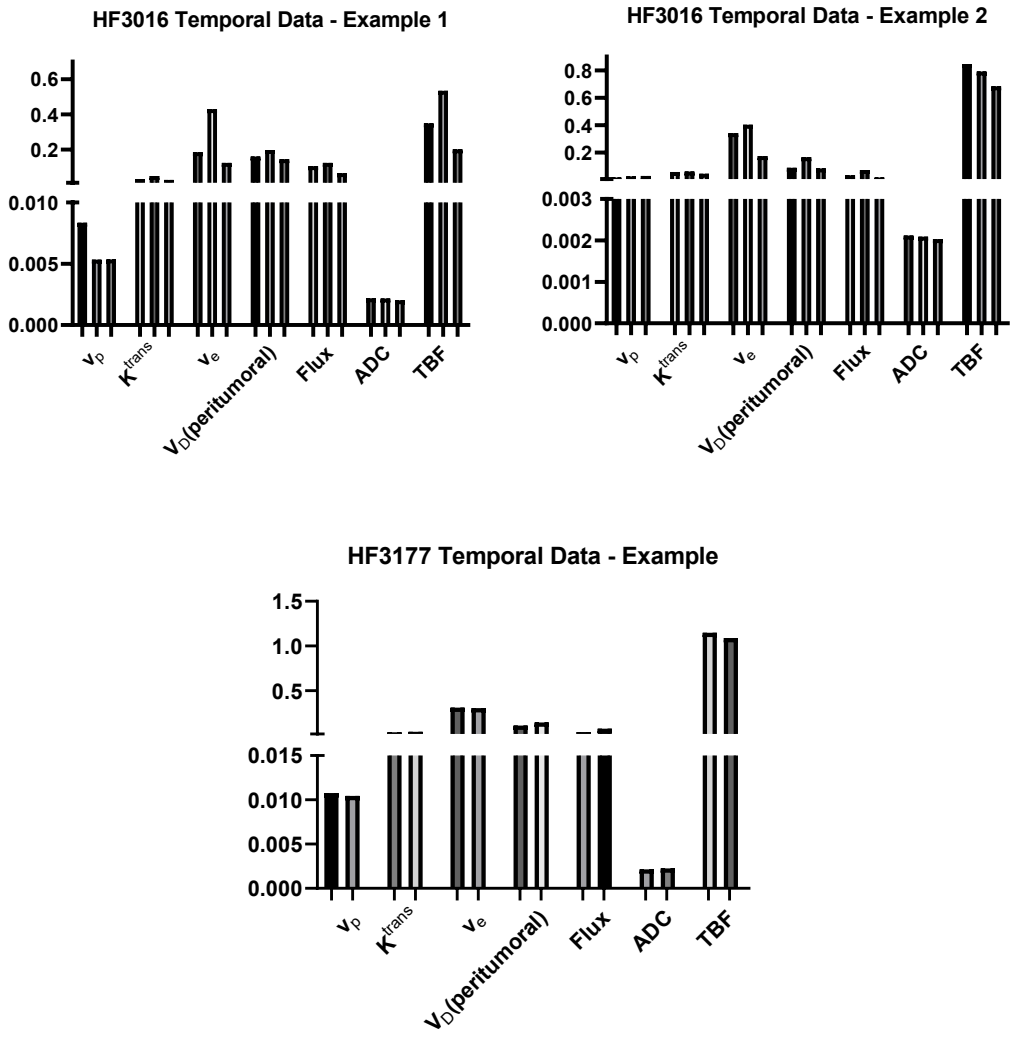

Figure S1: Longitudinal imaging follow-up data from three rats. Two with HF3016 and one with HF3177 glioma were imaged at multiple time points after implantation. The HF3016 were imaged at 4th 5th, and 7th weeks and HF3177 at 8th and 11th weeks. Once established the vascular kinetics did not seem to change appreciably over this duration. Units: K^{trans} : mL/min-mL, Flux: $\mu m^3/\mu m^2$sec sec, ADC: mm^2/sec, TBF: $mL/gm - min$, the rest are unitless.

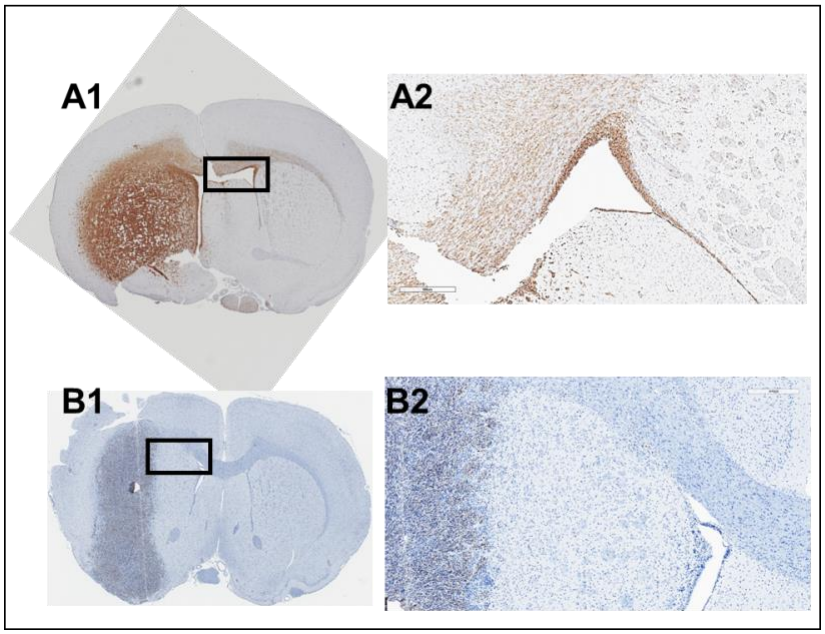

Figure S2: Examples of tumor infiltration from MHC-stained brain sections. A1, A2 are from HF3016 cell line and B1, B2 are from HF3177 cell line. A2 and B2 are magnified images of rectangles indicated in A1 and B1. HF3016 exhibited more infiltration along the white matter tract (A2) compared to HF3177 (B2). This observation was contrary to the expected increased infiltration for the recurrent HF3177 tumor in comparison to its primary counterpart, HF3016.

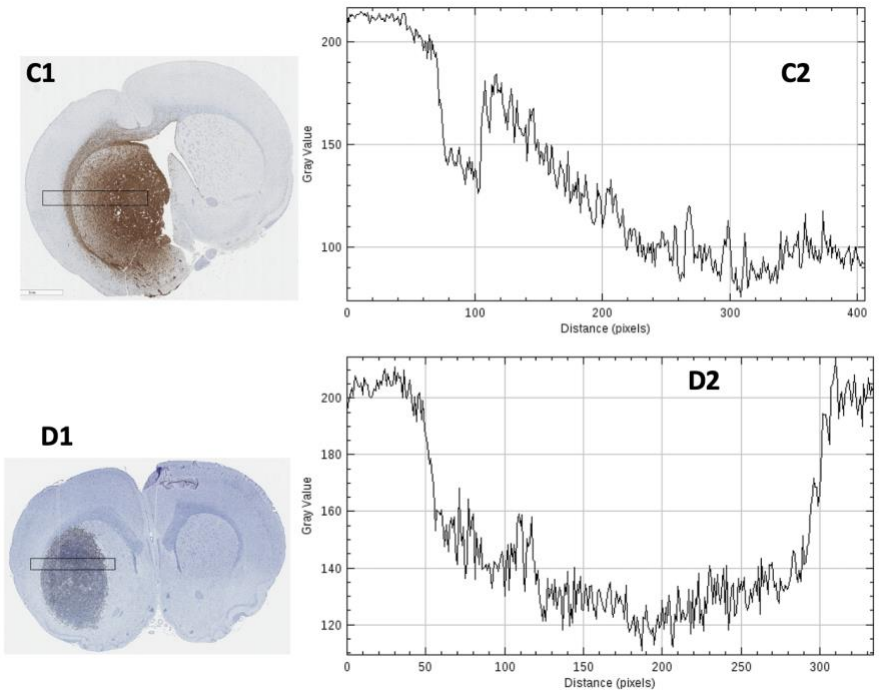

Figure S3: Tumor and normal tissue profile from MHC-stained brain sections. C1 is the MHC image from HF3016 and C2 is the corresponding tissue profile from the rectangular selection on C1. The profile starts with high greyscale values in normal tissue area, declines sharply at the tumor-normal tissue interface indicating significant amount of infiltrative tumor cells, a decent rise again around the peritumoral area indicating the presence of fair amount of normal tissue, and a continuous decline thereafter which is mainly the tumor. Note that there are several prominent spikes in the later part of the profile which are indicative of pseudopalisading necrosis in the tumor. The bottom panel is the MHC image (D1) from HF3177 showing a little different profile (D2) than HF3016 with less diffused cells compared to HF3016. Hence, there is sharp decline initially and similar rise around the peritumoral area while exiting the tumor with evidence of pseudopalisading necrosis in between.

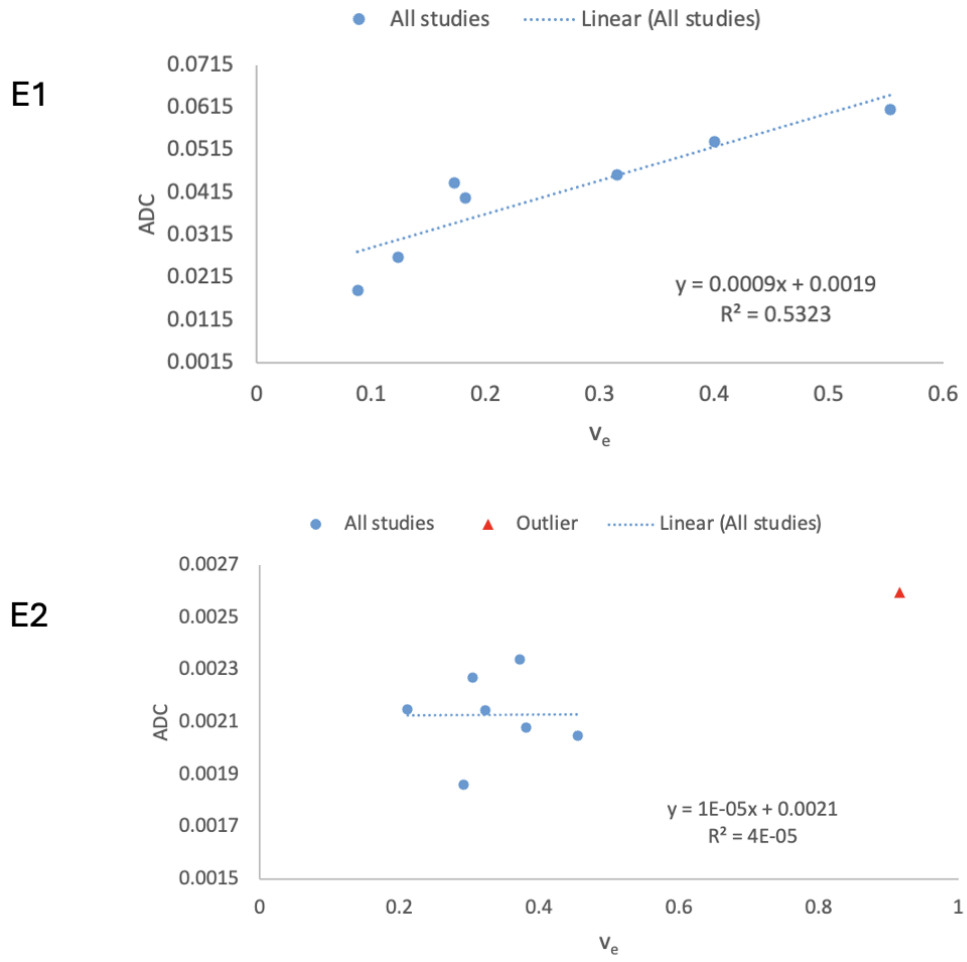

Figure S4: Scatter plot of v_e (x-axis) vs tumor ADC (y-axis) values in (E1) HF3016, (E2) HF3177. A moderate positive correlation was observed between these parameters for HF3016 that represent extracellular distribution space measurements. However, no specific trend emerged out for HF3177 (Figure E2). The inclusion of outlier data point in regression fit results in a moderate positive correlation as that in the HF3016 implants.

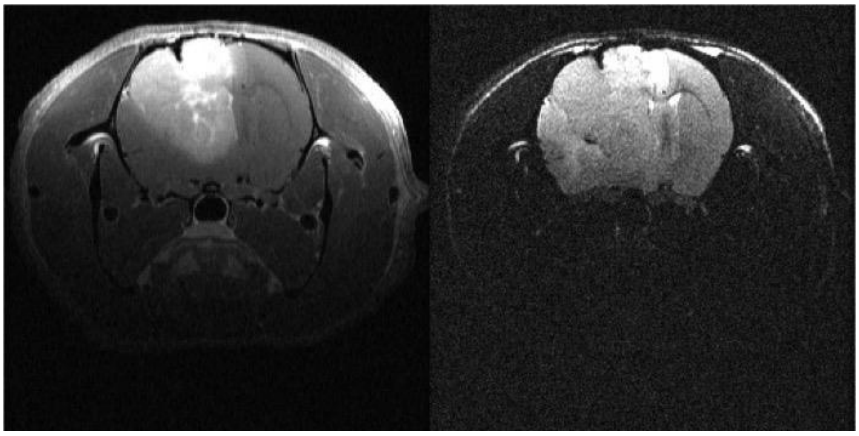

Figure S5: Left: Post-contrast T_1-weighted image approximately after 20 minutes of contrast injection. Right: T_2-weighted map exhibiting edema.

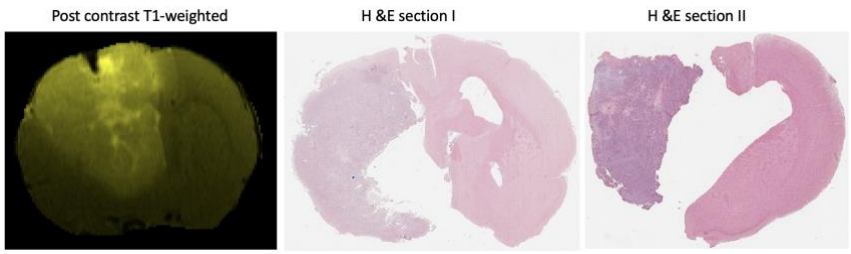

Figure S6: Left: post-contrast T_1-weighted image. Center and Right: two H-&-E histopathology images for FG136, exhibiting highly elevated interstitial volume fraction (v_e).

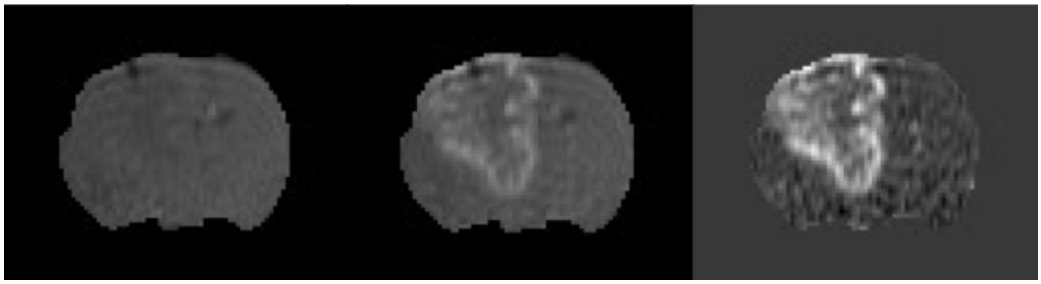

Figure S7: Left: pre-contrast T_1-weighted image. Center: Post-contrast T_1-weighted image. Right: Subtraction (post minus pre) image acquired 19 seconds after contrast injection exhibited ring enhancement and central perfusion deficit.

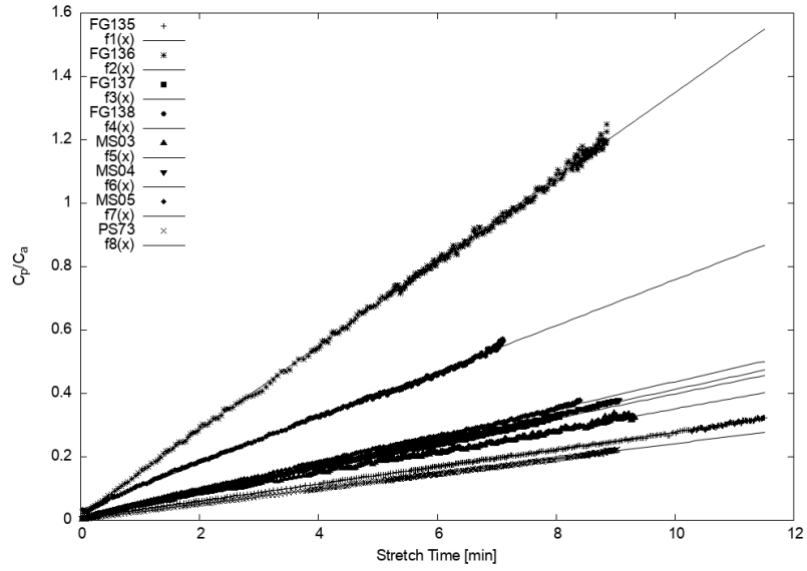

Figure S8: Graphs of goodness of fit of applied standard model in model 3 tumor in HF3177 group. The average R^2 was > 0.99 .

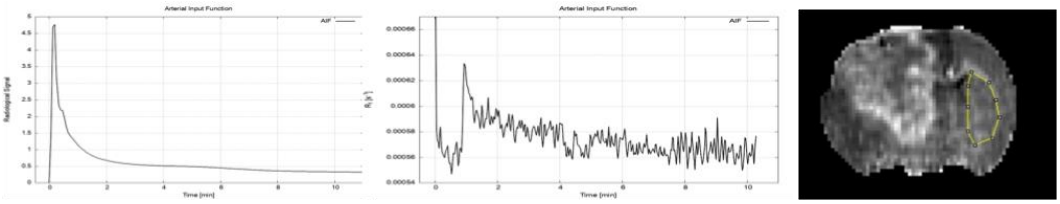

Figure S9: Left: The group-averaged AIF estimate of change in contrast agent concentration (Radiological signal on Y-axis, Time in minutes on X-axis) taken from our earlier stuies[2,3,4]. Center: R1(t) profile (R1 on Y-axis and Time in minutes on X-axis) in this particular study, FG136. Right: Example of region of interest selection in contralateral normal brain caudate putamen.

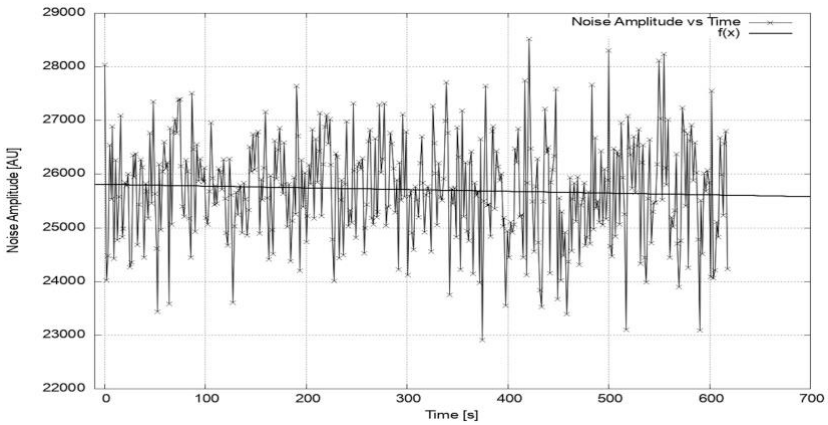

Figure: S10: Behavior of mean noise amplitude during the entire DCE-MRI session across all four coils for the animal FG136.

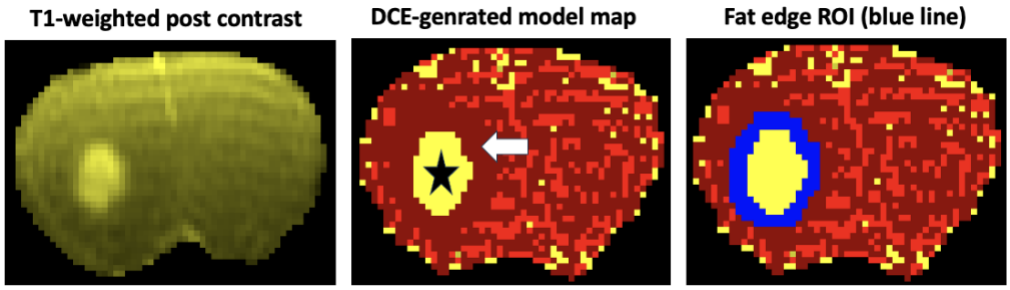

Figure S11: Left: T_1-weighted post-contrast image. Middle: DCE-MRI-generated model map. The yellow model 3 tumor is indicated by a black star in the center, the dark red area around the model 3 tumor (indicated by white block arrow) is the model 2 region. Right: ROI chosen on model 2 region (note the blue thick ring around model 3 tumor) for generating summary parameters, v_p and K^{trans}.

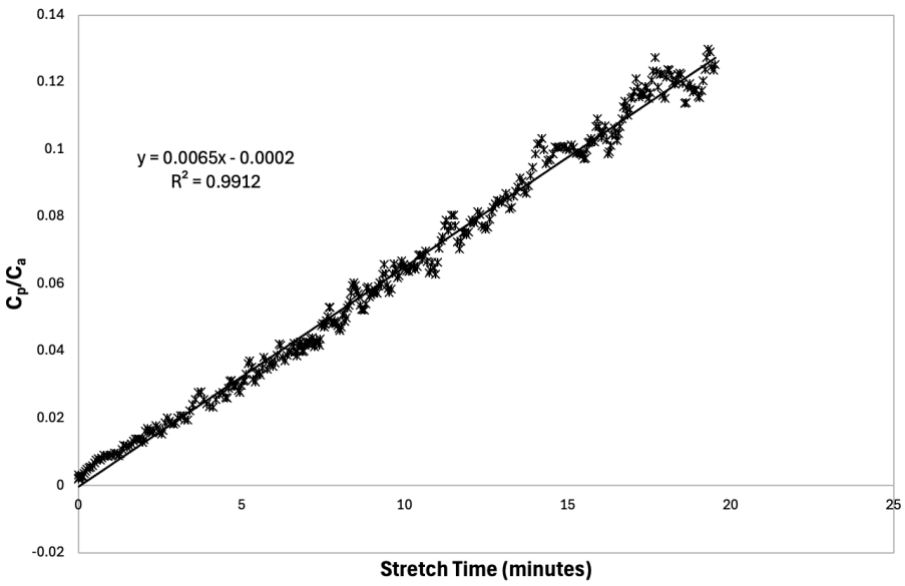

Figure S12: Patlak plot in model 2 region. Note the convexity of the curve in the beginning of the curve, mostly linear otherwise, signaling model failure.

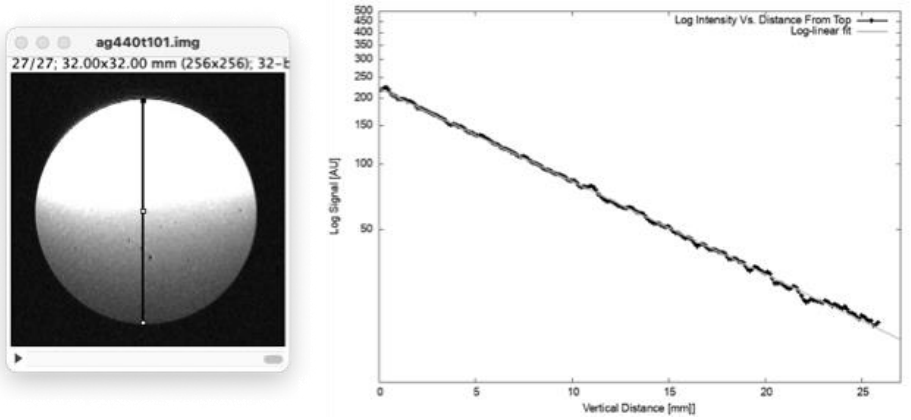

Figure S13: Left: Slice of a gel phantom (T_1-weighted). Right: log plot of intensity in the vertical line drawn on the phantom. It demonstrates the very desirable property in Coil 1 of log-linearity in a vertical trace of a large phantom. Horizontal uniformity is also excellent, and the vertical log-linearity persists across the width of the phantom: all vertical lines show approximately the same log-linear slope.

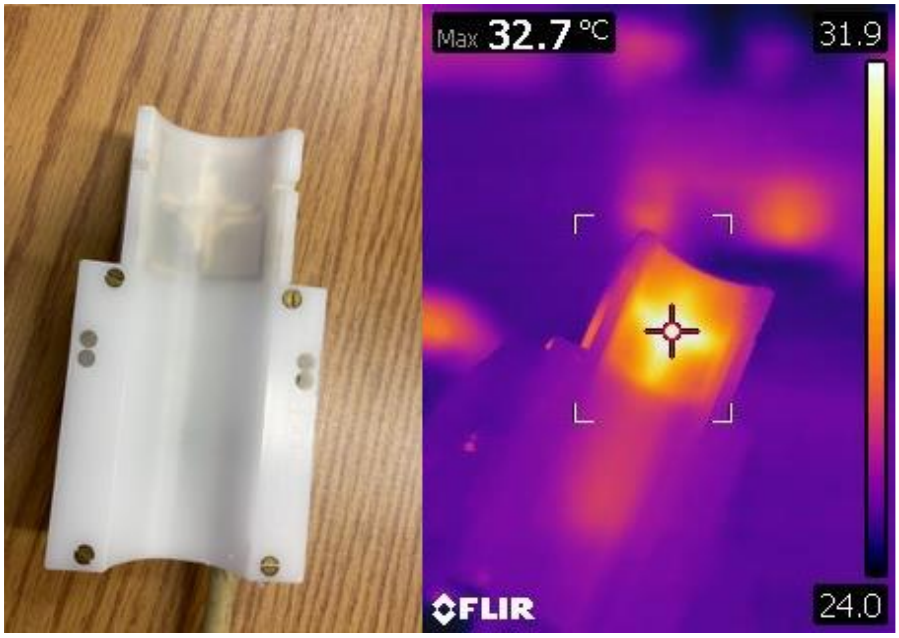

Figure S14: Left: a photo of the underside of Coil 1. Right: a thermal image produced at Bruker laboratories of this model coil after 5 minutes of continuous operation of active decoupling. Thermal effects propagate throughout the coil.

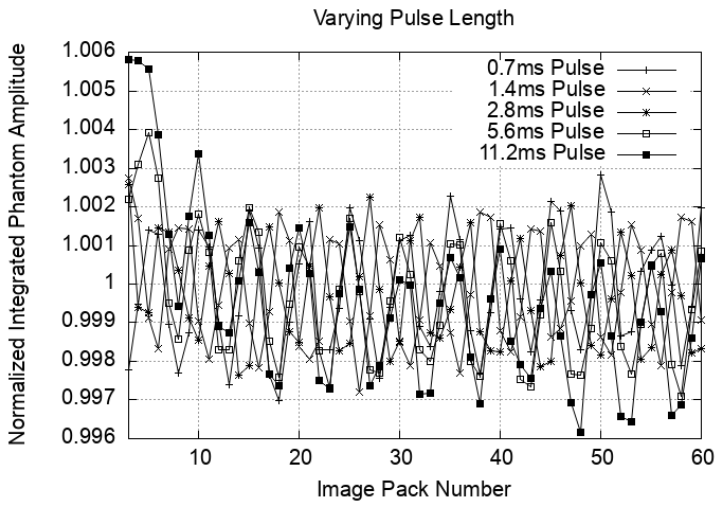

Figure S15: Coil 1 with lowered current- limiting resistor in the PIN diode circuit. It demonstrates that lowering the resistor value in the active decoupling circuit of Coil 1 essentially removes the receiver signal amplitude drift. Stimulated echoes persist.

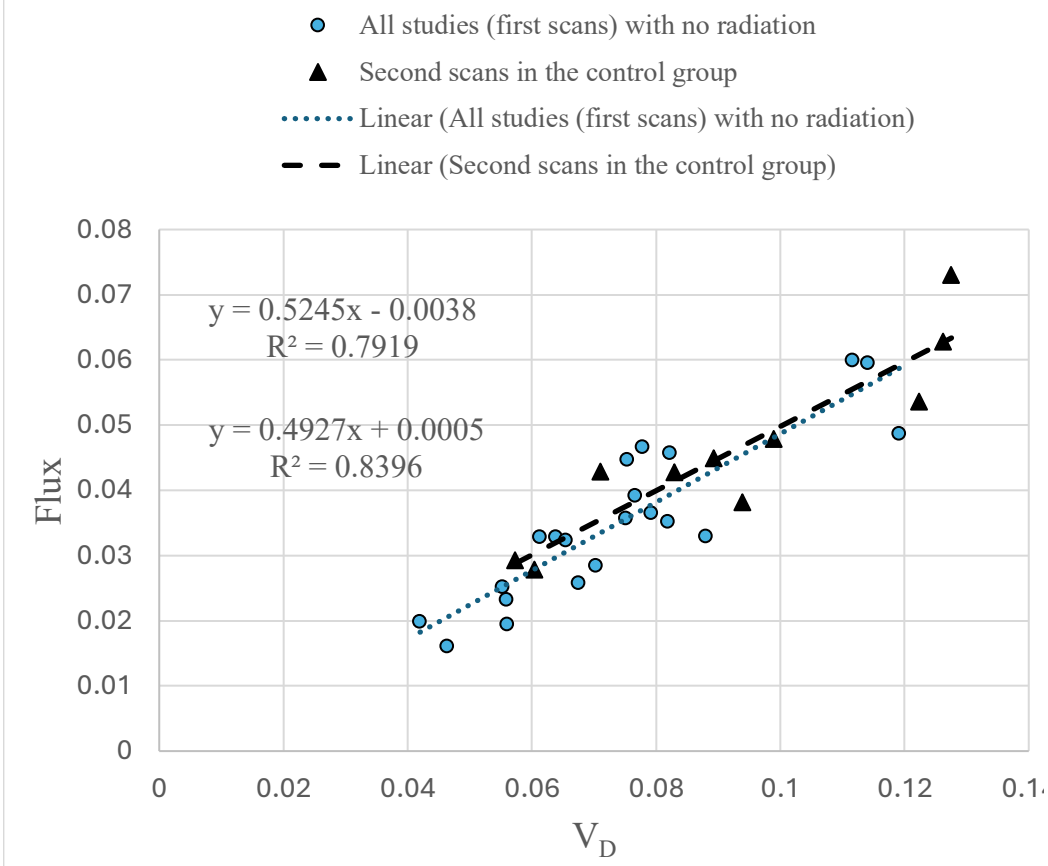

Figure S16: Graphs of Flux versus distribution volume at tumor rim. The circles are the data points of first MRI scan (24-hour pre scan) of all the animals from both groups (irradiated and controls). The triangles are the data points from the second MRI scan in the control population receiving no radiation. It is evident that the slopes (0.52 for all studies, 0.49 for second studies in the control. Group) and the R^2 values 0.8 are almost identical for both cases.

Cell line	Mean ± SEM
HF3016 (n=7)	1.13 ± 0.05
HF3177 (n=7)	1.10 ± 0.04

Table S1: Mean and SEM of 'tumor to normal brain' ratios for ADC values.

Studies (HF3016)	PS26	PS27	PS28	PS29	PS32	PS35	PS63
R^2	0.9925	0.9725	0.9203	0.9847	0.9755	0.9944	0.9981
Studies (HF3177)	FG135	FG137	FG138	PS73	MS03	MS04	MS05
R^2	0.9994	0.9981	0.9973	0.9968	0.9993	0.9988	0.9993

Table S2: Goodness of fit in Model 3 tumor for all PDOX studies

HF3016

Parameter	Mean ($x10^{-3}$)	Variance ($x10^{-5}$)	Skewness ($x10^{-1}$)	Kurtosis
v_p	7.52 (±3.88)	16.80 (±9.65)	7.52 (±4.58)	3.12 (±2.45)
K^{trans}	4.80 (±1.87)	5.08 (±3.96)	20.82 (±7.87)	8.04 (±6.42)

HF3177

Parameter	Mean ($x10^{-3}$)	Variance ($x10^{-3}$)	Skewness ($x10^{-1}$)	Kurtosis ($x10^{-1}$)
v_p	7.35 (±3.22)	1.97 (±1.80)	28.57 (±16.27)	59.88 (±25.22)
K^{trans}	5.65 (±0.72)	15.8 (±2.92) $x10^{-3}$	6.48 (±1.65)	9.20 (±3.38)

Table S3: Vascular parameter estimates (Mean ± SEM) from model 2 region for two tumor lines; the parameters reported have the same units as mentioned in Table 5.1 summary in the main text.

	Uncorrected				Corrected			
Studies	SF		K^{trans}		SF		K^{trans}	
	Test	Retest	Test	Retest	Test	Retest	Test	Retest
FL201	189.0	178.2	3.47E-02	3.64E-02	68.1	85.7	1.55E-02	1.80E-02
FL212	124.8	223.6	4.57E-02	8.30E-02	77.3	104.2	3.55E-02	3.96E-02
FL213	124.8	232.9	7.32E-02	3.04E-02	62.7	108.0	3.27E-02	1.43E-02
FL214	154.8	119.7	1.02E-01	3.37E-02	78.0	78.1	7.06E-02	7.37E-02
FL226	123.5	251.8	3.35E-02	2.34E-01	77.6	99.7	4.18E-02	1.15E-01
FL227	116.4	113.3	9.92E-02	7.68E-02	77.6	68.0	8.60E-02	4.58E-02
FL232	83.9	92.0	1.43E-02	3.68E-02	64.3	62.7	1.23E-02	2.12E-02
FL233	75.8	100.8	1.38E-01	1.44E-01	54.9	66.5	7.17E-02	9.50E-02
Mean	124.2	164.0	6.77E-02	8.44E-02	70.1	84.1	4.57E-02	5.29E-02
SD	36.2	65.4	4.28E-02	7.18E-02	8.9	18.1	2.73E-02	3.79E-02
SEM	12.8	23.1	1.51E-02	2.54E-02	3.1	6.4	9.67E-03	1.34E-02

Table S4: It provides the scale factor (SF) and K^{trans} summary in a subset of 9L studies analyzed before and after applying correction. The mean SF and K^{trans} are more consistent between the test-retest studies with noticeably lower variance for the corrected studies.

APPENDIX A

COPYRIGHT LETTERS OF PERMISSION TO REPRODUCE

Permission to reproduce Figure 3.1, Chapter 3

Dear Prabhu,

Thank you for contacting CCC regarding order **6100820187696**. We provide rights licensing on behalf of publishers who list their works with us. My name is Pedro and I will be happy to assist you.

First of all, I hope this e-mail finds you well. Now, regarding your inquiry, the confirmation e-mail you received at the time of your purchase is to confirm that you have successfully purchased permission to reuse the requested content at no cost. You may proceed to use this content in the ways specified when purchasing your license. For your convenience, I have attached a copy of license **6100820187696** to this e-mail, which you can also print from your 'My Orders' page **here**, and in the email.

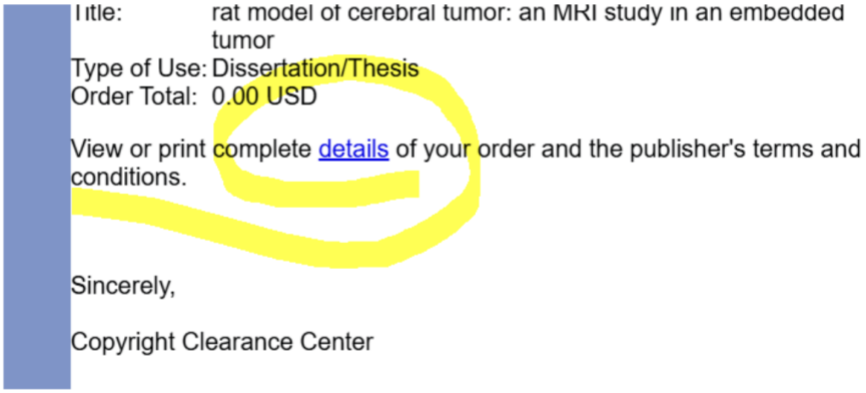
Title: rat model of cerebral tumor: an MRI study in an embedded tumor
Type of Use: Dissertation/Thesis
Order Total: 0.00 USD

View or print complete details of your order and the publisher's terms and conditions.

Sincerely,

Copyright Clearance Center

I hope this information was helpful. If you have any further questions, please don't hesitate to reply to this e-mail, or contact a Customer Account Specialist at +1-855-239-3415. Have a nice weekend!

Kind regards,
Pedro

Permission to reproduce Chapter 5 in its entirety.

JOHN WILEY AND SONS LICENSE
TERMS AND CONDITIONS

Oct 02, 2025

This Agreement between Prabhu C. Acharya ("You") and John Wiley and Sons ("John Wiley and Sons") consists of your license details and the terms and conditions provided by John Wiley and Sons and Copyright Clearance Center.

License Number	6112820307716
License date	Sep 19, 2025
Licensed Content Publisher	John Wiley and Sons
Licensed Content Publication	NMR in Biomedicine
Licensed Content Title	DCE-MRI Tumor Vascular Parameters in Two Preclinical Patient-Derived Orthotopic Xenograft Models of Glioblastoma
Licensed Content Author	Prabhu C. Acharya, Tavarekere N. Nagaraja, Stephen L. Brown, et al
Licensed Content Date	Jul 9, 2025
Licensed Content Volume	38
Licensed Content Issue	8

APPENDIX B

RESEARCH ACTIVITY APPROVAL FOR ANIMAL SUBJECTS

Re: IACUC No. **00001546** titled **MRI Signatures Of Response To High-Dose Radiotherapy In Rat Models Of Cerebral Tumor**

Period of IACUC Approval: **05/09/2024** through **05/09/2027**

Dear Dr. Ewing, James:

Thank you for submitting an application for review by the Institutional Animal Care and Use Committee. The application was presented at a convened meeting. A revised application responding to IACUC concerns was reviewed and all concerns were adequately addressed.

The expiration date for this study is 05/09/2027. In order to remain compliant with federal regulations, a new protocol application must be submitted to the IACUC office prior to expiration if you intend to proceed with this line of work beyond the above indicated expiration date. A Final Report must be submitted at the completion of the 3-year approval period or upon early termination of the project.

Any adverse effects on animals must be reported to the IACUC as soon as possible.

Please feel free to contact The IACUC Coordinator at 874-4360 if you have any questions regarding this matter.

Re: IACUC No. **00001548** titled **A PATIENT-DERIVED XENOGRAFT OF CEREBRAL GLIOMA WITH GENETIC AND RADIOLOGIC FIDELITY**

Period of IACUC Approval: **05/08/2024** through **05/08/2027**

Dear Dr. Ewing, James:

Thank you for submitting an application for review by the Institutional Animal Care and Use Committee. The application was presented at a convened meeting. A revised application responding to IACUC concerns was reviewed and all concerns were adequately addressed.

The expiration date for this study is 05/08/2027. In order to remain compliant with federal regulations, a new protocol application must be submitted to the IACUC office prior to expiration if you intend to proceed with this line of work beyond the above indicated expiration date. A Final Report must be submitted at the completion of the 3-year approval period or upon early termination of the project.

Any adverse effects on animals must be reported to the IACUC as soon as possible.

Please feel free to contact The IACUC Coordinator at 874-4360 if you have any questions regarding this matter.

REFERENCES

1. Ewing JR, Nagaraja TN, Aryal MP, et al. Peritumoral tissue compression is predictive of exudate flux in a rat model of cerebral tumor: an MRI study in an embedded tumor. *NMR Biomed.* 2015;28(11):1557-1569.
2. Ewing JR, Bagher-Ebadian H. Model selection in measures of vascular parameters using dynamic contrast-enhanced MRI: experimental and clinical applications. *NMR Biomed.* 2013;26(8):1028-1041.
3. Padhani AR. Dynamic contrast-enhanced MRI in clinical oncology: current status and future directions. *J Magn Reson Imaging.* 2002;16(4):407-422.
4. Sourbron SP, Buckley DL. Classic models for dynamic contrast-enhanced MRI. *NMR Biomed.* 2013;26(8):1004-1027.
5. Bagher-Ebadian H, Jain R, Nejad-Davarani SP, et al. Model selection for DCE-T1 studies in glioblastoma. *Magn Reson Med.* 2012;68(1):241-251.
6. Schabel MC, Parker DL. Uncertainty and bias in contrast concentration measurements using spoiled gradient echo pulse sequences. *Phys Med Biol.* 2008;53(9):2345-2373.
7. Subashi E, Choudhury KR, Johnson GA. An analysis of the uncertainty and bias in DCE-MRI measurements using the spoiled gradient-recalled echo pulse sequence. *Med Phys.* 2014;41(3):032301.
8. Gillies RJ, Bhujwalla ZM, Evelhoch J, et al. Applications of magnetic resonance in model systems: tumor biology and physiology. *Neoplasia.* 2000;2(1-2):139-151.
9. Evelhoch JL, Gillies RJ, Karczmar GS, et al. Applications of magnetic resonance in model systems: cancer therapeutics. *Neoplasia.* 2000;2(1-2):152-165.
10. Kang TW, Kim ST, Byun HS, et al. Morphological and functional MRI, MRS, perfusion and diffusion changes after radiosurgery of brain metastasis. *Eur J Radiol.* 2009;72(3):370-380.
11. Boxerman JL, Schmainda KM, Weisskoff RM. Relative cerebral blood volume maps corrected for contrast agent extravasation significantly correlate with glioma tumor grade, whereas uncorrected maps do not. *AJNR Am J Neuroradiol.* 2006;27(4):859-867.
12. Daldrup H, Shames DM, Wendland M, et al. Correlation of dynamic contrast-enhanced MR imaging with histologic tumor grade: comparison of macromolecular and small-molecular contrast media. *AJR Am J Roentgenol.* 1998;171(4):941-949.
13. Brown SL, Nagaraja TN, Aryal MP, et al. MRI-Tracked Tumor Vascular Changes in the Hours after Single-Fraction Irradiation. *Radiat Res.* 2015;183(6):713-721.
14. Sanvito F, Kaufmann TJ, Cloughesy TF, Wen PY, Ellingson BM. Standardized brain tumor imaging protocols for clinical trials: current recommendations and tips for integration. *Front Radiol.* 2023;3:1267615.
15. Tofts PS, Brix G, Buckley DL, et al. Estimating kinetic parameters from dynamic contrast-enhanced T(1)-weighted MRI of a diffusable tracer: standardized quantities and symbols. *J Magn Reson Imaging.* 1999;10(3):223-232.

16. Tofts PS. Modeling tracer kinetics in dynamic Gd-DTPA MR imaging. *J Magn Reson Imaging.* 1997;7(1):91-101.
17. Patlak CS, Blasberg RG. Graphical evaluation of blood-to-brain transfer constants from multiple-time uptake data. Generalizations. *J Cereb Blood Flow Metab.* 1985;5(4):584-590.
18. Patlak CS, Blasberg RG, Fenstermacher JD. Graphical evaluation of blood-to-brain transfer constants from multiple-time uptake data. *J Cereb Blood Flow Metab.* 1983;3(1):1-7.
19. Collins DJ, Germuska M, d'Arcy JA, et al. 3D sequences used for DCE-MRI can exhibit initial instabilities that will affect T1 quantification. Abstract presented at Magn Reson Med.; 2009.
20. Vos SB, Tax CM, Luijten PR, Ourselin S, Leemans A, Froeling M. The importance of correcting for signal drift in diffusion MRI. *Magn Reson Med.* 2017;77(1):285-299.
21. Aghaeifar A, Bosch D, Heule R, et al. Intra-scan RF power amplifier drift correction. *Magn Reson Med.* 2024;92(2):645-659.
22. Johnson DR, O'Neill BP. Glioblastoma survival in the United States before and during the temozolomide era. *J Neurooncol.* 2012;107(2):359-364.
23. Hicks WH, Bird CE, Traylor JI, et al. Contemporary Mouse Models in Glioma Research. *Cells.* 2021;10(3).
24. Omuro A, DeAngelis LM. Glioblastoma and other malignant gliomas: a clinical review. *JAMA.* 2013;310(17):1842-1850.
25. Jain RK, di Tomaso E, Duda DG, Loeffler JS, Sorensen AG, Batchelor TT. Angiogenesis in brain tumours. *Nat Rev Neurosci.* 2007;8(8):610-622.
26. Baxter LT, Jain RK. Transport of fluid and macromolecules in tumors. I. Role of interstitial pressure and convection. *Microvasc Res.* 1989;37(1):77-104.
27. Stupp R, Mason WP, van den Bent MJ, et al. Radiotherapy plus concomitant and adjuvant temozolomide for glioblastoma. *N Engl J Med.* 2005;352(10):987-996.
28. Price M, Ballard C, Benedetti J, et al. CBTRUS Statistical Report: Primary Brain and Other Central Nervous System Tumors Diagnosed in the United States in 2017-2021. *Neuro Oncol.* 2024;26(Supplement_6):vi1-vi85.
29. Stupp R, Hegi ME, Mason WP, et al. Effects of radiotherapy with concomitant and adjuvant temozolomide versus radiotherapy alone on survival in glioblastoma in a randomised phase III study: 5-year analysis of the EORTC-NCIC trial. *The Lancet Oncology.* 2009;10(5):459-466.
30. Stupp R, Mason WP, van den Bent MJ, et al. European Organisation for Research and Treatment of Cancer Brain Tumor and Radiotherapy Groups, National Cancer Institute of Canada Clinical Trials Group. Radiotherapy plus concomitant and adjuvant temozolomide for glioblastoma. *N Engl J Med.* 2005;352:987–996.
31. Aldape K, Brindle KM, Chesler L, et al. Challenges to curing primary brain tumours. *Nat Rev Clin Oncol.* 2019;16(8):509-520.
32. Candolfi M, Curtin JF, Nichols WS, et al. Intracranial glioblastoma models in preclinical neuro-oncology: neuropathological characterization and tumor progression. *J Neurooncol.* 2007;85(2):133-148.

33. Gao H, Korn JM, Ferretti S, et al. High-throughput screening using patient-derived tumor xenografts to predict clinical trial drug response. *Nat Med.* 2015;21(11):1318-1325.
34. Huszthy PC, Daphu I, Niclou SP, et al. In vivo models of primary brain tumors: pitfalls and perspectives. *Neuro Oncol.* 2012;14(8):979-993.
35. Irtenkauf SM, Sobiechowski S, Hasselbach LA, et al. Optimization of Glioblastoma Mouse Orthotopic Xenograft Models for Translational Research. *Comp Med.* 2017;67(4):300-314.
36. Hidalgo M, Amant F, Biankin AV, et al. Patient-derived xenograft models: an emerging platform for translational cancer research. *Cancer Discov.* 2014;4(9):998-1013.
37. Nagaraja TN, deCarvalho AC, Brown SL, et al. The impact of initial tumor microenvironment on imaging phenotype. *Cancer Treat Res Commun.* 2021;27:100315.
38. Gu A, Li J, Li MY, Liu Y. Patient-derived xenograft model in cancer: establishment and applications. *MedComm (2020).* 2025;6(2):e70059.
39. Ferretti S, Allegrini PR, Becquet MM, McSheehy PM. Tumor interstitial fluid pressure as an early-response marker for anticancer therapeutics. *Neoplasia.* 2009;11(9):874-881.
40. Heldin CH, Rubin K, Pietras K, Ostman A. High interstitial fluid pressure - an obstacle in cancer therapy. *Nat Rev Cancer.* 2004;4(10):806-813.
41. Elmghirbi R, Nagaraja TN, Brown SL, et al. Toward a noninvasive estimate of interstitial fluid Ppressure by dynamic contrast-enhanced magnetic resonance imaging in a rat model of cerebral tumor. *Magn Reson Med.* 2018;00:1-13.
42. Boucher Y, Baxter LT, Jain RK. Interstitial pressure gradients in tissue-isolated and subcutaneous tumors: implications for therapy. *Cancer Res.* 1990;50(15):4478-4484.
43. Munson JM, Shieh AC. Interstitial fluid flow in cancer: implications for disease progression and treatment. *Cancer Manag Res.* 2014;6:317-328.
44. Liu LJ, Brown SL, Ewing JR, Ala BD, Schneider KM, Schlesinger M. Estimation of Tumor Interstitial Fluid Pressure (TIFP) Noninvasively. *PLoS One.* 2016;11(7):e0140892.
45. Boucher Y, Jain RK. Microvascular pressure is the principal driving force for interstitial hypertension in solid tumors: implications for vascular collapse. *Cancer Res.* 1992;52(18):5110-5114.
46. Tong RT, Boucher Y, Kozin SV, Winkler F, Hicklin DJ, Jain RK. Vascular normalization by vascular endothelial growth factor receptor 2 blockade induces a pressure gradient across the vasculature and improves drug penetration in tumors. *Cancer Res.* 2004;64(11):3731-3736.
47. Jain RK. Barriers to drug delivery in solid tumors. *Sci Am.* 1994;271(1):58-65.
48. Jain RK. Transport of molecules in the tumor interstitium: a review. *Cancer Res.* 1987;47(12):3039-3051.
49. Boucher Y, Salehi H, Witwer B, Harsh GRt, Jain RK. Interstitial fluid pressure in intracranial tumours in patients and in rodents. *Br J Cancer.* 1997;75(6):829-836.

50. Baxter LT, Jain RK. Transport of fluid and macromolecules in tumors. II. Role of heterogeneous perfusion and lymphatics. *Microvasc Res.* 1990;40(2):246-263.
51. Barsoumian HB, Sheth RA, Ramapriyan R, et al. Radiation Therapy Modulates Tumor Physical Characteristics to Reduce Intratumoral Pressure and Enhance Intratumoral Drug Delivery and Retention. *Adv Radiat Oncol.* 2023;8(2):101137.
52. Znati CA, Rosenstein M, Boucher Y, Epperly MW, Bloomer WD, Jain RK. Effect of radiation on interstitial fluid pressure and oxygenation in a human tumor xenograft. *Cancer Res.* 1996;56(5):964-968.
53. George ML, Dzik-Jurasz AS, Padhani AR, et al. Non-invasive methods of assessing angiogenesis and their value in predicting response to treatment in colorectal cancer. *Br J Surg.* 2001;88(12):1628-1636.
54. Acharya PC, Nagaraja TN, Brown SL, et al. DCE-MRI Tumor Vascular Parameters in Two Preclinical Patient-Derived Orthotopic Xenograft Models of Glioblastoma. *NMR Biomed.* 2025;38(8):e70089.
55. Logan J, Fowler JS, Volkow ND, et al. Graphical analysis of reversible radioligand binding from time-activity measurements applied to [N-11C-methyl]-(-)-cocaine PET studies in human subjects. *J Cereb Blood Flow Metab.* 1990;10(5):740-747.
56. Logan J. Graphical analysis of PET data applied to reversible and irreversible tracers. *Nucl Med Biol.* 2000;27(7):661-670.
57. Tofts PS, Kermode AG. Measurement of the blood-brain barrier permeability and leakage space using dynamic MR imaging. 1. Fundamental concepts. *Magn Reson Med.* 1991;17(2):357-367.
58. Ewing JR, Brown SL, Lu M, et al. Model selection in magnetic resonance imaging measurements of vascular permeability: Gadomer in a 9L model of rat cerebral tumor. *J Cereb Blood Flow Metab.* 2006;26(3):310-320.
59. Ewing JR, Brown SL, Nagaraja TN, et al. MRI measurement of change in vascular parameters in the 9L rat cerebral tumor after dexamethasone administration. *J Magn Reson Imaging.* 2008;27(6):1430-1438.
60. Aryal MP, Nagaraja TN, Keenan KA, et al. Dynamic contrast enhanced MRI parameters and tumor cellularity in a rat model of cerebral glioma at 7 T. *Magn Reson Med.* 2014;71(6):2206-2214.
61. Aryal MP, Nagaraja TN, Brown SL, et al. Intratumor distribution and test-retest comparisons of physiological parameters quantified by dynamic contrast-enhanced MRI in rat U251 glioma. *NMR Biomed.* 2014;27(10):1230-1238.
62. Sourbron SP, Buckley DL. Tracer kinetic modelling in MRI: estimating perfusion and capillary permeability. *Phys Med Biol.* 2012;57(2):R1-33.
63. Tofts PS, Berkowitz B, Schnall MD. Quantitative analysis of dynamic Gd-DTPA enhancement in breast tumors using a permeability model. *Magn Reson Med.* 1995;33(4):564-568.
64. Ito H, Ibaraki M, Kanno I, Fukuda H, Miura S. Changes in cerebral blood flow and cerebral oxygen metabolism during neural activation measured by positron emission tomography: comparison with blood oxygenation level-dependent contrast measured by functional magnetic resonance imaging. *J Cereb Blood Flow Metab.* 2005;25(3):371-377.

65. Meier P, Zierler KL. On the theory of the indicator-dilution method for measurement of blood flow and volume. *J Appl Physiol.* 1954;6(12):731-744.
66. Zierler K. Indicator dilution methods for measuring blood flow, volume, and other properties of biological systems: a brief history and memoir. *Ann Biomed Eng.* 2000;28(8):836-848.
67. Crone C. The Permeability of Capillaries in Various Organs as Determined by Use of the 'Indicator Diffusion' Method. *Acta Physiol Scand.* 1963;58:292-305.
68. Knight RA, Nagaraja TN, Ewing JR, et al. Quantitation and localization of blood-to-brain influx by magnetic resonance imaging and quantitative autoradiography in a model of transient focal ischemia. *Magn Reson Med.* 2005;54(4):813-821.
69. Nagaraja TN, Knight RA, Ewing JR, Karki K, Nagesh V, Fenstermacher JD. Multiparametric magnetic resonance imaging and repeated measurements of blood-brain barrier permeability to contrast agents. *Methods Mol Biol.* 2011;686:193-212.
70. Renkin EM. Transport of potassium-42 from blood to tissue in isolated mammalian skeletal muscles. *Am J Physiol.* 1959;197:1205-1210.
71. Ewing JR, Knight RA, Nagaraja TN, et al. Patlak plots of Gd-DTPA MRI data yield blood-brain transfer constants concordant with those of 14C-sucrose in areas of blood-brain opening. *Magn Reson Med.* 2003;50(2):283-292.
72. Cao Y, Brown SL, Knight RA, Fenstermacher JD, Ewing JR. Effect of intravascular-to-extravascular water exchange on the determination of blood-to-tissue transfer constant by magnetic resonance imaging. *Magn Reson Med.* 2005;53(2):282-293.
73. Haroon HA, Buckley DL, Patankar TA, et al. A comparison of Ktrans measurements obtained with conventional and first pass pharmacokinetic models in human gliomas. *J Magn Reson Imaging.* 2004;19(5):527-536.
74. Harrer JU, Parker GJ, Haroon HA, et al. Comparative study of methods for determining vascular permeability and blood volume in human gliomas. *J Magn Reson Imaging.* 2004;20(5):748-757.
75. Symonds MRE, Moussalli A. A brief guide to model selection, multimodel inference and model averaging in behavioural ecology using Akaike's information criterion. *Behavioral Ecology and Sociobiology.* 2011;65(1):13-21.
76. Tietze A, Nielsen A, Klaerke Mikkelsen I, et al. Bayesian modeling of Dynamic Contrast Enhanced MRI data in cerebral glioma patients improves the diagnostic quality of hemodynamic parameter maps. *PLoS One.* 2018;13(9):e0202906.
77. Bagher-Ebadian H, Brown SL, Ghassemi MM, et al. Probabilistic nested model selection in pharmacokinetic analysis of DCE-MRI data in animal model of cerebral tumor. *Sci Rep.* 2025;15(1):1786.
78. Chwang WB, Jain R, Bagher-Ebadian H, et al. Measurement of rat brain tumor kinetics using an intravascular MR contrast agent and DCE-MRI nested model selection. *J Magn Reson Imaging.* 2014;40(5):1223-1229.
79. Shukla-Dave A, Lee N, Stambuk H, et al. Average arterial input function for quantitative dynamic contrast enhanced magnetic resonance imaging of neck nodal metastases. *BMC Med Phys.* 2009;9:4.

80. Calamante F, Morup M, Hansen LK. Defining a local arterial input function for perfusion MRI using independent component analysis. *Magn Reson Med.* 2004;52(4):789-797.
81. Calamante F. Arterial input function in perfusion MRI: a comprehensive review. *Prog Nucl Magn Reson Spectrosc.* 2013;74:1-32.
82. Nagaraja TN, Karki K, Ewing JR, et al. The MRI-measured arterial input function resulting from a bolus injection of Gd-DTPA in a rat model of stroke slightly underestimates that of Gd-[14C]DTPA and marginally overestimates the blood-to-brain influx rate constant determined by Patlak plots. *Magn Reson Med.* 2010;63(6):1502-1509.
83. Bereczki D, Wei L, Otsuka T, et al. Hypercapnia slightly raises blood volume and sizably elevates flow velocity in brain microvessels. *Am J Physiol.* 1993;264(5 Pt 2):H1360-1369.
84. Rey JA, Ewing JR, Sarntinoranont M. A computational model of glioma reveals opposing, stiffness-sensitive effects of leaky vasculature and tumor growth on tissue mechanical stress and porosity. *Biomech Model Mechanobiol.* 2021;20(5):1981-2000.
85. Schneider T, Mawrin C, Scherlach C, Skalej M, Firsching R. Gliomas in adults. *Dtsch Arztebl Int.* 2010;107(45):799-807; quiz 808.
86. Ostrom QT, Bauchet L, Davis FG, et al. The epidemiology of glioma in adults: a "state of the science" review. *Neuro Oncol.* 2014;16(7):896-913.
87. Ostrom QT, Cioffi G, Gittleman H, et al. CBTRUS Statistical Report: Primary Brain and Other Central Nervous System Tumors Diagnosed in the United States in 2012-2016. *Neuro Oncol.* 2019;21(Suppl 5):v1-v100.
88. Ostrom QT, Gittleman H, Xu J, et al. CBTRUS Statistical Report: Primary Brain and Other Central Nervous System Tumors Diagnosed in the United States in 2009-2013. *Neuro Oncol.* 2016;18(suppl_5):v1-v75.
89. Shergalis A, Bankhead A, 3rd, Luesakul U, Muangsin N, Neamati N. Current Challenges and Opportunities in Treating Glioblastoma. *Pharmacol Rev.* 2018;70(3):412-445.
90. Delgado-Lopez PD, Corrales-Garcia EM. Survival in glioblastoma: a review on the impact of treatment modalities. *Clin Transl Oncol.* 2016;18(11):1062-1071.
91. Lutterbach J, Guttenberger R, Pagenstecher A. Gliosarcoma: a clinical study. *Radiother Oncol.* 2001;61(1):57-64.
92. Muldoon LL, Alvarez JI, Begley DJ, et al. Immunologic privilege in the central nervous system and the blood-brain barrier. *J Cereb Blood Flow Metab.* 2013;33(1):13-21.
93. Padhani AR, Miles KA. Multiparametric imaging of tumor response to therapy. *Radiology.* 2010;256(2):348-364.
94. Bell LK, Ainsworth NL, Lee SH, Griffiths JR. MRI & MRS assessment of the role of the tumour microenvironment in response to therapy. *NMR Biomed.* 2011;24(6):612-635.
95. Nagaraja TN, Aryal MP, Brown SL, et al. Cilengitide-induced temporal variations in transvascular transfer parameters of tumor vasculature in a rat glioma model:

identifying potential MRI biomarkers of acute effects. *PLoS One.* 2013;8(12):e84493.
96. Padhani AR, Liu G, Koh DM, et al. Diffusion-weighted magnetic resonance imaging as a cancer biomarker: consensus and recommendations. *Neoplasia.* 2009;11(2):102-125.
97. Nagaraja TN, Elmghirbi R, Brown SL, et al. Reproducibility and relative stability in magnetic resonance imaging indices of tumor vascular physiology over a period of 24h in a rat 9L gliosarcoma model. *Magn Reson Imaging.* 2017;44:131-139.
98. Nagaraja TN, Elmghirbi R, Brown SL, et al. Imaging acute effects of bevacizumab on tumor vascular kinetics in a preclinical orthotopic model of U251 glioma. *NMR Biomed.* 2021;34(7):e4516.
99. Elmghirbi R, Nagaraja TN, Brown SL, et al. Acute Temporal Changes of MRI-Tracked Tumor Vascular Parameters after Combined Anti-angiogenic and Radiation Treatments in a Rat Glioma Model: Identifying Signatures of Synergism. *Radiat Res.* 2017;187(1):79-88.
100. Padhani AR, Khan AA. Diffusion-weighted (DW) and dynamic contrast-enhanced (DCE) magnetic resonance imaging (MRI) for monitoring anticancer therapy. *Target Oncol.* 2010;5(1):39-52.
101. Amer A, Ansari S, Krayyem A, et al. Dynamic Contrast-enhanced MRI Processing Comparison for Distinguishing True Progression From Pseudoprogression in High-grade Glioma. *J Comput Assist Tomogr.* 2025;49(4):656-661.
102. Arevalo-Perez J, Trang A, Yllera-Contreras E, et al. Longitudinal Evaluation of DCE-MRI as an Early Indicator of Progression after Standard Therapy in Glioblastoma. *Cancers (Basel).* 2024;16(10).
103. Thompson G, Mills SJ, Coope DJ, O'Connor JP, Jackson A. Imaging biomarkers of angiogenesis and the microvascular environment in cerebral tumours. *Br J Radiol.* 2011;84 Spec No 2(Spec Iss 2):S127-144.
104. Woodall RT, Sahoo P, Cui Y, et al. Repeatability of tumor perfusion kinetics from dynamic contrast-enhanced MRI in glioblastoma. *Neurooncol Adv.* 2021;3(1):vdab174.
105. Knopp MV, Giesel FL, Marcos H, von Tengg-Kobligk H, Choyke P. Dynamic contrast-enhanced magnetic resonance imaging in oncology. *Top Magn Reson Imaging.* 2001;12(4):301-308.
106. Jackson A, Jayson GC, Li KL, et al. Reproducibility of quantitative dynamic contrast-enhanced MRI in newly presenting glioma. *Br J Radiol.* 2003;76(903):153-162.
107. Kim B, Chenevert TL, Ross BD. Growth kinetics and treatment response of the intracerebral rat 9L brain tumor model: a quantitative in vivo study using magnetic resonance imaging. *Clin Cancer Res.* 1995;1(6):643-650.
108. Kim JH, Im GH, Yoon J, et al. Dynamic contrast-enhanced MRI for assessing therapeutic response of choroidal neovascularization in a rat model. *Invest Ophthalmol Vis Sci.* 2012;53(12):7693-7700.

109. Chawla S, Kim S, Loevner LA, et al. Prediction of disease-free survival in patients with squamous cell carcinomas of the head and neck using dynamic contrast-enhanced MR imaging. *AJNR Am J Neuroradiol.* 2011;32(4):778-784.
110. Cha S, Yang L, Johnson G, et al. Comparison of microvascular permeability measurements, K(trans), determined with conventional steady-state T1-weighted and first-pass T2*-weighted MR imaging methods in gliomas and meningiomas. *AJNR Am J Neuroradiol.* 2006;27(2):409-417.
111. Zhang N, Zhang L, Qiu B, Meng L, Wang X, Hou BL. Correlation of volume transfer coefficient Ktrans with histopathologic grades of gliomas. *J Magn Reson Imaging.* 2012;36(2):355-363.
112. Mills SJ, Patankar TA, Haroon HA, Baleriaux D, Swindell R, Jackson A. Do cerebral blood volume and contrast transfer coefficient predict prognosis in human glioma? *AJNR Am J Neuroradiol.* 2006;27(4):853-858.
113. Bluemke DA, Gatsonis CA, Chen MH, et al. Magnetic resonance imaging of the breast prior to biopsy. *JAMA.* 2004;292(22):2735-2742.
114. Chao SL, Metens T, Lemort M. TumourMetrics: a comprehensive clinical solution for the standardization of DCE-MRI analysis in research and routine use. *Quant Imaging Med Surg.* 2017;7(5):496-510.
115. Ohmura K, Tomita H, Hara A. Peritumoral Edema in Gliomas: A Review of Mechanisms and Management. *Biomedicines.* 2023;11(10).
116. Blystad I, Warntjes JBM, Smedby O, Lundberg P, Larsson EM, Tisell A. Quantitative MRI using relaxometry in malignant gliomas detects contrast enhancement in peritumoral oedema. *Sci Rep.* 2020;10(1):17986.
117. Blystad I, Warntjes JBM, Smedby O, Lundberg P, Larsson EM, Tisell A. Quantitative MRI for analysis of peritumoral edema in malignant gliomas. *PLoS One.* 2017;12(5):e0177135.
118. Paszek MJ, Zahir N, Johnson KR, et al. Tensional homeostasis and the malignant phenotype. *Cancer Cell.* 2005;8(3):241-254.
119. Tse JM, Cheng G, Tyrrell JA, et al. Mechanical compression drives cancer cells toward invasive phenotype. *Proceedings of the National Academy of Sciences of the United States of America.* 2012;109(3):911-916.
120. Rey JA, Spanick KG, Cabral G, et al. Heterogeneous Mechanical Stress and Interstitial Fluid Flow Predictions Derived from DCE-MRI for Rat U251N Orthotopic Gliomas. *Ann Biomed Eng.* 2024;52(11):3053-3066.
121. Kerschbaumer J, Bauer M, Popovscaia M, Grams AE, Thome C, Freyschlag CF. Correlation of Tumor and Peritumoral Edema Volumes with Survival in Patients with Cerebral Metastases. *Anticancer Res.* 2017;37(2):871-875.
122. Wiig H, Tenstad O, Iversen PO, Kalluri R, Bjerkvig R. Interstitial fluid: the overlooked component of the tumor microenvironment? *Fibrogenesis Tissue Repair.* 2010;3:12.
123. Reed RK, Rubin K. Transcapillary exchange: role and importance of the interstitial fluid pressure and the extracellular matrix. *Cardiovasc Res.* 2010;87(2):211-217.

124. Jain RK, Tong RT, Munn LL. Effect of vascular normalization by antiangiogenic therapy on interstitial hypertension, peritumor edema, and lymphatic metastasis: insights from a mathematical model. *Cancer Res.* 2007;67(6):2729-2735.
125. Rofstad EK, Tunheim SH, Mathiesen B, et al. Pulmonary and lymph node metastasis is associated with primary tumor interstitial fluid pressure in human melanoma xenografts. *Cancer Res.* 2002;62(3):661-664.
126. Lunt SJ, Fyles A, Hill RP, Milosevic M. Interstitial fluid pressure in tumors: therapeutic barrier and biomarker of angiogenesis. *Future Oncol.* 2008;4(6):793-802.
127. Curti BD, Urba WJ, Alvord WG, et al. Interstitial pressure of subcutaneous nodules in melanoma and lymphoma patients: changes during treatment. *Cancer Res.* 1993;53(10 Suppl):2204-2207.
128. Milosevic M, Fyles A, Hedley D, et al. Interstitial fluid pressure predicts survival in patients with cervix cancer independent of clinical prognostic factors and tumor oxygen measurements. *Cancer Res.* 2001;61(17):6400-6405.
129. Taghian AG, Abi-Raad R, Assaad SI, et al. Paclitaxel decreases the interstitial fluid pressure and improves oxygenation in breast cancers in patients treated with neoadjuvant chemotherapy: clinical implications. *J Clin Oncol.* 2005;23(9):1951-1961.
130. Garpebring A, Brynolfsson P, Yu J, et al. Uncertainty estimation in dynamic contrast-enhanced MRI. *Magn Reson Med.* 2013;69(4):992-1002.
131. Hoult DI, Richards RE. The signal-to-noise ratio of the nuclear magnetic resonance experiment. 1976. *J Magn Reson.* 2011;213(2):329-343.
132. Godenschweger F, Kagebein U, Stucht D, et al. Motion correction in MRI of the brain. *Phys Med Biol.* 2016;61(5):R32-56.
133. Bonmassar G, Serano P. MRI-Induced Heating of Coils for Microscopic Magnetic Stimulation at 1.5 Tesla: An Initial Study. *Front Hum Neurosci.* 2020;14:53.
134. Hui SCN, Mikkelsen M, Zollner HJ, et al. Frequency drift in MR spectroscopy at 3T. *Neuroimage.* 2021;241:118430.
135. Smith AM, Lewis BK, Ruttimann UE, et al. Investigation of low frequency drift in fMRI signal. *Neuroimage.* 1999;9(5):526-533.
136. Mo H, Harwood JS, Raftery D. Receiver gain function: the actual NMR receiver gain. *Magn Reson Chem.* 2010;48(3):235-238.
137. Turner R. Gradient coil design: a review of methods. *Magn Reson Imaging.* 1993;11(7):903-920.
138. Gruber B, Froeling M, Leiner T, Klomp DWJ. RF coils: A practical guide for nonphysicists. *J Magn Reson Imaging.* 2018;48(3):590-604.
139. Foerster BU, Tomasi D, Caparelli EC. Magnetic field shift due to mechanical vibration in functional magnetic resonance imaging. *Magn Reson Med.* 2005;54(5):1261-1267.
140. Wymer DT, Patel KP, Burke WF, 3rd, Bhatia VK. Phase-Contrast MRI: Physics, Techniques, and Clinical Applications. *Radiographics.* 2020;40(1):122-140.
141. El-Sharkawy AM, Schar M, Bottomley PA, Atalar E. Monitoring and correcting spatio-temporal variations of the MR scanner's static magnetic field. *MAGMA.* 2006;19(5):223-236.

142. Halefoglu AM, Yousem DM. Susceptibility weighted imaging: Clinical applications and future directions. *World J Radiol.* 2018;10(4):30-45.
143. Kumar A, Bottomley PA. Optimized quadrature surface coil designs. *MAGMA.* 2008;21(1-2):41-52.
144. Kathiravan S, Kanakaraj J. A review on potential issues and challenges in MR imaging. *ScientificWorldJournal.* 2013;2013:783715.
145. Gallagher TA, Nemeth AJ, Hacein-Bey L. An introduction to the Fourier transform: relationship to MRI. *AJR Am J Roentgenol.* 2008;190(5):1396-1405.
146. Luypaert R, Sourbron S, Makkat S, de Mey J. Error estimation for perfusion parameters obtained using the two-compartment exchange model in dynamic contrast-enhanced MRI: a simulation study. *Phys Med Biol.* 2010;55(21):6431-6443.
147. Dale BM, Jesberger JA, Lewin JS, Hillenbrand CM, Duerk JL. Determining and optimizing the precision of quantitative measurements of perfusion from dynamic contrast enhanced MRI. *J Magn Reson Imaging.* 2003;18(5):575-584.
148. Di Giovanni P, Azlan CA, Ahearn TS, Semple SI, Gilbert FJ, Redpath TW. The accuracy of pharmacokinetic parameter measurement in DCE-MRI of the breast at 3 T. *Phys Med Biol.* 2010;55(1):121-132.
149. Wake N, Chandarana H, Rusinek H, et al. Accuracy and precision of quantitative DCE-MRI parameters: How should one estimate contrast concentration? *Magn Reson Imaging.* 2018;52:16-23.
150. Sijbers J, den Dekker AJ, Van Audekerke J, Verhoye M, Van Dyck D. Estimation of the noise in magnitude MR images. *Magn Reson Imaging.* 1998;16(1):87-90.
151. Gudbjartsson H, Patz S. The Rician distribution of noisy MRI data. *Magn Reson Med.* 1995;34(6):910-914.
152. Andersen AH. On the Rician distribution of noisy MRI data. *Magn Reson Med.* 1996;36(2):331-333.
153. Osuka S, Van Meir EG. Overcoming therapeutic resistance in glioblastoma: the way forward. *J Clin Invest.* 2017;127(2):415-426.
154. Hasselbach LA, Irtenkauf SM, Lemke NW, et al. Optimization of high grade glioma cell culture from surgical specimens for use in clinically relevant animal models and 3D immunochemistry. *J Vis Exp.* 2014(83):e51088.
155. Jost SC, Wanebo JE, Song SK, et al. In vivo imaging in a murine model of glioblastoma. *Neurosurgery.* 2007;60(2):360-370; discussion 370-361.
156. Jalali S, Chung C, Foltz W, et al. MRI biomarkers identify the differential response of glioblastoma multiforme to anti-angiogenic therapy. *Neuro Oncol.* 2014;16(6):868-879.
157. Chenevert TL, McKeever PE, Ross BD. Monitoring early response of experimental brain tumors to therapy using diffusion magnetic resonance imaging. *Clin Cancer Res.* 1997;3(9):1457-1466.
158. Leach MO, Brindle KM, Evelhoch JL, et al. The assessment of antiangiogenic and antivascular therapies in early-stage clinical trials using magnetic resonance imaging: issues and recommendations. *Br J Cancer.* 2005;92(9):1599-1610.
159. Bhandari A, Bansal A, Singh A, Sinha N. Perfusion kinetics in human brain tumor with DCE-MRI derived model and CFD analysis. *J Biomech.* 2017;59:80-89.

160. Magdoom KN, Pishko GL, Rice L, Pampo C, Siemann DW, Sarntinoranont M. MRI-based computational model of heterogeneous tracer transport following local infusion into a mouse hind limb tumor. *PLoS One.* 2014;9(3):e89594.
161. Pishko GL, Astary GW, Zhang J, Mareci TH, Sarntinoranont M. Role of convection and diffusion on DCE-MRI parameters in low leakiness KHT sarcomas. *Microvasc Res.* 2012;84(3):306-313.
162. Bhandari A, Jaiswal K, Singh A, Zhan W. Convection-Enhanced Delivery of Antiangiogenic Drugs and Liposomal Cytotoxic Drugs to Heterogeneous Brain Tumor for Combination Therapy. *Cancers (Basel).* 2022;14(17).
163. Ross BD, Moffat BA, Lawrence TS, et al. Evaluation of cancer therapy using diffusion magnetic resonance imaging. *Mol Cancer Ther.* 2003;2(6):581-587.
164. Kamali A, Gandhi A, Nunez LC, et al. The Role of Apparent Diffusion Coefficient Values in Glioblastoma: Differentiating Tumor Progression Versus Treatment-Related Changes. *J Comput Assist Tomogr.* 2022;46(6):923-928.
165. Barajas RF, Jr., Rubenstein JL, Chang JS, Hwang J, Cha S. Diffusion-weighted MR imaging derived apparent diffusion coefficient is predictive of clinical outcome in primary central nervous system lymphoma. *AJNR Am J Neuroradiol.* 2010;31(1):60-66.
166. deCarvalho AC, Kim H, Poisson LM, et al. Discordant inheritance of chromosomal and extrachromosomal DNA elements contributes to dynamic disease evolution in glioblastoma. *Nat Genet.* 2018;50(5):708-717.
167. Houchens DP, Ovejera AA, Riblet SM, Slagel DE. Human brain tumor xenografts in nude mice as a chemotherapy model. *Eur J Cancer Clin Oncol.* 1983;19(6):799-805.
168. Jacobs VL, Valdes PA, Hickey WF, De Leo JA. Current review of in vivo GBM rodent models: emphasis on the CNS-1 tumour model. *ASN Neuro.* 2011;3(3):e00063.
169. Haddad AF, Young JS, Amara D, et al. Mouse models of glioblastoma for the evaluation of novel therapeutic strategies. *Neurooncol Adv.* 2021;3(1):vdab100.
170. Radaelli E, Ceruti R, Patton V, et al. Immunohistopathological and neuroimaging characterization of murine orthotopic xenograft models of glioblastoma multiforme recapitulating the most salient features of human disease. *Histol Histopathol.* 2009;24:879–891.
171. Qiang L, Yang Y, Ma YJ, et al. Isolation and characterization of cancer stem like cells in human glioblastoma cell lines. *Cancer Lett.* 2009;279(1):13-21.
172. Camphausen K, Purow B, Sproull M, et al. Influence of in vivo growth on human glioma cell line gene expression: convergent profiles under orthotopic conditions. *Proceedings of the National Academy of Sciences of the United States of America.* 2005;102(23):8287-8292.
173. Torsvik A, Stieber D, Enger PO, et al. U-251 revisited: genetic drift and phenotypic consequences of long-term cultures of glioblastoma cells. *Cancer Med.* 2014;3(4):812-824.
174. Benda P, Someda K, Messer J, Sweet WH. Morphological and immunochemical studies of rat glial tumors and clonal strains propagated in culture. *J Neurosurg.* 1971;34(3):310-323.

175. Schmidek HH, Nielsen SL, Schiller AL, Messer J. Morphological studies of rat brain tumors induced by N-nitrosomethylurea. *J Neurosurg.* 1971;34(3):335-340.
176. Henderson SD, Kimler BF, Morantz RA. Radiation therapy of 9L rat brain tumors. *Int J Radiat Oncol Biol Phys.* 1981;7(4):497-502.
177. Wen P, Loeffler JS, Morris JH, Lampson LA. The effects of irradiation on major histocompatibility complex expression and lymphocytic infiltration in the normal rat brain and the 9L gliosarcoma brain tumor model. *J Neuroimmunol.* 1990;27(2-3):239-244.
178. Kimler BF, Liu C, Evans RG, Morantz RA. Intracerebral chemotherapy in the 9L rat brain tumor model. *J Neurooncol.* 1992;14(3):191-200.
179. Kruse CA, Mitchell DH, Kleinschmidt-DeMasters BK, et al. Systemic chemotherapy combined with local adoptive immunotherapy cures rats bearing 9L gliosarcoma. *J Neurooncol.* 1993;15(2):97-112.
180. Tentler JJ, Tan AC, Weekes CD, et al. Patient-derived tumour xenografts as models for oncology drug development. *Nat Rev Clin Oncol.* 2012;9(6):338-350.
181. Xu Z, Kader M, Sen R, Placantonakis DG. Orthotopic Patient-Derived Glioblastoma Xenografts in Mice. *Methods Mol Biol.* 2018;1741:183-190.
182. Kim MP, Evans DB, Wang H, Abbruzzese JL, Fleming JB, Gallick GE. Generation of orthotopic and heterotopic human pancreatic cancer xenografts in immunodeficient mice. *Nat Protoc.* 2009;4(11):1670-1680.
183. da Hora CC, Schweiger MW, Wurdinger T, Tannous BA. Patient-Derived Glioma Models: From Patients to Dish to Animals. *Cells.* 2019;8(10).
184. deCarvalho AC, Nelson K, Lemke N, et al. Gliosarcoma stem cells undergo glial and mesenchymal differentiation in vivo. *Stem Cells.* 2010;28(2):181-190.
185. Golebiewska A, Hau AC, Oudin A, et al. Patient-derived organoids and orthotopic xenografts of primary and recurrent gliomas represent relevant patient avatars for precision oncology. *Acta Neuropathol.* 2020;140(6):919-949.
186. Benton G, Arnaoutova I, George J, Kleinman HK, Koblinski J. Matrigel: from discovery and ECM mimicry to assays and models for cancer research. *Adv Drug Deliv Rev.* 2014;79-80:3-18.
187. Kleinman HK, Martin GR. Matrigel: basement membrane matrix with biological activity. *Semin Cancer Biol.* 2005;15(5):378-386.
188. Ewing JR, Wei L, Knight RA, et al. Direct comparison of local cerebral blood flow rates measured by MRI arterial spin-tagging and quantitative autoradiography in a rat model of experimental cerebral ischemia. *J Cereb Blood Flow Metab.* 2003;23(2):198-209.
189. Paudyal R, Bagher-Ebadian H, Nagaraja TN, Fenstermacher JD, Ewing JR. Modeling of Look-Locker estimates of the magnetic resonance imaging estimate of longitudinal relaxation rate in tissue after contrast administration. *Magn Reson Med.* 2011;66(5):1432-1444.
190. Noch E, Khalili K. Molecular mechanisms of necrosis in glioblastoma: the role of glutamate excitotoxicity. *Cancer Biol Ther.* 2009;8(19):1791-1797.
191. Aldape KD, David James C. Pathology and molecular classification. In: Bernstein M, Berger MS, eds. *Neuro-oncology The Essentials.* 2nd ed. New York, NY: Thieme Medical Publishers; 2008:18-31.

192. Serventi J, Behr J. Surgery and Evidence-based Treatments in Patients with Newly Diagnosed High-grade Glioma. *Seminars in oncology nursing.* 2018;34(5):443-453.
193. Suchorska B, Weller M, Tabatabai G, et al. Complete resection of contrast-enhancing tumor volume is associated with improved survival in recurrent glioblastoma-results from the DIRECTOR trial. *Neuro Oncol.* 2016;18(4):549-556.
194. Valadie OG, Brown SL, Farmer K, et al. Characterization of the Response of 9L and U-251N Orthotopic Brain Tumors to 3D Conformal Radiation Therapy. *Radiat Res.* 2023;199(3):217-228.
195. Benner T, van der Kouwe AJ, Kirsch JE, Sorensen AG. Real-time RF pulse adjustment for B0 drift correction. *Magn Reson Med.* 2006;56(1):204-209.
196. Odeen H, Parker DL. Magnetic resonance thermometry and its biological applications - Physical principles and practical considerations. *Prog Nucl Magn Reson Spectrosc.* 2019;110:34-61.
197. Mispelter J LM, Briguet A. *NMR Probeheads for Biophysical and Biomedical Experiments: Theoretical Principles and Practical Guidelines.* Imperial College Press; 2015.
198. Antoniou A, Georgiou L, Christodoulou T, et al. MR relaxation times of agar-based tissue-mimicking phantoms. *J Appl Clin Med Phys.* 2022;23(5):e13533.
199. McIlvain G, Ganji E, Cooper C, Killian ML, Ogunnaike BA, Johnson CL. Reliable preparation of agarose phantoms for use in quantitative magnetic resonance elastography. *J Mech Behav Biomed Mater.* 2019;97:65-73.
200. McAleer MF, Brown PD. Therapeutic management of gliosarcoma in the temozolomide era. *CNS Oncol.* 2015;4(3):171-178.
201. Lopez GY, Van Ziffle J, Onodera C, et al. The genetic landscape of gliomas arising after therapeutic radiation. *Acta Neuropathol.* 2019;137(1):139-150.
202. Perry JR, Ang LC, Bilbao JM, Muller PJ. Clinicopathologic features of primary and postirradiation cerebral gliosarcoma. *Cancer.* 1995;75(12):2910-2918.
203. Salavati H, Debbaut C, Pullens P, Ceelen W. Interstitial fluid pressure as an emerging biomarker in solid tumors. *Biochim Biophys Acta Rev Cancer.* 2022;1877(5):188792.
204. Sarntinoranont M, Rooney F, Ferrari M. Interstitial stress and fluid pressure within a growing tumor. *Ann Biomed Eng.* 2003;31(3):327-335.
205. Jain RK, Martin JD, Stylianopoulos T. The role of mechanical forces in tumor growth and therapy. *Annu Rev Biomed Eng.* 2014;16:321-346.
206. Liu LJ, Brown SL, Ewing JR, Schlesinger M. Phenomenological model of interstitial fluid pressure in a solid tumor. *Phys Rev E Stat Nonlin Soft Matter Phys.* 2011;84(2 Pt 1):021919.
207. Stylianopoulos T, Martin JD, Snuderl M, Mpekris F, Jain SR, Jain RK. Coevolution of solid stress and interstitial fluid pressure in tumors during progression: implications for vascular collapse. *Cancer Res.* 2013;73(13):3833-3841.

208. Kim JH, Khil MS, Kolozsvary A, Gutierrez JA, Brown SL. Fractionated radiosurgery for 9L gliosarcoma in the rat brain. *Int J Radiat Oncol Biol Phys.* 1999;45(4):1035-1040.
209. Kim HG, Yu AR, Lee JJ, Lee YJ, Lim SM, Kim JS. Measurement of Tumor Pressure and Strategies of Imaging Tumor Pressure for Radioimmunotherapy. *Nucl Med Mol Imaging.* 2019;53(4):235-241.
210. Jain RK. Transport of molecules across tumor vasculature. *Cancer Metastasis Rev.* 1987;6(4):559-593.
211. Jang SH, Wientjes MG, Lu D, Au JL. Drug delivery and transport to solid tumors. *Pharm Res.* 2003;20(9):1337-1350.
212. Goel S, Wong AH, Jain RK. Vascular normalization as a therapeutic strategy for malignant and nonmalignant disease. *Cold Spring Harb Perspect Med.* 2012;2(3):a006486.
213. Horsman MR, Nielsen T, Ostergaard L, Overgaard J. Radiation administered as a large single dose or in a fractionated schedule: Role of the tumour vasculature as a target for influencing response. *Acta Oncol.* 2006;45(7):876-880.